Optimization of a Hydraulic Savonius Turbine

Dissertation
for the award of the degree

Doktoringenieur
(Dr.-Ing.)

by M.Sc. Emeel Botrous Shafik Kerikous
Date of birth: 05. July 1986
Place of birth: Cairo, Egypt

Accepted by the Faculty of Process and System Engineering
of the Otto-von-Guericke-University of Magdeburg

Doctoral committee:

Prof. Dr.-Ing. habil. Ulrich Krause	(Chairman)
Prof. Dr.-Ing. habil. Dr. h.c Dominique Thévenin	(Reviewer)
Assoc. Prof. Dr.-Ing. habil. Thierry Maître	(Reviewer)
Prof. Dr. Abdus Samad	(Reviewer)

Submitted on : 26.08.2022
Doctoral Colloquium on : 19.12.2022

To my God

Declaration

I hereby declare that I prepared the submitted work without inadmissible assistance and without the use of any aids other than those indicated. Facts or ideas taken from other sources, either directly or indirectly have been marked as such.

In particular, I did not use the services of a commercial graduation consultation. Furthermore, I have not made payments to third parties either directly or indirectly for any work connected with the content of the submitted dissertation.

This work has so far not been submitted either in Germany or abroad in same or similar form as a dissertation and has also not yet been published as a whole.

Magdeburg,
26.08.2022   Emeel Kerikous

Abstract

Ever-growing energy demand and unacceptable emissions from fossil fuel combustion are major driving forces for expanding alternative, green energy sources. Hydro-power is one promising ecological alternative to meet these energy requirements. Hydro-kinetic turbines produce energy from streaming fluids such as water. This work concentrates only on water flows, because such systems do not require any weir or dam and thus, can be employed with minimal ecological impact with low power output. However, available designs are not yet suitable as efficient water energy converters, in particular for conditions corresponding to low water speeds, as are mostly found in practice. Savonius turbines are particularly robust and cost-efficient but show only poor efficiency. This research aims at maximizing the power output of a hydraulic Savonius turbine using different novel ideas. These ideas were optimized using a numerical model. First, an experimental work was carried out by using PIV (particle image velocimetry) in order to validate the flow structure as well as the power coefficient for a standard Savonius turbine. After the validation of the CFD model, many transient computational fluid dynamics (CFD) simulations were performed using the industrial flow simulation code Star-CCM+, driven by the in-house optimization library OPAL++, and relying on evolutionary algorithms for different cases to obtain the optimal configuration for the hydraulic turbine. The optimization was divided into three steps. First, the blade shape of the concave and convex sides evolved independently from each other (no constant blade thickness), then the shape and position of an obstacle plate in front of the hydraulic Savonius turbine were optimized for the standard Savonius turbine, and finally, three important geometry parameters, the overlap ratio, the gap ratio, and the arc angle were simultaneously optimized. The second step is to check that this improvement could be found in reality, thus experimental work for the thick blade was conducted to check the improvement of the turbine. In parallel to this experimental work, the combination of these parameters was tested and checked for the optimal cases. Finally, an aggressive optimization process was conducted to get the final improvement in the hydraulic Savonius turbine, which produced a substantial increase of 28% in comparison to the standard Savonius turbine.

Zusammenfassung

Der ständig wachsende Energiebedarf und die inakzeptablen Emissionen aus der Verbrennung fossiler Brennstoffe sind die Hauptantriebskräfte für den Ausbau alternativer, grüner Energiequellen. Die Wasserkraft ist eine vielversprechende ökologische Alternative zur Deckung dieses Energiebedarfs. Hydrokinetische Turbinen erzeugen Energie aus strömenden Fluiden wie Wasser. Diese Arbeit konzentriert sich nur auf Wasserströmungen, da solche Systeme keine Wehre oder Dämme benötigen und daher mit minimalen ökologischen Auswirkungen aber bei geringer Leistung eingesetzt werden können. Allerdings sind die vorhandenen Konstruktionen noch nicht als effiziente Wasserenergiewandler geeignet, insbesondere nicht für Bedingungen, die niedrigen Wassergeschwindigkeiten entsprechen, wie sie in der Praxis meist anzutreffen sind. Savonius-Turbinen sind besonders robust und kostengünstig, weisen aber nur einen geringen Wirkungsgrad auf. Diese Forschungsarbeit zielt darauf ab, die Ausgangsleistung einer hydraulischen Savonius-Turbine durch verschiedene neuartige Ideen zu maximieren. Diese Ideen wurden mit Hilfe des numerischen Modells optimiert. Zu diesem Zweck wurden zuerst experimentelle Untersuchungen mit Hilfe von PIV (Particle Image Velocimetry) durchgeführt, um die Strömungsstruktur sowie den Leistungskoeffizienten für die Standard-Savonius-Turbine zu validieren. Nach der Validierung des CFD-Modells wurden zahlreiche instationäre CFD-Simulationen mit dem industriellen Strömungssimulationsprogramm Star-CCM+ durchgeführt, die durch die hauseigene Optimierungsbibliothek OPAL++ unter Verwendung von Evolutionsalgorithmen für verschiedene Fälle gesteuert wurden, um die optimale Konfiguration der Wasserturbine zu ermitteln. Die Optimierung wurde in drei Schritte unterteilt. Zunächst entwickelt sich die Schaufelform der konkaven und der konvexen Seite unabhängig voneinander (keine konstante Schaufeldicke), dann wurden die Form und die Position einer Leitplatte vor der hydraulischen Savonius-Turbine für die Standard-Savonius-Turbine optimiert, am Ende werden, drei wichtige Geometrieparameter, d.h. 1) das Überlappungsverhältnis, 2) das Spaltverhältnis und 3) der Bogenwinkel gleichzeitig optimiert. Der zweite Schritt besteht darin, zu überprüfen, ob diese Verbesserung in der realität nachweisbar sind, weshalb experimentelle Arbeiten für die dicke Schaufel durchgeführt wurden, um die Verbesserung der Turbine zu überprüfen. Parallel zu diesen experimentellen Arbeiten wurde die Kombination dieser Parameter getestet und auf die optimalen Fälle hin überprüft. Schließlich wurde ein aggressiver Optimierungsprozess durchgeführt, um die endgültige Verbesserung der hydraulischen Savonius-Turbine zu erreichen, die eine enorme Verbesserung von 28 % im Vergleich zur Standard-Savonius-Turbine ereicht.

Contents

List of Tables

List of Figures

xiv

xv

xvi

Nomenclatures

Roman Letters

Symbol	Description	Units
A	Projected area of rotor (DH)	[m^2]
C_p	Power coefficient	[$-$]
C_t	Torque coefficient	[$-$]
C_{ts}	Static torque coefficient	[$-$]
D	Turbine diameter ($2R$)	[m]
E	Energy	[J]
H	Blade height	[m]
$\dot{m}$	Mass flow rate	[kg/s]
N	Rotational speed of rotor	[rpm]
P	Output power	[W]
Q	Flow rate	[m^3/s]
R	Turbine radius	[m]
r	Radius of semi-cylindrical blade	[m]
T	Output torque	[Nm]
T_s	Static torque quantifying self-starting capability	[Nm]
U	Water velocity	[m/s]
y	Projected location along Y-axis	[m]

Greek Letters

Symbol	Description	Units
θ	Rotor angle	[°]
λ	Tip speed ratio	[-]
ρ	Density	[kg/m^3]
ψ	Blade arc angle	[°]
ω	Angular speed	[rad/s]

Abbreviations

Acronym	Description
CCD	Charged-coupled device
CFD	Computational fluid dynamics
EA	Evolutionary algorithms
F.S.	Full scale
GA	Genetic algorithm
HAWT	Horizontal axial wind turbine
LSS	Lehrstuhl Strömungsmechanik und Strömungstechnik (Chair of Fluid Mechanics and Technical Flow)
NURBS	Nonuniform rational B-spline
OPAL++	Optimization algorithm library++
PIV	Particle image velocimetry
PTU	Programmable timing unit
RANS	Reynolds-Averaged Navier-Stokes (A mathematical model based on average values of variables for both steady-state and dynamic flows)
RMS	Root-mean-square
SBX	Simulated binary cross-over
TSR	Tip speed ratio

Chapter 1

Introduction

Energy is the ability to do work, hence changes or developments in any aspect of life cannot be achieved without energy. Not only the achievements of civilization and extension of the human capabilities require harnessing various forms of energy but also the simple daily activities like transportation and food preparation, et cetera, demand a source of power. Moreover, as a result of continuous increases in the population, electricity demand is expected to grow by 70% by 2035 [1]. Accordingly, effective use of existing sources of energy and the search for new and renewable sources are major challenges and will become essential for continuous human development and economic growth. It is known that energy cannot be created or destroyed, but it can be converted. Power transferred effectively from oil, gas, coal, biomass, wind or hydropower can be used to produce useful work. Accordingly, this work will be concerned with converting an available energy source to a more useful form.

1.1 Energy resources

Electricity is the most-popular form of energy, which could be produced from primary sources. These primary sources of energy can be divided into two main categories, i.e. non-renewable sources and renewable sources. Non-renewable sources are usually accompanied by polluting by-products and unacceptable emissions both in the form of wasted heat and environmentally unfriendly releases. In this context, effective conversion of renewable, or green energy sources is essential, which is one promising ecological alternative to meet these energy requirements and to create a healthy planet. Figure 1.1 shows the share of renewable energy as a percentage of global electricity production in 2018 [2]. Renewable energy contributes 26.2 % of the total production. This percentage was increased by 8 % in 2021. However, this increase is low compared to the planned three-years target because of the Covid-19 pandemic in 2020, which had

a negative impact on investment in the renewable energy field. Moreover, renewable power additions must triple until 2050 to cover the energetic demand [3].
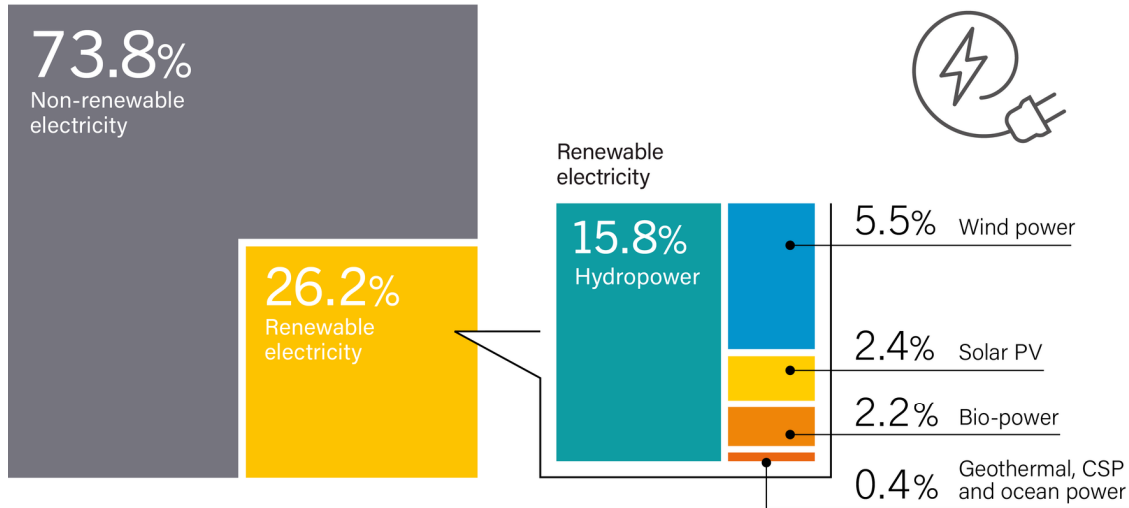
Figure 1.1: Renewable energy share of total global electricity production, 2018 [2].

Renewable energy sources can be classified into five categories, i.e solar, wind, biomass, geothermal, and hydropower. The use of renewable energy is not a modern idea. More than 200 years ago, wood (biomass) was used as the main source of energy as heat. Nowadays, renewable energies have been found to be the best sources of clean and green energy. In 2018, energy from renewable sources contribute 26.2 % on global electricity production, with 5.5 %, 2.4%, 2.2%, 0.4 %, 15.8% from wind, solar, bio-power, geothermal, and hydraulic power, respectively, as shown in Figure 1.1.

In the European Union (EU), renewable energy sources (RES) are not sufficiently utilized to meet the energetic demand. Not only are there different RES in the EU, but their effective use also has a high economic potential. However, renewable energy covers only a small portion (7.8%-8%) of total energy production. Moreover, use of RES could lead to 8.5 million additional jobs in the year 2030. In 2001, the European Commission issued the 2001/77/EC Directive on electricity production from RES, which states that the Community aims to increase the use of renewable energy. In other words, mandatory national goals should be achieved, increasing the individual share of RES in all sectors [4].

1.1.1 Advantages and disadvantages of renewable energy sources

Utilization of renewable energy sources provides a lot of advantages over fossil fuel. However, the use of renewable energy also has some disadvantages. First, the main

advantages of utilizing renewable energy will be stated:

- **Renewable energy will not run out.** Renewable energy usually uses resources directly from the environment such as sunshine, wind, kinetic or potential water energies to provide power. In comparison with fossil fuels, renewable energy has no potential consequences in the case of long-term use. In other words, if fossil fuels are used as a permanent source, they will lead to a number of issues such as a negative environmental impact as well as increasing costs. Moreover, the world will eventually run out of oil and gas [5–7].

- **Human health and environmental benefits.** In principle, renewable energy has a positive effect on air and water. First, one of the main advantages of renewable energies is that these sources do not contribute to the conventional greenhouse effect because they usually do not produce carbon dioxide. By contrast, fossil fuels are major emitters of carbon dioxide. While 42% of the global emission is coming from the direct production of heat and electrical power, the transportation and industry are responsible only for 25%, and 19%, respectively [8]. Renewable energy does not contribute to air pollution. Second, renewable energy has a beneficial effect on water. Most traditional fossil fuel technologies use a huge amount of water for cooling their system, changing the availability of water. Electrical power stations use water as a coolant [9, 10]. Almost 200 billion cubic meters (40% of the total water) are withdrawn for power generation in the United States [11]. Water pollution constitutes an additional hazard to the environment and human health. Therefore, using renewable energy will reduce all the risks stemming from air and water pollution.

- **Lower operation and maintenance costs.** Use of renewable energy will save a lot of money over the long term. After renewable energy systems are built, there are no operating costs. By contrast, fossil fuel systems require additional fuel purchases at regular intervals during operation. Moreover, the maintenance costs of renewable systems are lower than the maintenance costs of traditional fossil fuels systems. This is because renewable technologies like solar panels or wind turbines have fewer moving parts compared to the traditional fossil systems. All of these parameters and comparisons of running costs for various types of renewable energy can be found in [12].

- **Local energy sources.** Renewable power can mostly be produced from local environmental sources. It is not necessary to import large quantity of energy from

foreign countries. Therefore, energy supplies are less dependent on the politics of foreign countries. Oil and gas are irregularly distributed over the world, creating political tensions and possible wars between countries [7]. Nowadays, there are political tensions between Russia, the European Union, and the United States of America (US) because of the war in Ukraine, and oil and gas play an important role in this tension.

Besides the advantages mentioned, it is also necessary to discuss the disadvantage of the use of renewable energies.

- **Higher initial costs.** While the operation and maintenance costs of renewable energies are lower compared to conventional fossil fuel systems, these technologies still have high initial costs. In order to get high economic returns, it is necessary to use these technologies over the long-term [13].

- **Storage and intermittency.** While renewable energy can be found all over the world, most of them are not available continuously. Sunshine is not available at night; the capacity of the wind is not similar in all seasons. Because of this, storage of renewable energy becomes necessary [14].

Overall, renewable energy has advantages and disadvantages. However, the positive sides outweigh the negative sides at any level, i.e., personal, governmental, or corporate. Not only could renewable energy save a lot of money, but it could also help slow climate change. Renewable energy is an important source of power because of continuing increases in the population, but it will also be mandatory as pollution and the climate change issues increase.

Now, the question is which type of renewable energy meets all of these requirements. In fact, all of the available renewable energy types could be used to meet these demands. However, hydropower, which is energy from flowing water, shows advantages over the other types. First, it is more sustainable with less fluctuations year-round compared to solar energy and wind energy. Second, 70 % of the earth's surface is water, making it an abundant power source. Finally, the hydropower industry is usually related to power generation as well as water management. Thus, support of the hydropower industry will lead to delivering drinking water as well as power to many people around the world.

1.2 Hydropower

In general, hydropower is the extraction of energy from moving water and its conversion to usable power, i.e. electrical power, or mechanical power. Since hydropower is the biggest source of renewable energy, it should be at the top of the political agenda at every level of the government. Moreover, the International Journal of Hydropower & Dams states that 50 % of local electricity production comes from hydraulic power in 63 countries around the world and at least 90 % in 23 countries [15].

Two principles can be employed in order to extract energy from water streams. The first approach is based on potential energy, using a head difference and requiring a dam or a natural channel [16, 17]. For the dam procedure, there are several environmental issues to consider. First, while dams are used to store water and produce a water head, the water is released from the dam according to energetic demand. This process leads to large fluctuations in the water streams. Accordingly, this negatively affects aquatic life in multiple ways, from water turbidity and temperature to oxygen content; agriculture will also be affected. Second, certain species of fish can not move through a dam; local fish production will decrease. Finally, the water level fluctuation will harm the downstream riverbank; downstream life will be very negatively affected [18]. Because of all of the aforementioned issues, use of the second technology to extract energy from water becomes desirable.

The second one corresponds to hydrokinetic turbines, which produce power directly from the kinetic energy of water currents [19]. While both procedures are often combined in practical systems, pure hydrokinetic turbines have several advantages. Regarding environmental issues in particular, most of the issues mentioned for conventional turbines are released for pure hydrokinetic turbines.

1.3 Pure hydrokinetic turbines

Hydrokinetic machines are generally simple and cost-efficient, although they typically deliver a power output of a few kW at most. In order to increase the total power output, they can easily be combined in arrays. However, hydrokinetic turbines have disadvantages as well. since they use only kinetic energy, they offer limited power production. Additionally, their efficiency is usually quite low, far below the theoretical peak power coefficient (59.3%), which is known as the "Betz limit". Note that, while kinetic turbines can in principle extract energy from any streaming fluid in a liquid or

gaseous state, only water will be considered in this work.

Only a few studies can be found in the literature concerning the optimization of hydrokinetic water turbines, as discussed in Chapter 3. However, the scientific background for this field can be quite easily derived from the abundant literature concerning wind turbines. In principle, for the same turbine size, water turbines operating in a stream at 2–3 m/s can produce four times the power density of wind turbines with a wind speed of 11–13 m/s. The reason for this difference is that the density of water is more than 800 times higher than that of air. This explains the renewed interest in hydraulic turbines, more particularly in Savonius turbines.

1.4 Savonius turbine

There are two main types of turbine that are used to convert the kinetic energy of fluids to mechanical energy. The first one is lift-device turbines, such as a horizontal axial wind turbine (HAWT), Darrieus turbine, H-rotor turbine, as shown in Figure 1.2. This type has a higher efficiency compared to drag-type turbines like the Savonius turbine [20, 21]. Savonius turbines produce torque through the combined impact of drag and pressure forces acting in complex interactions on the blades. In the original design, each blade shows a semi-circular shape. Savonius turbines are typically employed at low tip speed ratios (comparing tip blade speed to water speed). Thus, its rotation speed is usually low as well and its size is smaller in comparison with lift devices. Therefore, they are particularly suitable for environmental water flows. With the standard design, Savonius turbines have very low power coefficients, but are robust, have a simple design, and can be manufactured at low cost. If higher power coefficients could be obtained, Savonius turbines would become a viable system to extract hydrokinetic energy from water.

1.5 Scope of the thesis

The central objective of the work presented here is to maximize the power output of a hydraulic Savonius turbine by changing the blade shape, adding some guiding plates, and adjusting its main parameters. Consequently, this type of turbine will be more suitable for environmental water flows. Not only it will work more efficiently, but the plates might also protect the blades from suspended solids in the water stream.
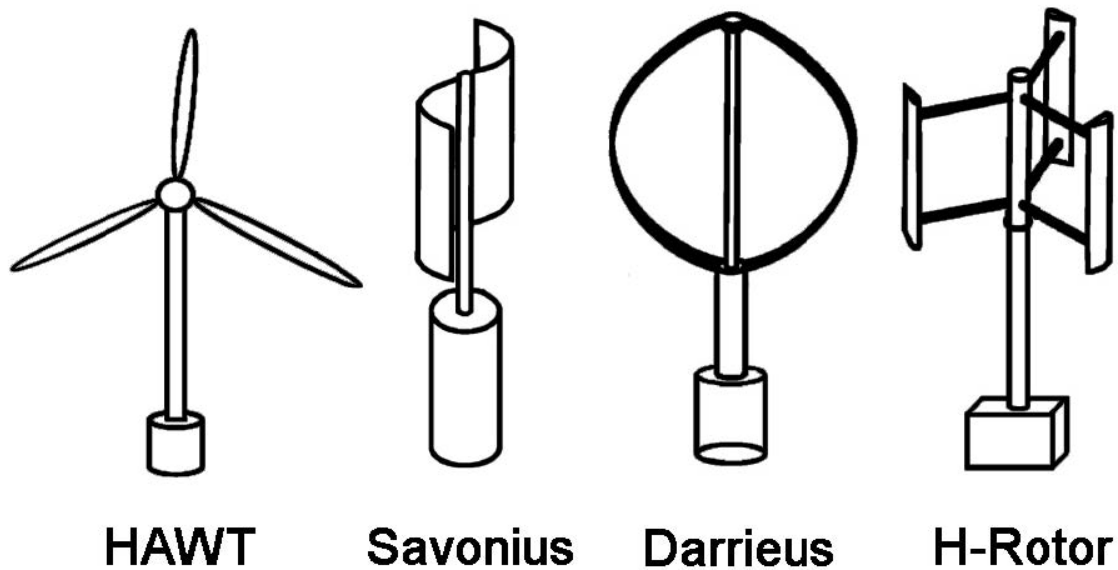
Figure 1.2: Schematics of different types of turbine [20, 21].

1.6 Conclusions and outline

This chapter provides a brief introduction to renewable energy conversion and its importance for human life. In chapter 2, the basics for converting kinetic energy to mechanical energy are discussed in detail, followed by a discussion of the Savonius turbine, which is the main topic of this thesis. In Chapter 3 a literature review of the performance of Savonius turbines is presented. The optimization process will be discussed in chapter 4. The whole methodology of this research is introduced in chapter 5, and will end by including the coupling between the flow solver and the optimizer (OPAL++). All results of the optimization are presented in chapter 6, comparing the new designs with the classical ones. The thesis ends with conclusions and suggestions for future research in chapter 7.

Chapter 2

Basics of Converting Kinetic Energy to Mechanical Energy

2.1 Introduction

As discussed previously, this study is concerned with hydrokinetic turbines. However, the scientific background of these types of turbines is derived from wind turbines. Usually in turbomachinery, laws of similarity could be applied when the working fluid is changed. Both hydraulic and wind turbines have a very small Mach number of less then 0.3. Thus, both working fluids in that case were assumed to be incompressible. If the Reynolds number is kept constant, both turbines have a kinematic similarity [22]. Therefore, the basic concepts of wind turbines will be discussed in the beginning followed by the main concepts for measuring the performance of these turbines. These turbines convert kinetic energy from a fluid, air or water, to mechanical energy to rotate the shaft. Therefore, the main functional component of these turbines is the blade. Between 1922 and 1925, Albert Betz published seminal documents based on the basic laws of physics showing that the mechanical energy produced from streaming air passing through a given-cross section has a physical limit [22]. That means that the converted mechanical energy is proportional to the kinetic energy in the flow by a fixed value. Moreover, he found that the maximum power extraction occurred at a specific ratio between the inlet fluid speed and the linear speed of the impeller.

2.1.1 Betz's momentum theory

When a mass of fluid m moves at a velocity v, its kinetic energy E is calculated by:

$$E = \frac{mv^2}{2} \qquad (2.1)$$

When the fluid passes through a constant cross section A, the flow rate Q can be written as,

$$Q = Av \tag{2.2}$$

and the mass flow rate $\dot{m}$ is related to the flow rate Q and the (constant) density of the fluid ρ by:

$$\dot{m} = \rho Q = \rho Av \tag{2.3}$$

Then the kinetic energy of the fluid could be expressed as power P in W and written as,

$$P = \frac{\rho Av^3}{2} \tag{2.4}$$

The main objective is to convert the kinetic energy to mechanical energy, thus the main question is how much mechanical energy can be extracted from the available flow energy. In other words, the kinetic energy in the flow will decrease, and some will be converted to mechanical power. Therefore, the flow velocity behind the rotor disk will be decreased to v_2, and according to the continuity equation the exit area should be increased to permit the same amount of mass flow. Consequently, the difference between the incoming velocity v_1 and the exit velocity v_2 will produce useful mechanical power, as shown in Figure 2.1. By neglecting any losses, the extracted mechanical energy can be written as,

$$P = \frac{\rho A_1 v_1^3 - \rho A_2 v_2^3}{2} \tag{2.5}$$

From the continuity equation,

$$\dot{m} = \rho A_1 v_1 = \rho A_2 v_2 \tag{2.6}$$

thus,

$$P = \frac{\dot{m}}{2}(v_1^2 - v_2^2) \tag{2.7}$$

From the above equation, it is mathematically clear that, in order to reach the maximum extracted power, the exit velocity v_2 should be zero, but that has no physical meaning. In other words, when the exit velocity is zero, based on the continuity equation the inlet velocity also becomes zero, then there is no flow in the actuator. Therefore, to get the maximum extracted power, mechanical energy should be expressed in term of v_2/v_1. This can be done by applying the law of conservation of
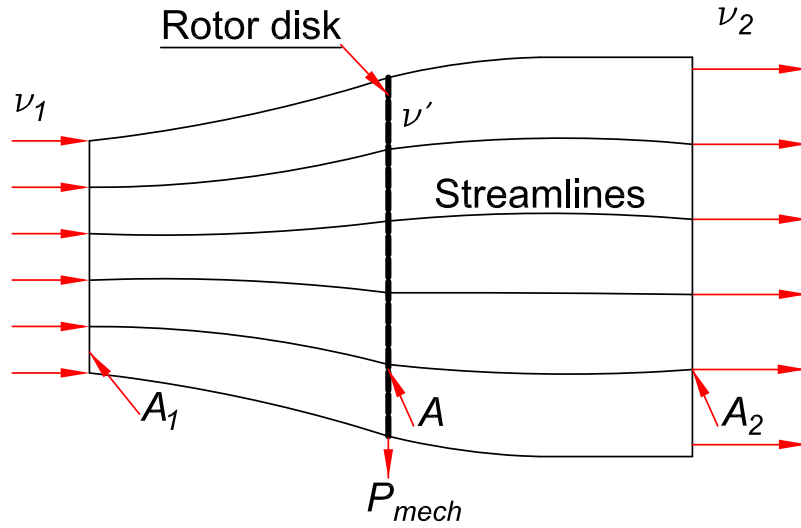
Figure 2.1: Flow field around an actuator disk according to the elementary momentum theory.

momentum.

The fluid acts on the actuator with a force expressed as,

$$F = \dot{m}(v_1 - v_2) \tag{2.8}$$

From Newton's Second Law of "action equals reaction", this force equals the thrust on the actuator which moves with a velocity v'. Therefore, the mechanical power produced is written as,

$$P = Fv' = \dot{m}(v_1 - v_2)v' \tag{2.9}$$

The actuator velocity is proportional to the inlet and exit velocity from the actuator, and this value is obtained simply by equating the mechanical power in Equation 2.9 to the extracted power from the fluid in Equation 2.7:

$$\dot{m}(v_1 - v_2)v' = \frac{\dot{m}}{2}(v_1^2 - v_2^2) \tag{2.10}$$

Therefore, the flow velocity in the actuator plane equals the mean of the sum of the inlet and exit velocities,

$$v' = \frac{v_1 + v_2}{2} \tag{2.11}$$

Then, the mass flow rate through the actuator can be expressed as,

$$\dot{m} = \rho A v' = \rho A \frac{v_1 + v_2}{2} \tag{2.12}$$

By substituting by Equation 2.12 and Equation 2.11 into Equation 2.9, the mechanical power can be expressed as,

$$P = \rho A \frac{v_1 + v_2}{2} \times (v_1 - v_2) \times \frac{v_1 + v_2}{2} \tag{2.13}$$

then,

$$P = \frac{\rho A (v_1^2 - v_2^2)(v_1 + v_2)}{4} \tag{2.14}$$

After the mechanical power was calculated, the reference power available in the fluid should be known; then the performance of the turbine can be expressed. The reference power P_0 can be calculated as the power available just before entering the actuator area and before being converted to mechanical energy. Therefore, the reference power can be calculated with,

$$P_0 = \frac{\rho A v_1^3}{2} \tag{2.15}$$

Now, the performance of the turbine is simply expressed by the usual mechanical power divided by the reference power in the fluid, which is called the power coefficient C_P.

$$C_P = \frac{P}{P_0} = \frac{\dfrac{\rho A (v_1^2 - v_2^2)(v_1 + v_2)}{4}}{\dfrac{\rho A v_1^3}{2}} \tag{2.16}$$

thus,

$$C_P = \frac{P}{P_0} = \frac{1}{2} \left(1 - \left(\frac{v_2}{v_1} \right)^2 \right) \left(1 + \frac{v_2}{v_1} \right) \tag{2.17}$$

It is clear that C_P is a function of only the velocity ratio v_2/v_1. Thus, by mathematical derivative, the maximum power coefficient (ideal power coefficient) can be obtained. The maximum value is obtained at $v_2/v_1 = 1/3$ and the ideal power coefficient in this case, called the Betz limit, is:

$$C_P(\text{max}) = \frac{16}{27} = 0.593 \tag{2.18}$$

2.2 Classification of different turbine designs

As discussed above, the efficiency of the turbines depends on the actuator speed and the fluid speed. The relation between the actuator (blade) tip speed and the inlet velocity speed is called the tip speed ratio:

$$\text{Tip speed ratio} = \lambda = \frac{\omega R}{v} \tag{2.19}$$

where ω is the angular velocity of the turbine, R is the radius of the turbine blade, and v is the free stream velocity of the inlet fluid.
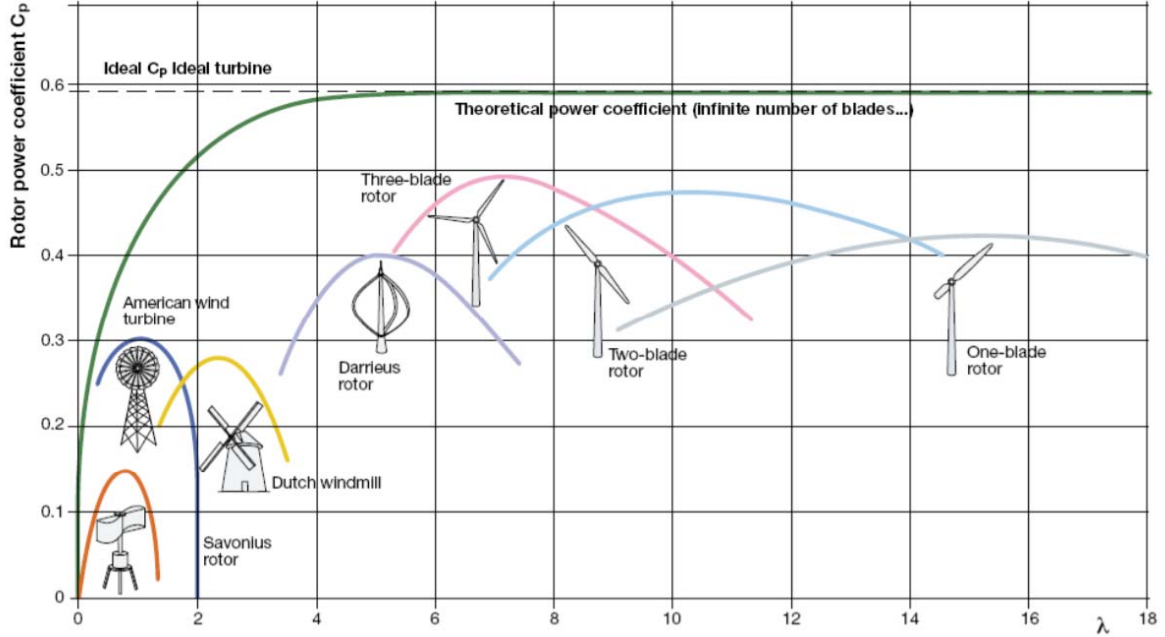
Figure 2.2: Different turbine designs for different tip speed ratios [23].

Figure 2.2 presents different turbine designs for different tip speed ratios. It is clear that the maximum theoretical performance for all types of turbines is achieved at the Betz limit (0.593). From the momentum theory, the main findings can be summarized as:

- The mechanical extracted power is linearly proportional to the area swept by the turbine.

- The mechanical power is proportional to the third degree of the inlet flow velocity.

- The ideal maximum performance of the turbine is the ideal Betz limit which equals 0.593.

2.3 Operating principles of standard Savonius turbines

Usually, the choice of the type of turbine is dependent on the local fluid conditions in the required area, as shown in Figure 2.2. Horizontal turbines (two- and three-bladed)

have better performance compared with all other types of turbines, which leads to them being used in a wide range to convert wind energy to useful mechanical energy. On the other hand, Savonius turbines appear to have a very small power coefficient ($C_P \approx 0.1 - 0.15$). In principle, the Savonius turbine is a slow operating machine usually run at $\lambda \approx 1.5$ or below. Thus, if it is operated in hydraulic applications (water usually has a low fluid speed compared to air), it will rotate with a reasonable rotational speed compared to any other type of turbine. Therefore, Savonius turbines are the best system for aquatic environments. Figure 2.3 shows the main features of a Savonius turbine
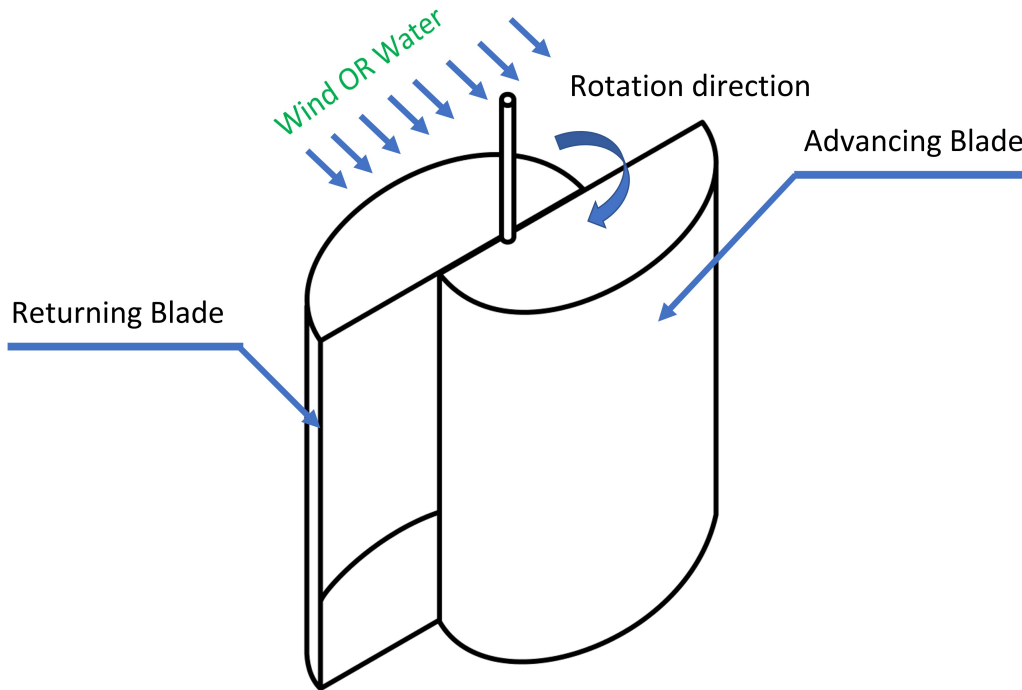
Figure 2.3: Standard Savonius turbine shape.

2.3.1   Performance measurements of Savonius turbine

The performance of such turbines is usually measured by a TSR-C_p curve or by a TSR-C_t curve. The tip speed ratio (TSR or λ) is the ratio between the peak velocity along the blade, which is the tangential velocity at the tip of the rotor, to the velocity of the working fluid (here, water):

$$TSR = \lambda = \frac{v_{tip}}{U} = \frac{\omega R}{U} \tag{2.20}$$

where R is the radius of the turbine, ω is the angular velocity of the rotor and U is the incoming velocity of the working fluid.

The power coefficient C_p is the ratio between the power produced by the turbine to the power available in the working fluid. The torque coefficient C_t is a complementary performance indicator. Both quantities C_p and C_t can be obtained as follows:

$$C_p = \frac{P_{mech}}{P_{available}} = \frac{T\omega}{0.5\rho A U^3} \tag{2.21}$$

$$C_T = \frac{T}{0.5\rho A R U^2} = \left(\frac{T\omega}{0.5\rho A U^3}\right) / \left(\frac{\omega R}{U}\right) = \frac{C_p}{\lambda} \tag{2.22}$$

where A is the projected frontal area of the rotor ($A = D \times H$), with $D = 2R$ the diameter of the turbine, H its height, ρ the density of the working fluid, and T the average torque acting on the rotor. The instantaneous value of the torque depends on the orientation of the turbine. If the torque coefficient is calculated for a fixed turbine in order to check its self-starting capacity, then the value obtained is called the static torque coefficient C_{ts}. In the rest of this thesis, the objective of the optimization process is to maximize the output power coefficient C_p.

2.3.2   Summary

After presenting the maximum theoretical performance of such turbines, and showing the position of the Savonius turbine relative to other types of turbines, the previous studies on such turbines will be illustrated in detail in the next chapter.

Chapter 3

Literature Review

The topic of low-head hydraulic turbines is one of the most active areas in power production research today. While there is until now little in the literature on the specific topic of hydraulic turbines, the fundamental background could be easily derived from the literature concerning wind turbines. Therefore, in this chapter, the research most related to hydraulic turbines and relevant studies concerning wind turbines will be presented. To present all of this literature, this chapter will be divided into various sections. In the beginning, various hydrokinetic turbines will be discussed and a special turbine will be selected. Then, literature concerning the investigation of the flow structures around this selected turbine will be discussed. Finally, all possible solutions to improve its performance will be detailed.

3.1 Investigations of hydrokinetic turbines

As indicated by their names, hydrokinetic turbines convert kinetic energy into usable energy. Generally, these types of turbines are classified into two types according to the position of the axes: axial [24, 25] or cross flow (or vertical) [26, 27]. Another classification is based on their operating principle: lift turbines such as Darrieus turbines [28–32] and modern wind turbines [33], which have a high power coefficient but are very expensive to operate as well as to manufacture [34], or drag-type turbines such as Savonius turbines and water wheels [19, 35]. Drag turbines are robust and easier to construct, which is the main advantage of such type of turbines. However, they usually suffer from low turbine performance. Savonius turbines have more advantages compared to water wheels; they are totally immersed in water, thus they produce more power and less noise. Since water wheels move between two fluids, water and air, they lose energy and produce more noise at the inlet and the outlet positions of the blades from the water.
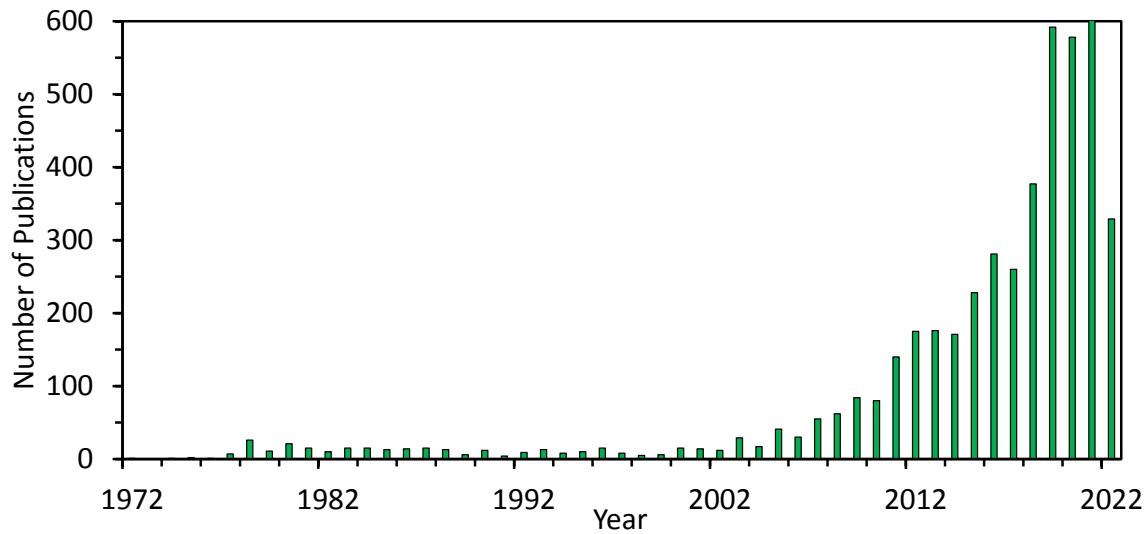
Figure 3.1: Publication per year using keyword "Savonius turbine".

One of the drawbacks of Savonius turbines is their low performance compared to all other turbines. Therefore, many researchers have tried to understand the behavior of such a turbine and how each parameter affects the efficiency in each case. Figure 3.1 shows the number of publications in the field of Savonius turbines every year (for both water and wind turbines) as found by the use of "Savonius turbine" as a keyword using "app.dimensions.ai" website. It is clear now that the field is very active. All of the world is searching for renewable energy that is based on robust and low-cost turbine manufacturing. In the next sections, the most interesting literature related to this research will be presented.

3.2 Savonius turbine

Sigurd Johannes Savonius develop the vertical axis Savonius turbine in the late 1920s. The Savonius turbine is formed by splitting a cylindrical shape into two halves and then arranging these two parts so that an S-shape is formed, and a small gap is created between them [36]. Figure 3.2 shows the main features of a Savonius turbine. In principle, they have many advantages in practice due to their simplicity, robustness, and low cost. However, these turbines have a poor power coefficient. If a greater efficiency could be achieved while maintaining the simplicity of the turbine, Savonius turbines would turn into a very attractive converter for water energy. Before presenting the available improvements for such turbines, the flow pattern around the turbine blade will be discussed.
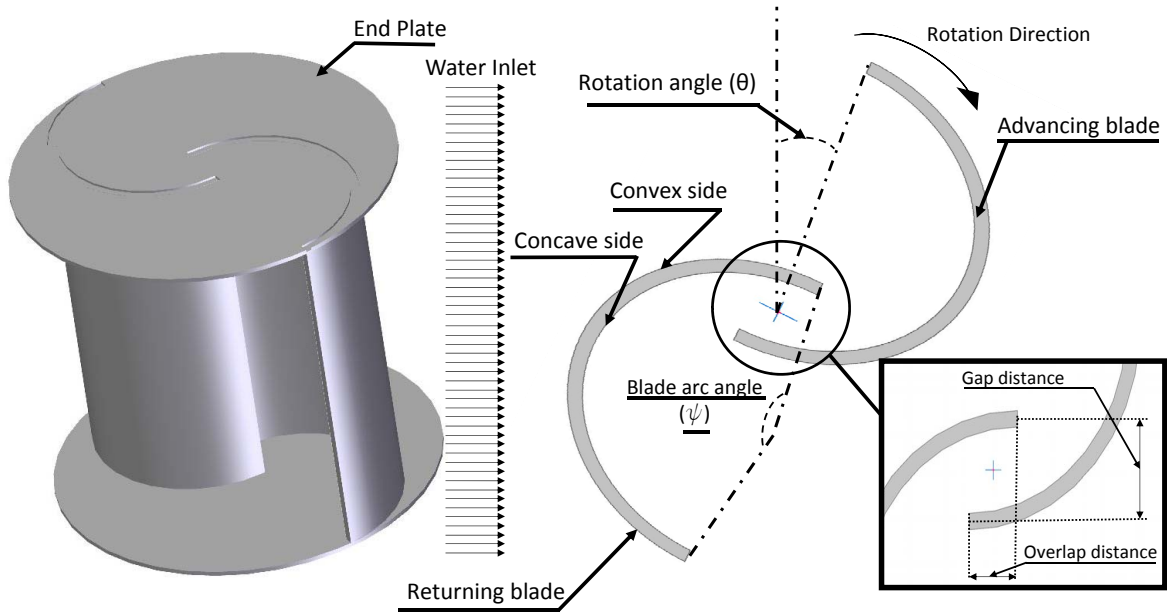
Figure 3.2: Standard Savonius turbine with the main parameters.

3.2.1 Flow pattern around Savonius rotors

The Savonius turbine is a drag-type turbine, but lift forces still make a small contribution although they are not the main source of power. In [37], the flow pattern around a Savonius turbine is shown. The authors have divided the main flow into six different patterns, as shown in Figure 3.3. Flow (I) produces the lift force. For power production, flow (II) and (III) rebuild the pressure on the concave side of the returning blades. However, flow (IV) is the absorbing power flow. For vortex creation around the turbine, while flow (V) produces a vortex on the advancing blade, the vortex in the returning blade is produced by flow (VI). It should be taken into consideration that, the flow distribution changes with the azimuth angle (or rotational angle), therefore the power produced varies with the angle as well.

3.2.2 Performance improvement techniques

From the discussion above and previous studies, the performance of Savonius turbines can be improved by: (1) reducing the fluid resistance acting on the returning blade (Flow (IV) in Figure 3.3), (2) increasing the force acting on the advancing blade (Flow (II) and (III) in the same Figure). Different techniques have been used to improve the system by changing different parameters, such as blade shape, overlap ratio, gap ratio, number of blades, end plate, guide plates, and other accessories [38–43]. In the next sections, these techniques will be discussed in detail.

If the lift forces are increased (Flow (I) in Figure 3.3), performance will be improved. However, this point is not clearly discussed in the existing research. Therefore, this is still one goal of this thesis, but first, other previous studies will be presented.
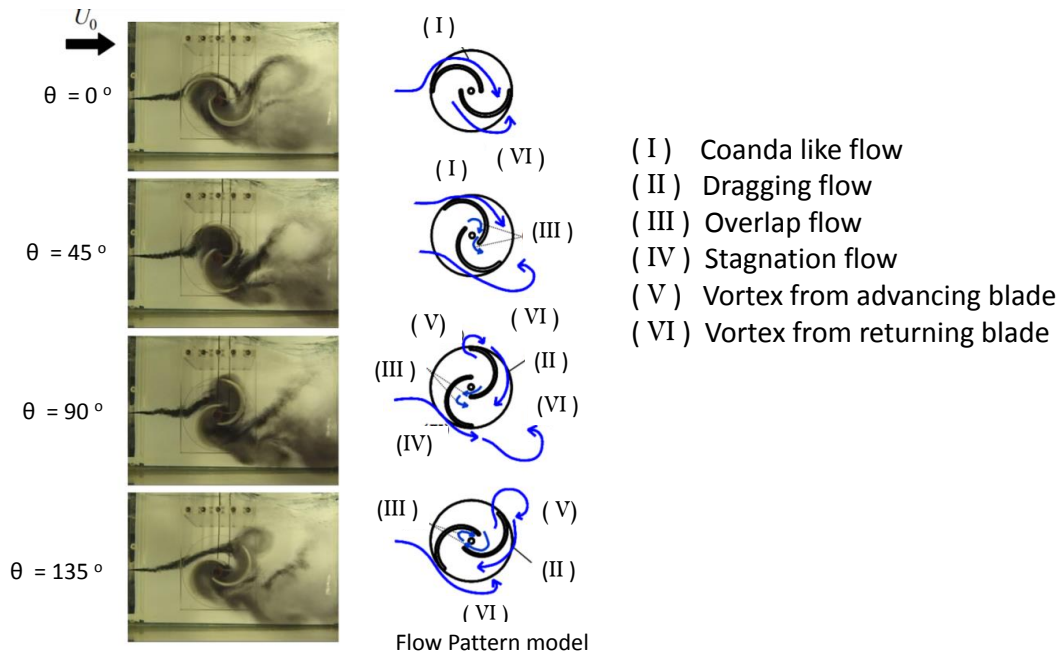
Figure 3.3: Flow pattern around the blades [37].

3.2.2.1 Effect of the number of blades

Numerous studies have attempted to compare the performance of two- and three-bladed Savonius turbines. It has been found that the performance of two blades is better compared to three blades. Several studies confirmed this [44, 45]. The reason is that by increasing the number of blades in the rotor, the angular positions at which the advancing blade produces power without negative interaction with a returning blade are limited. Therefore, the average power over the cycle decreases as shown in Figure 3.4. Moreover, the performance of turbines with different blades numbering between two and eight was investigated in [46], as shown in Figure 3.5. These findings prove that the turbine with only two blades has higher performance compared with all higher numbers of blades. Therefore, only two-bladed Savonius turbines will be considered in this research.
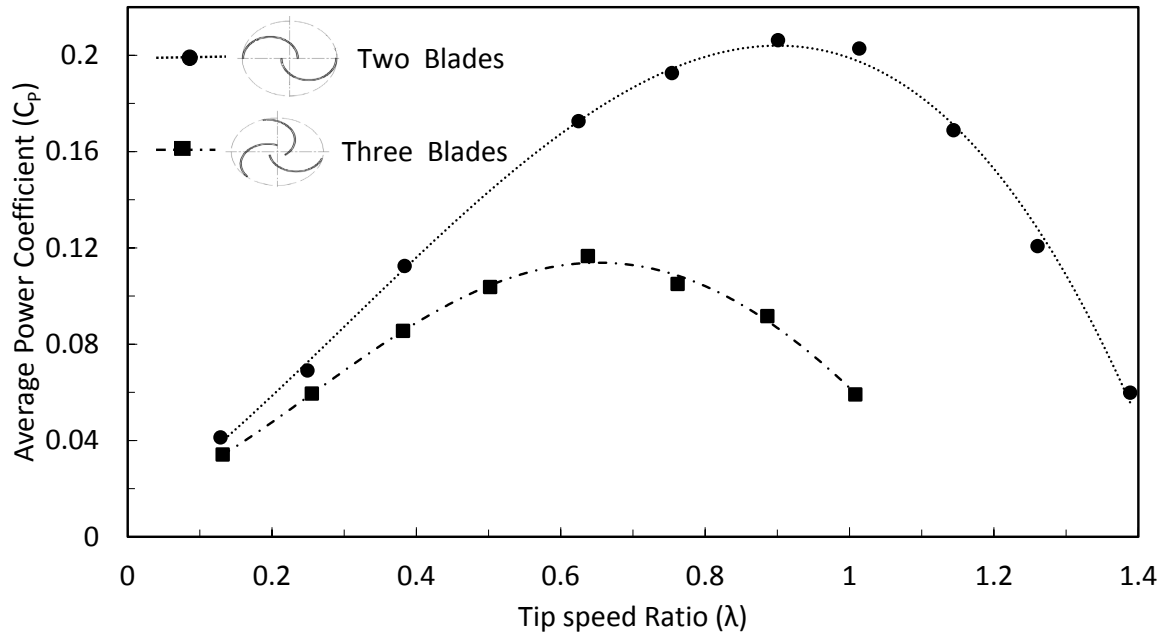
Figure 3.4: Comparision between turbines with two and three blades in the rotor [47].
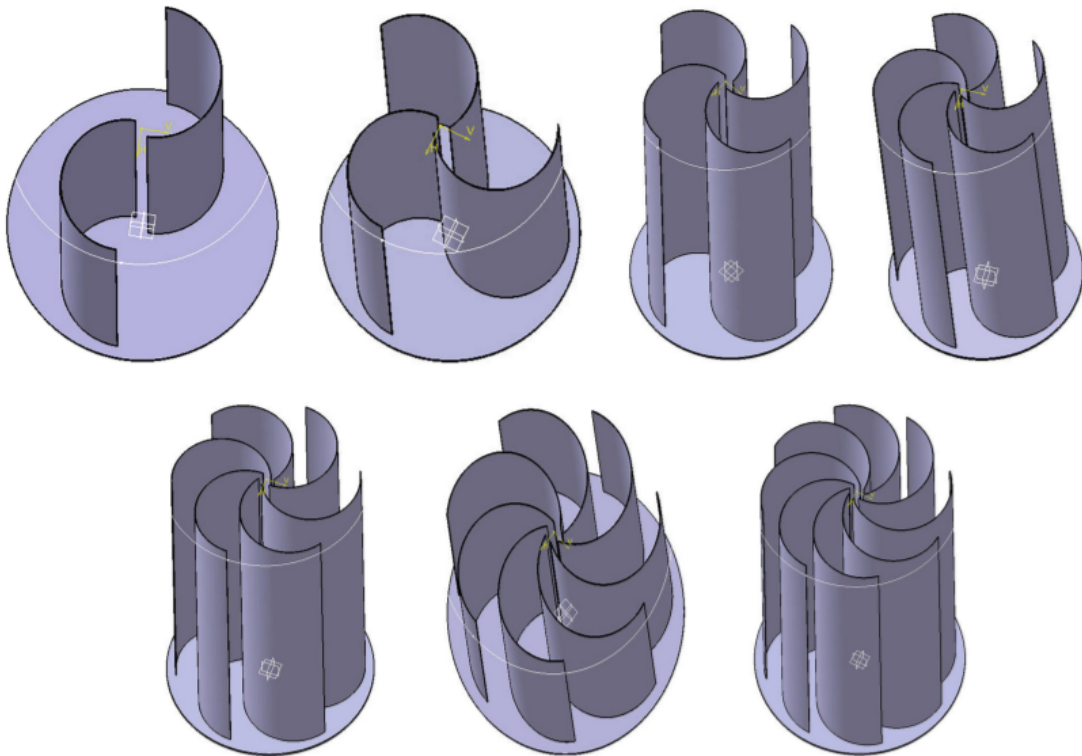
Figure 3.5: Various models with increasing number of blades for Savonius turbine [46].

3.2.2.2   Effect of the end plate

A simple accessory that could be added to a Savonius turbine is the end plate, as already shown in Figure 3.2. Using an end plate with a size of 1.1 times the diameter

of the turbine significantly improves the performance of a Savonius turbine [44, 47–49]. It helps to prevent the flow from escaping from the concave side of the advancing blades to the outside flow, which increases the pressure difference on the blades, thus increasing the power production.

3.2.2.3 Influence of the overlap and gap ratios as well as the arc angle

The description of overlap, gap ratios, and arc angle configurations are presented in Figure 3.2. To understand the effect of these parameters on performance, let us look at the flow pattern in Figure 3.3. While the small space between the blades leads to flow passing between those (overlap flow (III), as shown in Figure 3.3), the arc angle controls the vortex at the end of the advancing and returning blades. Controlling both of these parameters is very important for improving the performance of the turbine. The gap increases the pressure on the returning blades on the convex side; this is its advantage. On the other hand, it also helps the flow to escape from the advancing blade, which decreases the power produced. While these parameters affect the flow structure around the turbine, there is no consensus among the results in published research, and there are only few publications that address the arc angle. Some studies stated that the gap, as well as the overlap ratios, should be zero [50]. Other studies stated that the gap ratio should be zero but with an optimal overlap varying widely from 0.15 to 0.3 [51]. Some other researchers recommend that this range should be from 0.1 to 0.15 [45]. The optimal arc angle for a five-blade hydrokinetic Savonius turbine was found to be 70° in [52]. The blade overlap ratio, arc angle, and aspect ratio were studied simultaneously in [53]; the output power coefficient was increased by more than 24% compared with a classical shape. Due to controversial findings, in this thesis, this point will be investigated in detail, and the three parameters will be optimized together.

3.2.2.4 Effect of the blade shape

One particularly promising improvement relies on a modified blade shape. Figure 3.6 shows various blade shapes used in the past for Savonius turbines. While the first shape is the standard for a Savonius turbine, the remaining shapes are variant forms. As stated in various studies, all of these modified shapes produce more power compared to the standard shape [54–60]. The largest improvement was found by using an elliptical profile, which improved C_p by 10.7% over a semicircular profile [61]. The numerical optimization of the elliptical profile numerically produced an improvement of 18.2% compared to the semicircular-bladed Savonius rotor [62]. Moreover, six parameters were considered in an optimization process to improve the blade shape in [63]. The most important studies are summarized in Table 3.1, showing that extensive work has already been done to optimize the shape of Savonius turbine blades. The initial studies only considered infinitely thin blades, or blades with constant thickness (with the same shape on the convex and concave side). However, the energetic contribution of each side is physically very different. Very recently, researchers have started considering turbine blades with different concave and convex profiles [60, 64]. Only classical airfoil shapes and semi-elliptical blades have been investigated. The blade curvature was described with few geometrical parameters, so that only a limited increase in power coefficient could be obtained until now (4.4% in [60]).

Table 3.1: Selected studies regarding optimal blade shapes for Savonius turbines

Design Modification	Percentage increase in C_p	Method	Description and comment
Optimal blade shape [63]	38.9%	Numerical	Thin blade with deflector
New blade shape [55]	26%	Numerical	Thin blade with different gap and overlap ratios
New blade shape [65]	34.8%	Experimental	Thin blade with different gap and overlap ratios
Airfoil shape with curtain [64]	20%	Numerical	Complex design
Different shapes on convex and concave sides [60]	4.4%	Numerical	Only semi-elliptical shape
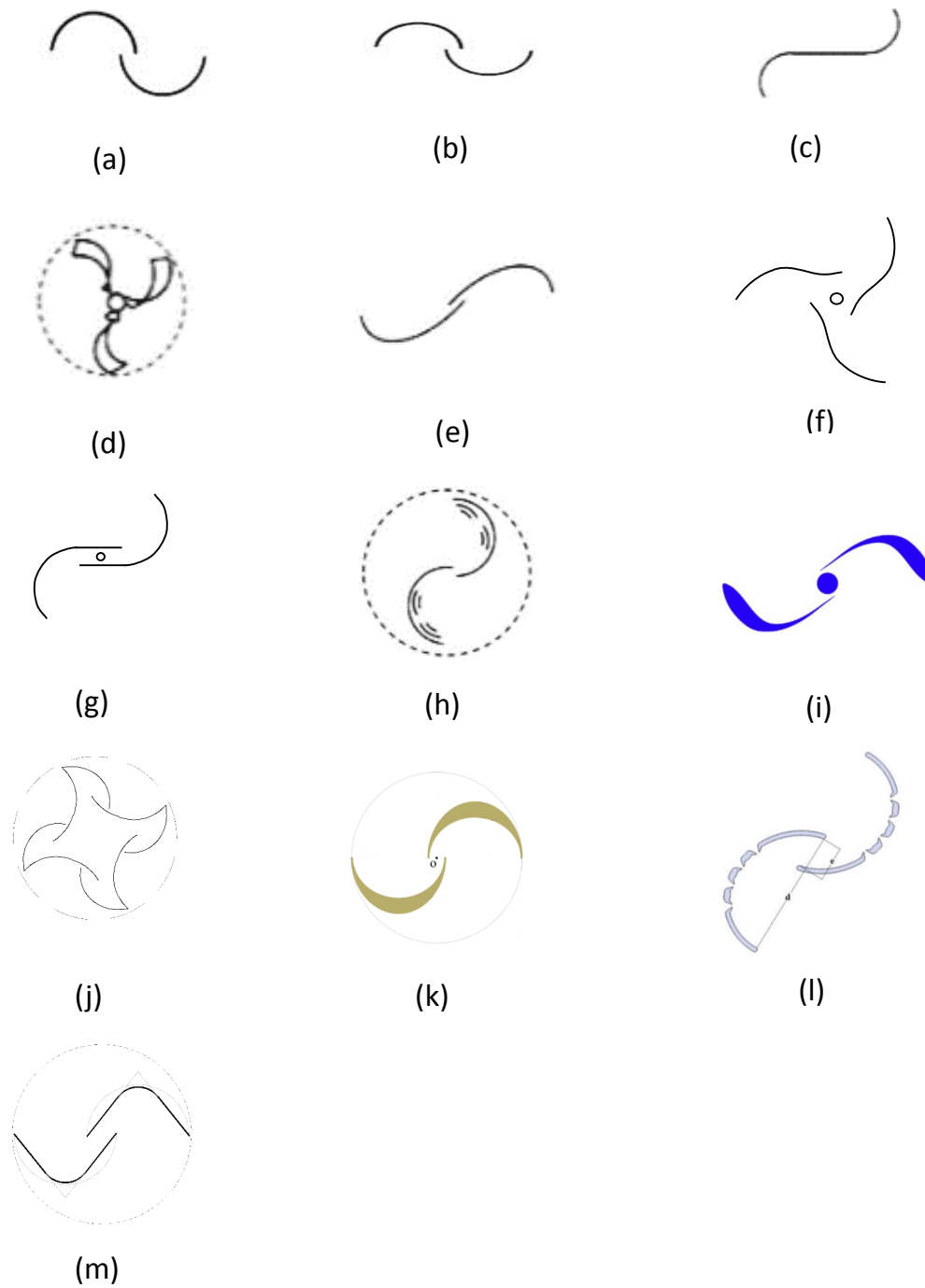
Figure 3.6: Various blade forms for Savonius rotor (a) Standard shape [36] (b) Semi-elliptical (c) Bach [36] (d) Twisted [54] (e) Elliptical [55] (f) Fish ridged [56] (g) Modified Bach [66] (h) Multiple quarter blades [57] (i) Airfoil shape [58] (j) Bronzinus [59] (k) Different concave and convex [60] (l) Elliptical Savonius with four parallel channels [67] (m) V-shape [68].

3.2.2.5 Augmentation of the flow

As presented in the previous chapter,the maximum performance is fixed by the Betz limit at 59.3%. However, this limit could be easily exceeded by using one augmentation technique to capture a large flow area, as discussed below. While this method could optimize the flow quantity and velocity entering the turbine, it can decrease the overall turbine performance depending on the reference area used to compare C_p. Taking that into consideration, the improvement in performance for the next studies is mainly due to an increase in the frontal area of the flow, which should be compared to a large-diameter turbine [69], keeping the Reynolds number constant for a fair comparison [70]. Figure 3.7 shows several augmentation techniques that were used in previous studies, starting with very complex systems such as wind guide augmentation [71], guide box [72], and conveyor-deflector systems [73], and ending with simple augmentation systems like shield obstacles [74], and deflector plates [75]. The main idea of these techniques usually relies on the increase in the mass flow rate through the rotor area. Since the power produced is proportional to the cube of the incoming velocity, a small increase in fluid velocity will lead to a large increase in performance.

On the other hand, using a guiding plate (a deflector shield in front of the returning blade) is an area of interest, especially in conjunction with Savonius turbines, since the returning blade moves against the direction of the flow and thus suffers from high drag, which produces a counter-moment on the turbine, and reduces the power coefficient. An initial study investigating the optimal location for a straight plate found an increase in the power coefficient of 27.3% and 27.5 % for two- and three-bladed wind turbines, respectively [74]. A similar study was later conducted for a two-blade Savonius turbine in water, achieving an increase of about 50 % in the power coefficient compared to a standard one [75]. More power can be generated by using a nozzle or a duct together with a deflector [71, 76, 77]. Table 3.2 summarizes the corresponding results, revealing that extensive studies were conducted involving deflector plates for Savonius turbines.

Though these previous studies revealed promising findings, it must be noted that the power increase was largely obtained by substantially increasing the frontal flow area occupied by the system (turbine + deflector plate). In that sense, a comparison is difficult since the power output of a larger turbine occupying the same space would also be noticeably higher. For a better comparison, the power coefficient could be calculated by exchanging the frontal area of the turbine (indicated by the diameter of the turbine in 2D cases) with the largest area of the system [78]. In this manner, the comparison is improved, but still flawed since this calculation method assumes that

both cases (with an obstacle or nozzle and the standard turbine with a larger diameter) have similar flow structures around the turbine blades, which usually does not happen.
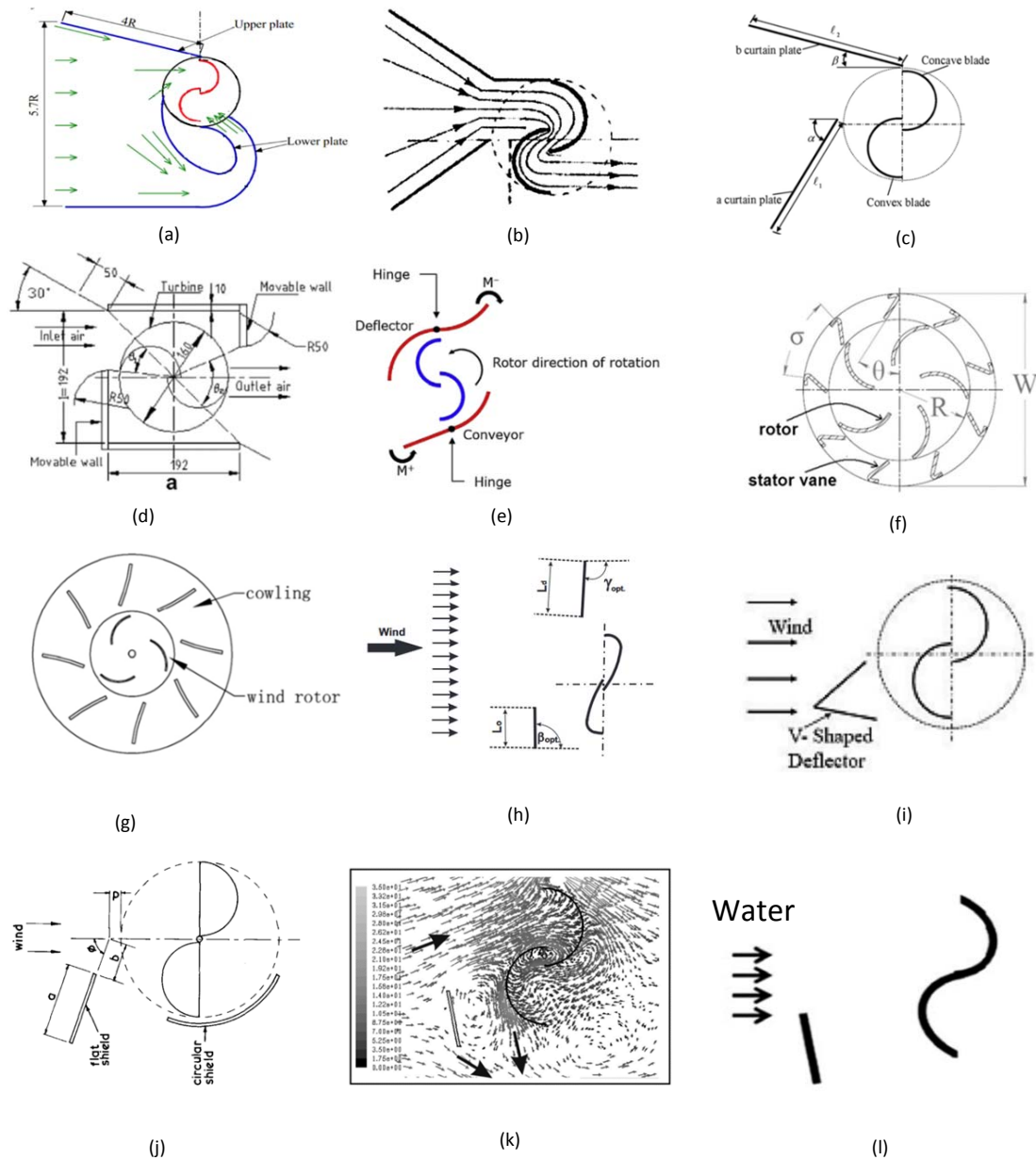
Figure 3.7: Different types of augmentation (a) Wind guide augmentation [71] (b) Nozzle [79] (c) Two curtain plates [80] (d) Guide box [72] (e) Conveyor-deflector system [73] (f) Stator vanes [81] (g) Tower cowling [82] (h) Modified Savonius with guide plates [83] (i) V-shape deflector [84] (j) Flat and circular shield [49] (k) Shield obstacle [74] (l) Modified hydraulic Savonius with deflector plate [75].

26

Table 3.2: Selected studies considering deflector plates for Savonius turbines

Design Modification	Findings	Methodology	Comments
1 straight plate [74]	27.3% increase in power coefficient for 2 blades; 27.5% increase in power coefficient for 3 blades	Numerical	Wind turbine
Curved plates [71]	160% increase in power coefficient for modified Savonius turbine	Numerical	Wind turbine with complex geometry
Curtain design [80]	150% increase in power coefficient	Experimental	Wind turbine
1 straight plate [75]	50% increase in power coefficient for modified Savonius turbine	Experimental	Water turbine, testing only 8 configurations
2 deflector plates [85]	150% increase in power coefficient for modified Savonius turbine	Experimental	Water turbine, testing only 8 configurations

3.3 Scope of the thesis

Using Savonius turbines in water is a current topic of interest. While much of the previous research is based on parametric studies, few recent studies recently have taken the full optimization process into consideration. Therefore, in this thesis, several new ideas (derived from a good understanding of the flow structure as well as improvements made in previous studies) will be experimentally and numerically analysed in order to improve the performance of such a turbine. However, before starting the optimization process, the numerical model should be validated using experiments conducted in this thesis as well as using previous experimental data from the literature, in order to finally optimize the configuration.

The optimization process has been divided in these steps:

1. **Optimization of thick blades**

   As is apparent from the previous discussion, extensive work has already been done to optimize thin Savonius turbine blades, keeping the same shape on the convex and concave sides. However, the energetic contribution of each side is physically very different, so that changing the thickness can produce higher torque. Up to now, only classical airfoil shapes and semi-elliptical blades have been investigated. The blade curvature was described with few geometrical parameters so that only a limited increase in power coefficient could be obtained in this manner (4.4% in [60]). Therefore, in order to evaluate the full potential of such arbitrary shapes, the number of geometrical parameters used to describe both blade sides during optimization must be increased. Of course, this requires a far higher number of CFD simulations in order to meaningfully explore the resulting, very large parameter space. For this purpose, several geometrical parameters are used in the research presented here to describe the shape of the blades, allowing the concave and the convex sides to be optimized independently; this will be presented in the next chapters.

2. **Optimization of a deflector plate in front of the turbine**

   Using such deflectors for wind turbines is not promising, since the wind direction cannot be easily predicted and changes rapidly. The situation is different in water, and most hydropower sources can be considered as having a uni-directional flow. Additionally, employing a deflector plate in water can be used to protect the blades from suspended solids and floating debris. This is particularly important for the returning blade, which is associated with a higher impact velocity. Therefore, the interest in a deflector plate for hydropower Savonius turbines is driven by two factors: 1) increase power production, 2) protect the returning blade from impacts. Optimizing the deflector in front of the returning plate will be one of the targets in this research. At the difference of previous works the present study considers an optimization process for the shape and the position of a thick deflector plate upstream of a hydraulic Savonius turbine but keeping a constant frontal area (no enlargement).

3. **Optimization of the three main parameters: overlap ratio, gap ratios, arc angle**

   As there is no consensus in their literature concerning this optimal value, in this study, these three main parameters are simultaneously optimized to obtain the

complete optimal configuration of a Savonius turbine using water as a working fluid.

Before all of these optimization processes are discussed the optimization process procedure will be presented in the next chapter, in order to understand how and how many processes need to be investigated in order to determine the final, optimal version of the turbine.

Chapter 4

Introduction to Optimization

Optimization is the process of determining the best solution for a given problem. Nowadays, optimization is a topic of interest in every field; e.g. science, engineering, and business. In business, maximizing profit by decreasing the resources used, and minimizing operating costs is the primary target for all management systems. In the engineering field, improving the efficiency of any production device is one of the most important revenues for competition between companies. There is an infinite number of similar examples in real life. The optimization process has evolved over time. For many years, the optimization process was conducted by using a trial-and-error methodology. While this method can be sufficient when only a few values of the input variables are possible, in real life, each problem has many variables that affect the output (and then the optimal condition). Since turbulence in fluid mechanics is a chaotic process, finding the optimal values becomes even more complicated in fluid mechanics applications similar to this case [86–88]. Therefore, to take full advantage of the power of optimization, there is no choice but to use a computer- and in some cases high-speed computers- to find the optimal conditions.

Since this project uses an in-house optimizer code, in this chapter the fundamental background of the implemented optimization process will be discussed. Moreover, the genetic algorithm, which will be used in the upcoming chapters, will be presented in detail.

4.1   Definition of the optimization problem

From a mathematical point of view, optimization simply consists of maximizing or minimizing one or more objective functions for a given system. For a better understanding, assume that there exists a function or problem O which is affected by k

number of parameters, as shown in equation 4.1. The input parameters are represented by $x_1......x_k$, and O is the objective function. Minimizing or maximizing O is the optimization process. In other words, $(x_1......x_k)$ are the variables that could be changed to get the optimal condition (max or min) of the O function. While $g(x)$ and $h(x)$ are called behavioral constraints, the maximum and minimum value of any x_i (input parameter) are called side constraints. Any set of the input parameters that fully satisfies all of the constraints is called a feasible solution, even if it does not minimize or maximize the objective function [89–92].

Minimize or maximize

$$O = f(x_i) \quad (i = 1.....k) \tag{4.1}$$

Subject to:

$$\text{Constraints} \begin{cases} g_j(x) \leq 0 & j = 1....l & \text{Inequality constraints} \\ h_m(x) = 0 & m = 1.......w & \text{Equality constraints} \\ x_i(\text{min}) \leq x_i \leq x_i(\text{max}) & & \text{Side constraints} \end{cases} \tag{4.2}$$

4.1.1 Classification of the optimization problem

From the above discussion, any optimization problem could be classified into different categories:

1. **According to the number of objectives**

   - Single-objective: There is only one objective function.
   - Multi-objective: There are several objectives to maximize or minimize simultaneously; e.g., maximize the efficiency and simultaneously minimize the cost of the product.

2. **According to the presence or absence of constraints**

   From the name, it is clear that when any of the input parameters have constraints, it is called a constrained problem, otherwise, it is called an unconstrained problem.

3. **According to discretization variables**

   If any of the design variables is a discrete variable, then it is no longer a continuous optimization problem. Therefore, it will fall under one of three different cases as follows:

- Binary programming: the variable takes the value 0 or 1.

- Integer programming: the variable is restricted to take an integer value [93, 94].

- Discrete optimization: the design input parameter is restricted to take some specific real values.

  In a few real applications, a mixture between the above types of binary, integer, discrete, and continuous variables can be found in the same problem [95].

4. **According to modality**

   In a single-modal problem, only one optimum exists. On the other hand, a multi-modal problem has more than one optimum. From an engineering point of view, there are many problems that are multi-modal. Depending on the case, either only one solution can be selected as a final, optimal solution, or all of the optimal values can be kept as solutions.

There are additional possible classifications, e.g. linear and non-linear processes or simple and complex problems, that will not be discussed in this thesis [91].

4.1.2 Global and local optima

Figure 4.1 shows the difference between the global and local optimal values. While the highest value in the feasible solution domain is called the global optimal, the best value in a specific range is called a local optimal value. When using a traditional search method (e.g. a trial-and-error method), the optimizer can get stuck on the local optimum. However, the goal is to get the global optimal value.

4.2 Solution approaches

After defining the optimization problem, several general approaches could be applied to get the optimal solution, as follows:

- **Experimental approach (parametric study)**

  Despite the name, it is also possible to use numerical simulations for this approach. Usually, it is based on experience and trial-and-error. It consists of the following steps: 1) build up the physical model, 2) evaluate its performance ; 3) change the parameters and evaluate the new performance, stopping once a sufficient quality was satisfied. The disadvantage of this approach is that it is very
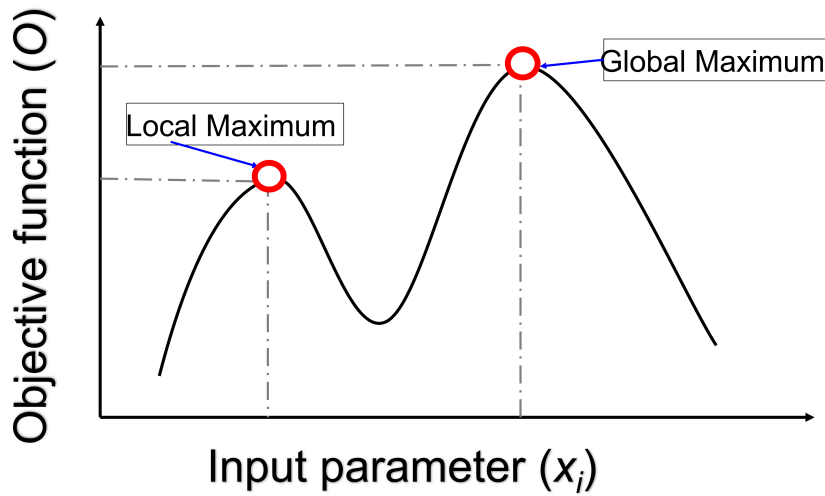
Figure 4.1: Local and global optimal.

costly, needs a lot of numerical time, and can be stuck on the local optimum, as shown in Section 4.1.2.

- **Analytical approach**

  This model is only useful when known mathematical functions relate the objectives and the input parameters; this is practically never found in real problems involving fluid mechanics.

  However, this approach can be helpful for understanding and developing the numerical model or the algorithm, as discussed later.

- **Graphical approach**

  One of the optimization approaches used is the graphical approach, which is simply drawing the function and determining the optimum from the graph. In order to understand this method, assume an optimization problem [91],

$$f(x) = x_1 + 2x_2 \tag{4.3}$$

Subject to:

$$\text{Constraints} \begin{cases} x_1^2 + x_2^2 - 1 \leq 0 & \text{Inequality constraints} \\ -1 \leq x_1, x_2 \leq 1 & \text{Side constraints} \end{cases} \tag{4.4}$$

where the objective is to minimize $f(x)$. Now, if this function is sketched with the constraints defining the feasible region as well as the side constraints, as shown

in Figure 4.2, the x-axis represents the first input parameter x_1, the y-axis shows the second input parameter x_2. The inclined dotted lines represent the objective function values $f(x)$. The circle in the middle of the graph represents the feasible solution. When searching for the minimum value of the $f(x)$ inside the feasible region, O^* is the target point, and the minimum value of $f(x) = -2.24$. The input parameters at this point are $[x_1, x_2] = [-0.4472, -0.8944]$.
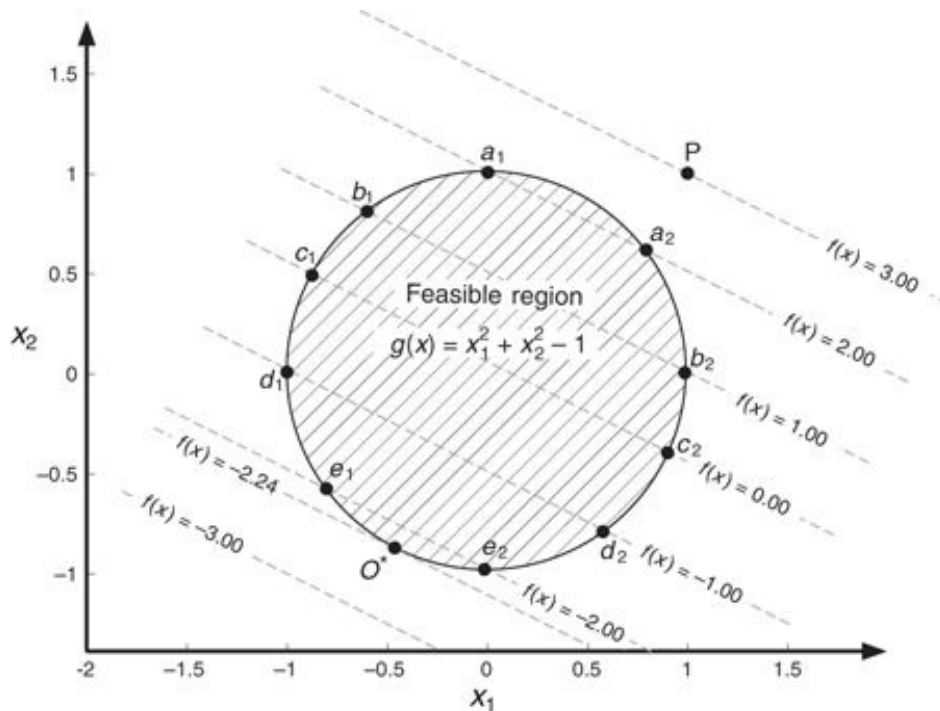
Figure 4.2: Example for the graphical optimization approach [91].

It is clear that, as the number of variables increases, using this approach will become more complicated. Moreover, more constraints will lead to complications in finding feasible regions. This approach is only useful for small numbers of variables with few constraints, and analytical formulations. This is not relevant for fluid dynamics applications.

- **Numerical approach**

  After several decades of research, optimized values can be identified without using the manual approaches but by using algorithms (machine learning). This method is dependent on an algorithm to find the optimal solution. Of course, depending on the quality of the algorithm, the optimal solution can be found more quickly and/or in a more robust manner.

In this approach, the optimizer starts with the initial (suboptimal) design. According to the algorithm, it starts to generate the next, and hopefully improved, design. Then, the optimizer continues iterating until it reaches the optimal design or satisfies the quality being targeted.

For example, consider the problem:

$$f(x) = (x_1^2 + x_2)^2 + 3x_2^2 \tag{4.5}$$

Subject to:

$$\text{Side constraints} \begin{cases} -1 \leq x_1 \leq 1 \\ -0.5 \leq x_2 \leq 0.5 \end{cases} \tag{4.6}$$

where the objective is to minimize $f(x)$. Figure 4.3 shows the methodology of the numerical approach used to obtain the optimal design. While the two axes represent the two input variables, the contours show the objective function values. Each point in the figure represents an iteration of the optimizer. The optimizer will start with a very suboptimal result as an initial point, then each iteration produces a progressively better result until it reaches the optimal design values, as shown by following the path indicated by the arrow. A numerical approach has a limited accuracy. Therefore, it will give an approximation of the optimal value. Here the optimal value for this function is $x_1 = x_2 = 0$, however, the optimizer may give for instance x_1 and x_2 of the order of 10^{-6}.

There are several algorithms that can be used for such a numerical approach. In CFD-based optimization (CFD-O), the most popular approaches are based on evolutionary algorithm (EA) [96], more specifically genetic algorithms(GA) [92].

4.3 Evolutionary algorithms

Evolutionary algorithms (EA) are computer programs that attempt to solve optimization problems by simulating the processes of Darwinian evolution [97]. EA starts the process by selecting a random or a quasi-random initial population size of N individual, which is called a generation. Then, the optimizer calculates the fitness score of each individual using the fitness function. A population member with a high fitness score is a better solution than an individual with a lower fitness score in each generation. After calculating and sorting the individual by their fitness score, the optimizer
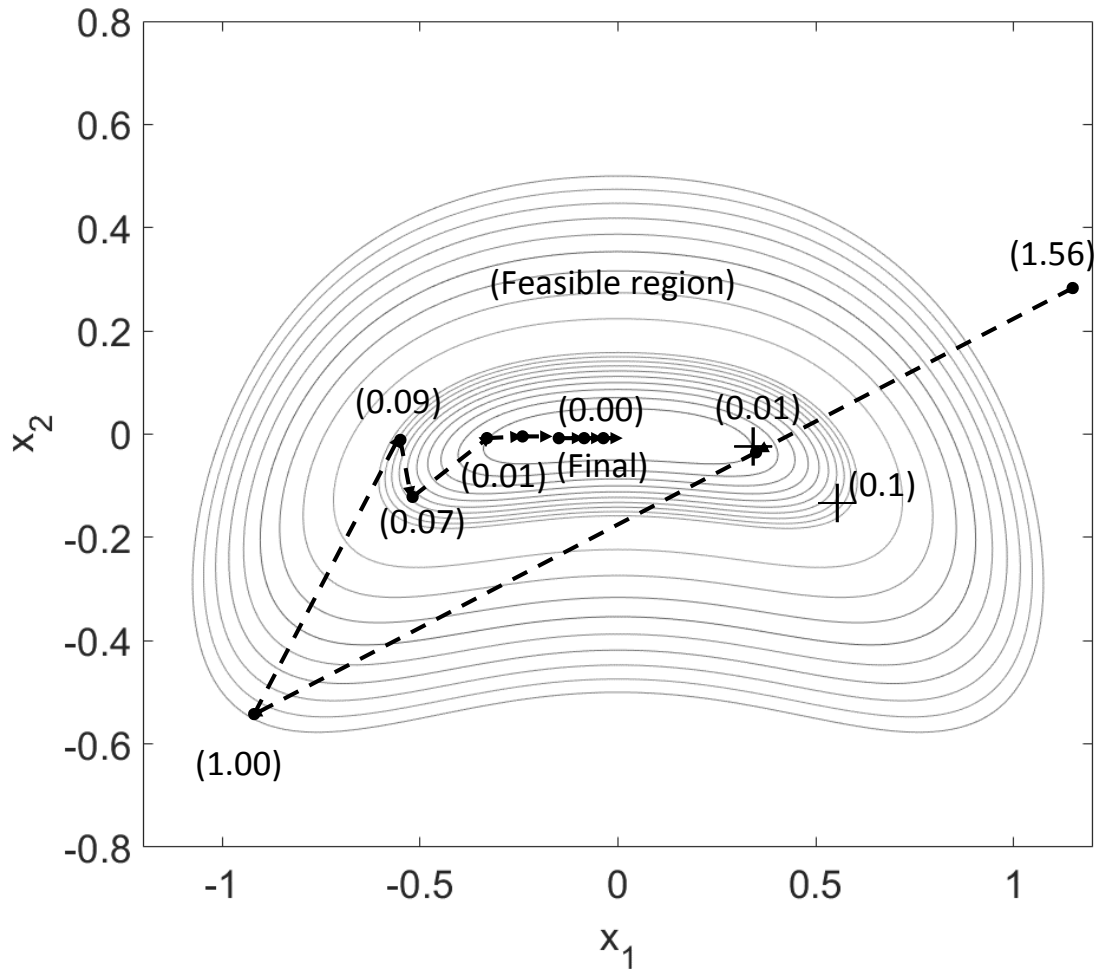
Figure 4.3: Example illustrating the numerical optimization approach [91].

starts to calculate the next generation by using mutation and cross-over functions favoring individuals with a higher fitness. Once the new generation is generated, the optimizer once again calculates the fitness scores, and repeats several iterations of the steps decried previously to get the optimal design.

4.3.1 Genetic algorithm (GA) and application in OPAL++

A genetic algorithm was first introduced by J.H. Holland [98–100]. OPAL++ is an in-house programming language used for optimization of several fluid mechanics problems. The genetic algorithm is based on the creation of parents (first generation) and children (next generations). According to the parents' fitness scores, the optimizer calculates the children. Then, the children become parents to the new generation, and this process is repeated to get the optimal design. Figure 4.4 shows a flow chart of the genetic algorithm procedure. The process starts with obtaining the initial population and then the optimizer calculates the fitness score of these individuals. The optimizer

will classify high-fitness score individuals as elite, and divide the rest into two groups: one group for the crossover operation and a second one for the mutation operation. After the processes of crossover and mutation, the new generation is now ready, and the same steps are repeated again.

For better clarity, Figure 4.5 shows the crossover and mutation processes. During crossover, a part of an encoded string for two individuals is exchanged. For example, the first two strings from two individuals were exchanged to produce the children. The SBX (simulated binary crossover) method is used for crossover in OPAL++ [101]. During mutation, a mutated child is generated from a single parent, then one string in the parent is mutated to a new value. This allows avoiding convergence towards a local optimal value; instead, the global optimal value should be reached.

The genetic algorithms are applied in OPAL++ as follows:

- All variables have a real representation.

- Each generation contains N individuals.

- SBX is used for crossover calculations [101]

- A polynomial mutation is applied [102, 103].

- Elitist selection is applied. Individuals are immortal to preserve information, but only the best N individuals survive. All further details can be found in [104]
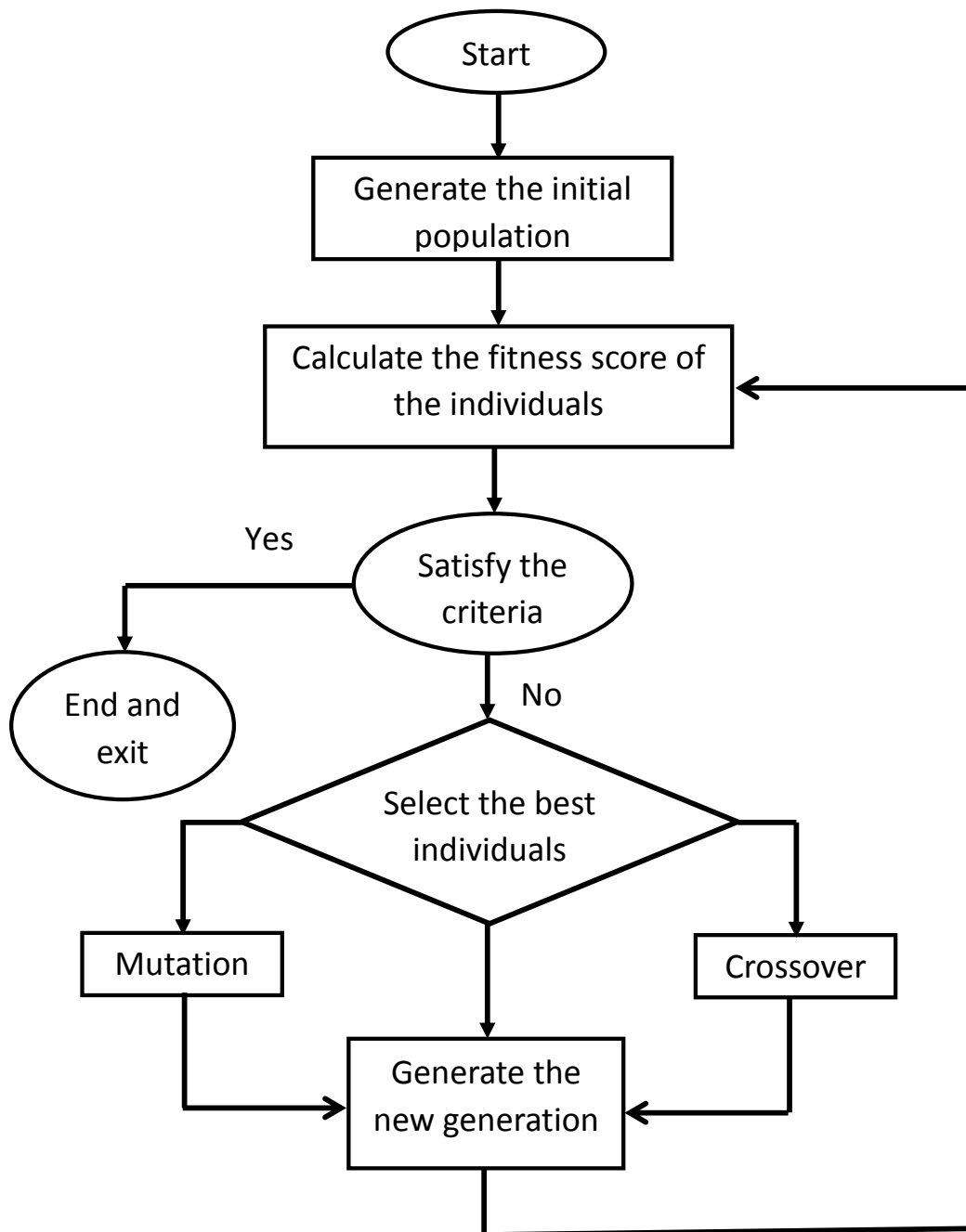
Figure 4.4: Flow chart for the genetic algorithm.
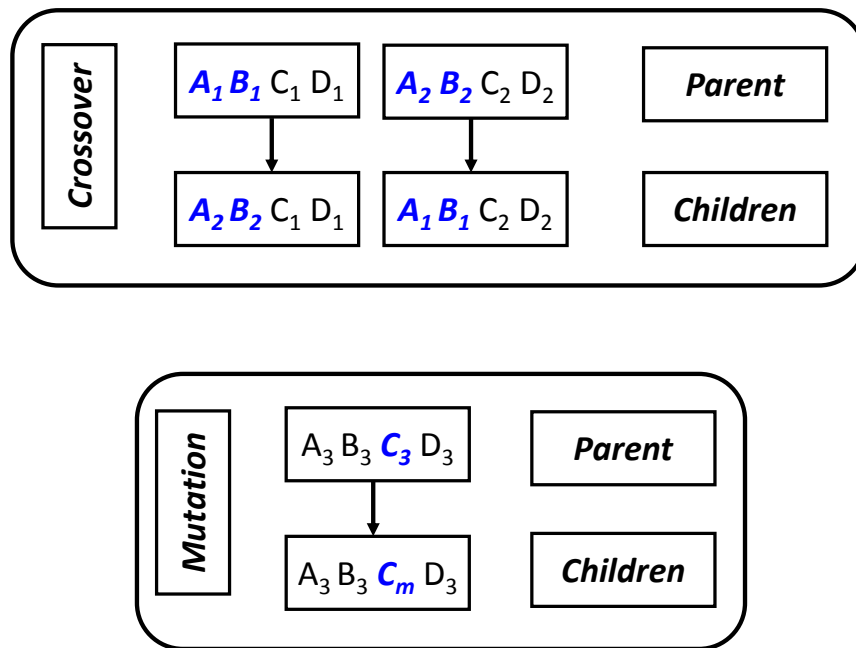
Figure 4.5: Illustration of the crossover and mutation processes.

4.3.2 Summary

Most optimization processes show local and global optimal values. When using traditional optimization methods, the optimizer could converge toward a local optimal value. Genetic Algorithms are able to escape local optimal values. Additionally, they are robust, tolerating faulty or missing evaluations. For this reason, GA will be used in the upcoming chapters.

Chapter 5

Methodology

5.1   Introduction

In order to be sure that the optimization procedure delivers the right optimal results, computational fluid dynamics (CFD) should produce a very accurate description of flow structure and performance of the turbine. From older studies, it is clear that producing a highly accurate flow structure for a Savonius turbine is a very challenging task as the flow is of a highly time-dependent nature and involves flow separation around the turbine blades. Therefore, verification of the simulation process as well as validation for the turbine will be discussed in detail. Not only will validation based on the literature review be discussed but also validation of the CFD by using results from own experiments conducted for this thesis, ensuring that the CFD produces very accurate results and can be used in the optimization process. Accordingly, the first part of this chapter will discuss the verification and validation of CFD from literature. The second part will present the experimental methodology and the validation of the CFD using own experimental results. In the end, the procedure for using CFD in an optimization process will be discussed. Part of this chapter is based on previous publications [105–107].

5.2   Numerical flow simulations

The industrial CFD code Star-CCM+ was used to investigate the flow structure and to calculate the power coefficient C_p for each blade geometry. By neglecting flow structures appearing at the end of the blade, 2D simulations through the mid-section plane of the turbine deliver results relevant to real, 3D Savonius configurations; since in most practical cases end plates are used in real systems, 3D effects can be considered to be of minor importance. Such 2D simulations have been used successfully in almost every

previously published studies concerning Savonius rotors [60, 63, 108, 109], compared to only very few 3D studies [110, 111]. Considering that a single 3D simulation requires a huge computational time, it would be completely impossible to rely on 3D configurations for optimization, since the optimizer requires as many as 2000 CFD simulations. Additionally, the results of the current 2D numerical model have been successfully validated using existing experimental data. That does not mean that 3D simulations will be neglected; the same physics and mesh constructions were used at the end to create 3D simulations that were compared with the results from the experimental set-up, ensuring a posteriori that the results from the simulations could be effectively used in the optimization process. Overall, it is clear from a recent study that 2D simulations produce more interesting results compared to 3D simulations [112] due to limitations in the computational power. Therefore, the optimization process will be conducted using many 2D simulations while the experimental setup will be used to validate the few 3D simulations and the output from the optimization process.

5.2.1 Computational domain and boundary conditions

To simulate this configuration, the numerical domain is divided into two sub-domains: a rotating domain around the turbine and a very large fixed domain, as shown in Figure 5.1. Classical boundary conditions are employed: a velocity inlet on the left side, a pressure outlet on the right side, symmetry lines at the upper and lower sides, and no-slip walls along the blades. An overset mesh is used at the boundary between both domains. The overset mesh method is a powerful tool for simulating motion within a CFD analysis [113].

The size of the overall domain is $30 \times D$ from left to right and $20 \times D$ from bottom to top. This is necessary in order to be sure that the influence of the boundary conditions on C_p is negligible [63].

5.2.2 Discretization in time and space

During optimization, each blade geometry must be evaluated using a dedicated CFD simulation. Each CFD simulation was systematically carried out over a total of at least 10 complete rotation periods. The average power coefficient is computed for each cycle independently. The CFD simulation was stopped when, after 10 cycles, the relative change of the average C_p between two consecutive cycles stayed below 1%.

At the very beginning of the simulations, the flow field is far from realistic. In order to speed-up convergence toward the physical, periodic solution, a two-level approach was applied to select the time step. In the first phase, during the first five rotations, a
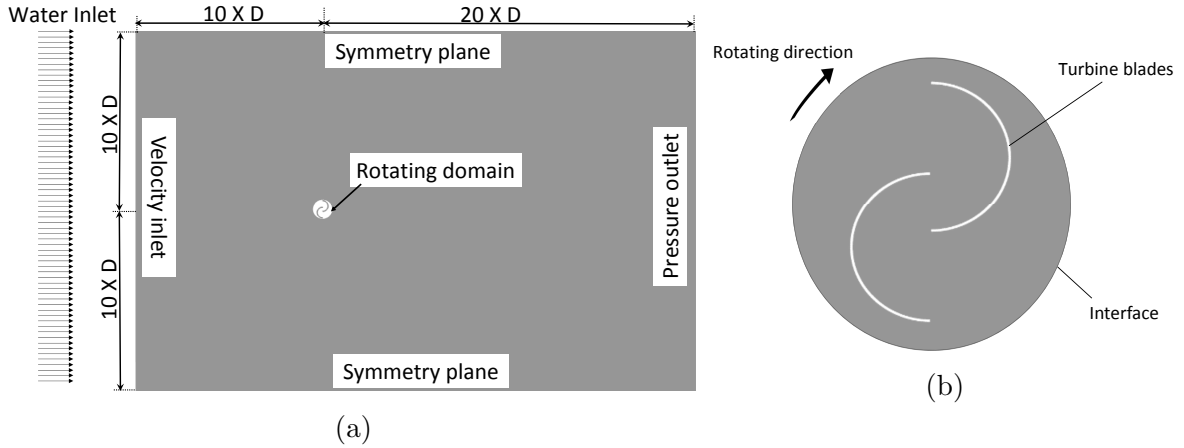
Figure 5.1: Simulation domains. (a) Overall domain, (b) Rotating domain, centered at the turbine's center and of radius $1.3 \times R$.

coarse time step corresponding to 5°/step was used to get a rough approximation. In the second phase, accurate results must be obtained from the coarse ones; therefore, suitably short time steps of 0.5°/step are used, as illustrated in Figure 5.2. In this way, it is possible to noticeably speed up the overall process while obtaining highly accurate results, as already discussed in [114]. The values of C_p discussed afterwards correspond systematically to the average value obtained during the last rotation computed by CFD.
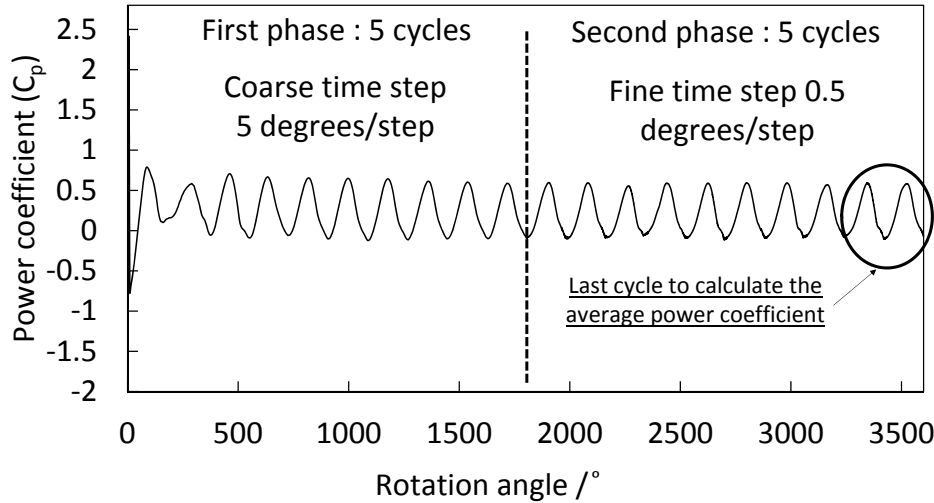
Figure 5.2: Example evolution of the power coefficient C_p during 10 rotation periods for $\lambda = 1$.

A special case occurs when using a deflector plate at the front of the turbine. Due to the expected occurrence of vortex shedding behind the deflector plate and behind the turbine blades, the average value of the power coefficient for just one rotation period will fluctuate within a specific range. This effect can be seen in the supplementary

43

Video (1) provided with this thesis. Figure 5.3 shows typical oscillations of the average power coefficient for the turbine using a specific configuration for the deflector plate over a simulation for 100 complete cycles. As shown, the average power coefficient for each cycle (black square points) shows spurious variations. Therefore, the C_p of one cycle cannot be meaningfully compared to others in the optimization process. In order to make meaningful comparisons, an average value of C_p over several rotation periods must be used instead.

Obviously, the accuracy of this procedure will increase with the number of cycles involved. However, the computational cost of the CFD used to evaluate each design will grow as well with the number of cycles used in the averaging procedure. Therefore, it is necessary to check how many cycles are really needed to get converged averaged values.

The initial 15 cycles will be completely ignored when computing the average power coefficient. The data points shown by grey circles in Figure 5.3 show the average value obtained for a gradually increasing number of cycles, starting from cycle 16. It can be seen that the average value of the power coefficient obtained when using more than 12 cycles starting from cycle 16 (until cycle 27) does not show any noticeable changes (defined here as a relative variation well below 1%) when up to 100 cycles are computed and taken into account. Based on this observation, each configuration has been computed by CFD over 30 cycles in total; the first 15 cycles are removed from the analysis, while the average value of C_p obtained from cycle 16 to cycle 30 will be used for quantifying the quality of this specific design. This allows for fair quantitative comparisons between different configurations.

Figure 5.4 presents the instantaneous power coefficient as a function of the rotation angle for the same configuration as in Fig. 5.3, but now only for the first 30 rotations. In order to speed up the computational procedure, and keeping in mind that the first 15 cycles will be ignored when computing the average value of the power coefficient, a two-level approach has been used, as in the previous section. A coarse time step corresponding to 5°/step is used for the first five rotation cycles, leading to fast but rough results. Afterwards, a well-resolved time step with 0.5°/step is used until the end of the simulation, delivering accurate C_p predictions, as illustrated in Figure 5.2. This two-level approach ensures precise numerical results at acceptable computational cost.

From the literature, it is known that accurate CFD simulations of Savonius turbines are difficult, in particular due to the large flow separations, controlling the efficiency
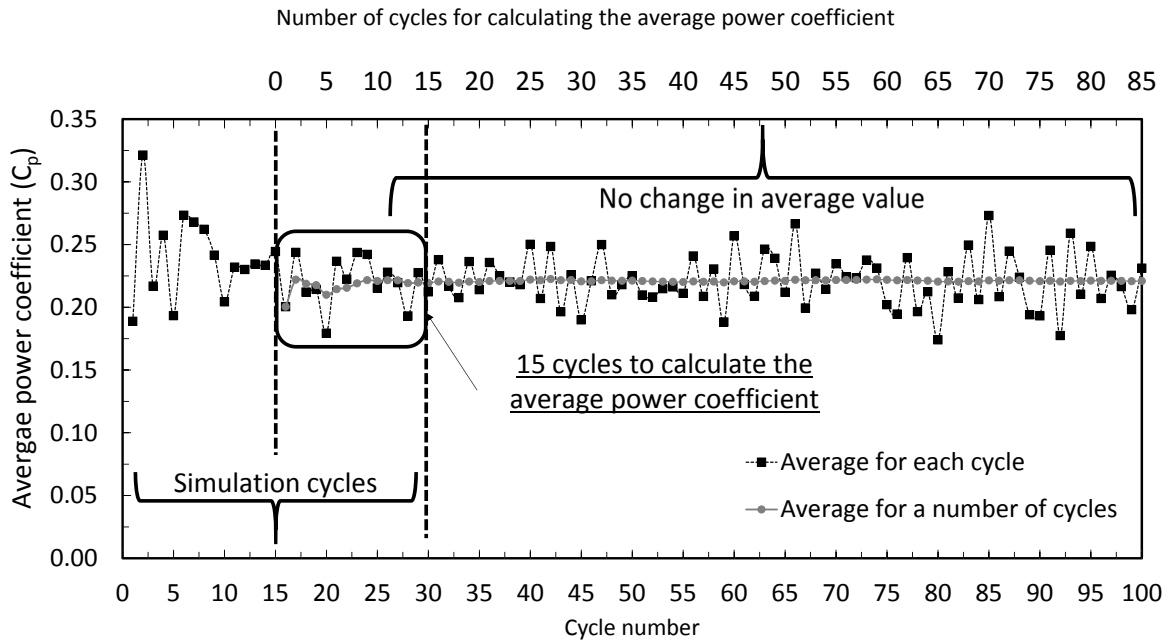
Figure 5.3: Average power coefficient C_p for each cycle over 100 rotation periods for $\lambda = 1$ and a selected deflector plate configuration.
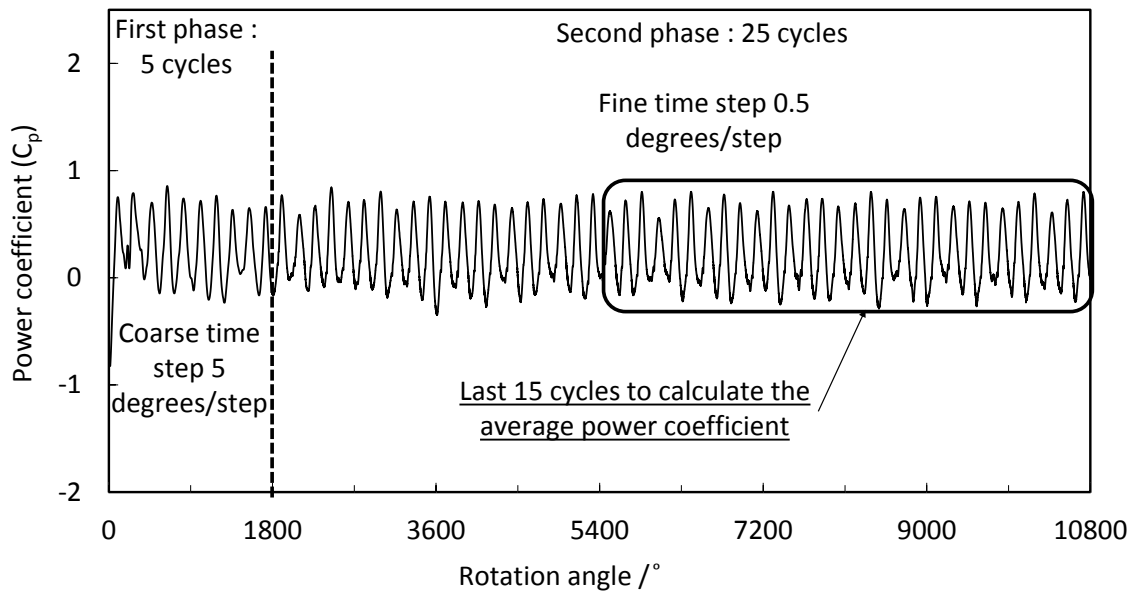
Figure 5.4: Evaluation of the output power coefficient for all 30 cycles for $\lambda = 1$ and for the same configuration as Fig. 5.3.

of the system. Therefore, it is necessary to check the whole CFD procedure with great care. Afterwards, the resulting methodology must be validated.

The mesh size, its quality, and the thickness of the first layer around the turbine blades are the most significant parameters affecting the prediction and must be discussed. Regarding mesh quality, quality reports delivered by the CFD software employed here, Star-CCM+ Version 12.02.11, have been systematically checked; a maximum skew angle always below 40° was assured. The distance of the first grid layer from the turbine blades is quantified by the y^+ value. Therefore, the maximum and average value of y^+ have been monitored during all simulations, and have been found to be ≈ 0.9 and ≈ 0.13, respectively, demonstrating that a very fine near-wall resolution has been achieved. This is also visible in Fig. 5.5.
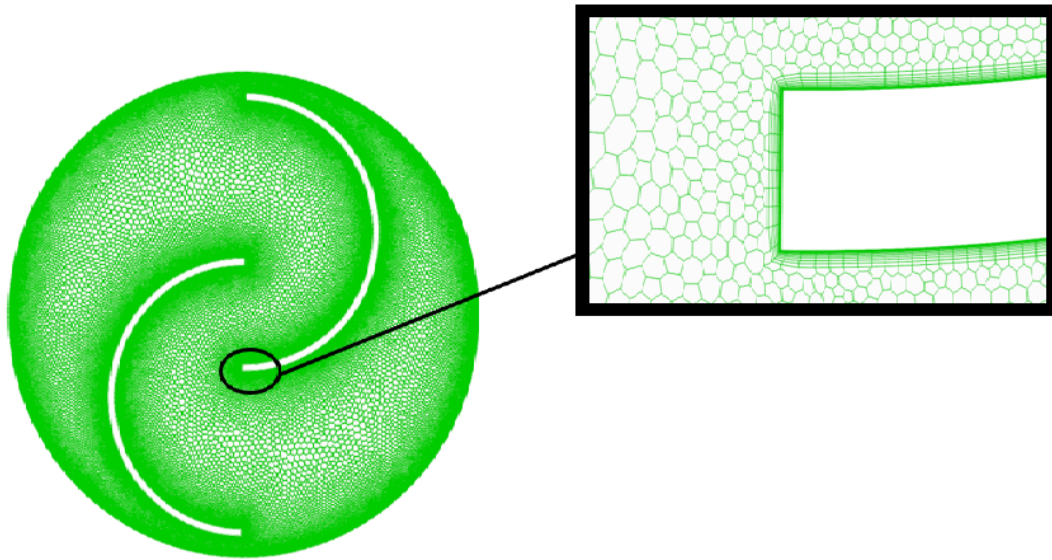
Figure 5.5: Final mesh resolution in the rotating domain and near the blade for the standard Savonius design.

Concerning now the overall mesh size, the result will be usually more accurate for a finer mesh, but the simulation will need a longer computational time, hindering the proper exploration of the parameter space during optimization. The study concerning mesh resolution was conducted for the standard Savonius design at $\lambda = 1$ and for three different mesh densities, as documented in Table 5.1. By setting the maximum acceptable difference to 1%, it can be seen that, while the relative error between mesh 1 and mesh 2 exceeds this tolerance, the error between mesh 2 and mesh 3 becomes acceptable (below 0.5%). Accordingly, mesh 2 with about 400,000 cells has been systematically retained for all later simulations; the exact number of cells obviously depends on the blade shape. The resulting mesh in the rotating domain is visible in Figure 5.5 for the standard Savonius design.

Similar to the mesh density, the time step has also an influence on the performance

Table 5.1: C_p obtained as a function of mesh density

	Number of cells in rotating domain	Number of cells in fixed domain	Total number of cells	C_p	ΔC_p
1	68,895	169,164	238,059	0.2337	6.6%
2	97,498	297,007	394,505	0.2192	0.49%
3	149,093	569,726	718,819	0.2203	0.8%
4	223,777	1,100,903	1,324,680	0.2181	—

calculation from CFD. In addition to the two-stage approach discussed previously, the impact of the time step in the second stage was investigated over the range from 0.25°/step to 5°/step. As shown in Table 5.2, and taking the solution with the shortest time step as a reference, it can be seen that the difference in C_p is less than 1% for 0.5°/step, while it exceeds this threshold for the two larger time steps. Therefore, a time step of 0.5°/step has been systematically retained for the second phase.

Table 5.2: C_p obtained as a function of time step during second stage

Time step (in °/step)	C_p	ΔC_p
0.25	0.2186	—
0.5	0.2192	0.2 %
1	0.2107	3.1 %
5	0.2112	3.0 %

5.2.3   Validation

A topic of interest is the validation of hydraulic turbine simulations. There are two possible procedures: 1) using existing experimental data from the literature, or 2) building a new experimental setup. Each method has advantages and disadvantages. Usually, it is sufficient to validate the simulation with existing experimental data from the literature. However, certain small details about the experimental conditions can not always be found in the published article, for example turbulence conditions, or bearing friction. This could lead to small uncertainties at each measuring point, which is a disadvantage of using this method. Usually, a new experimental setup is more convincing, because it is possible to have similar conditions for both the simulation and experiment. As validation is critical to any simulation, therefore for the optimization

process, validating the simulation twice (both from existing published data, and from experiments in our own water channel) will result in greater precision. Moreover, this offers a good opportunity to validate the optimization process, as the base case and the optimal condition will both be compared in the same experimental setup. The second question is whether or not to use 2D simulation or 3D simulation. While the reality is that 3D flow conditions exist around the turbine, it is impossible to perform the optimization process using 3D simulations. Each optimization requires many simulations to get the optimal case; therefore it is necessary to perform the optimization process using 2D simulations in order to test more cases and use the computational time more efficiently. To solve this problem, validation with the existing data from the literature was carried out for 2D simulations (similar to the optimization process), while a 3D validation was conducted using our own experimental data. Consequently, 2D and 3D validations were both used in the first step for different experimental data to check the simulation's accuracy, and then the optimization processes were performed by using a 2D simulation; then at the end, a last 3D validation was performed to check the result of the optimization process.

5.2.3.1 Validation with existing data from the literature

A first validation of the CFD model by comparison with the experimental data from [115] was carried out. Geometrical and process parameters from [115] were retained, but in a two-dimensional configuration. Figure 5.6 shows that the $k - \omega$ SST model combined with the proposed numerical setup delivers a good agreement with the experimental data in the range $0.6 \leq \lambda \leq 1.2$. The later optimization was carried out for a specific value of the tip speed ratio, $\lambda = 1.1$, for which very good agreement with the experimental results is observed. After optimization, the performance of the standard and optimal shapes will be checked and compared for a typical range of operation, $0.6 \leq \lambda \leq 1.2$, for which validation has been properly conducted. For $\lambda > 1.2$, the difference between the CFD model and experiments increases and reaches a maximum value of about 7% at $\lambda = 1.5$. The increasing error at higher λ may be due to various reasons. First, when the velocity is increased, the free water surface in the experiments may strongly oscillate as waves, which is not considered in the numerical work presented here. Secondly, more complex three-dimensional flow structures may occur, which cannot be represented using 2D simulations. By considering only the most relevant range $0.6 \leq \lambda \leq 1.2$ in the optimization, an error below $\approx 1\%$ is obtained throughout, which is fully sufficient for the purpose of optimization.
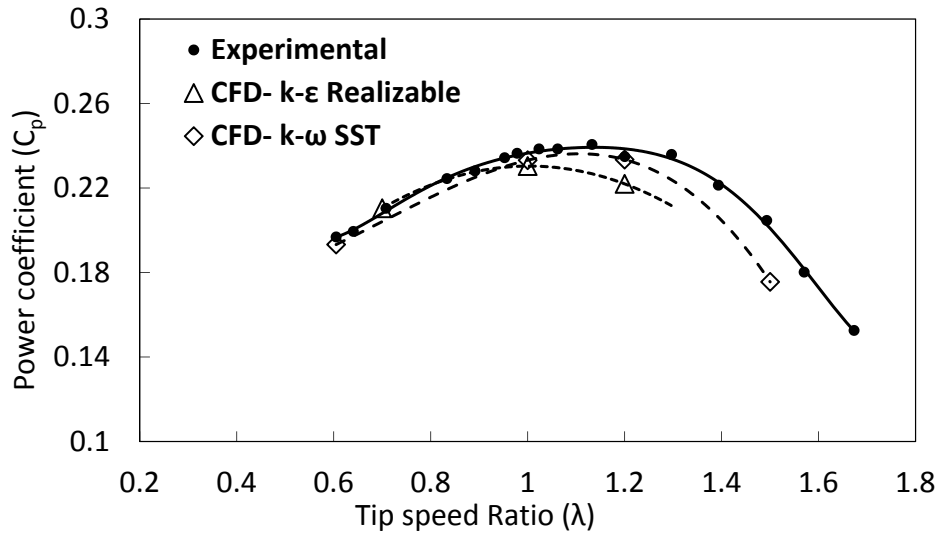
Figure 5.6: Comparison of experimental (from [115]) and numerical values of the power coefficient C_p.

5.3 Experimental work

In this section, the experimental methodology and its results will be illustrated. After first explaining the methodology, the outcome of this research will be discussed and compared with the simulation results. The methodology section will discuss the position of the turbine and the equipment applied. While PIV is used to measure the flow structure around the turbine, a very accurate torque sensor is used to measure the torque and rotational speed of the turbine. The results section will be divided into two parts: the flow field behind the turbine, and then the extracted power together with torque and the corresponding rotational speed.

5.3.1 Water channel

The water channel at Otto von Guericke university in Magdeburg, Germany was used to conduct these experiments and to measure the performance and the flow around the turbine. Figure 5.7 shows the water channel, which consists of three main parts: the inlet, test section, and outlet. The lower tank contains 100 m^3 water with four submersible centrifugal pumps under the floor of the lab, with a smaller tank to receive the water on the lab floor, as shown in Figure 5.8. The frequency of three of the pumps can be simultaneously varied to change the flow conditions inside the channel, while the fourth pump operates at a fixed frequency but can be switched-off. Each pump is connected to a pipe to deliver the water to the water channel. At the inlet level, a honeycomb and a subsequent fine mesh were used to provide less turbulent flow

conditions [116], as shown in Figure 5.9. The dimensions of the test section are 10 m long, 1.2 m wide and 0.8 m in height. It was designed so that the entire 10 m length is a free surface. In this section, the water level was measured by a water level sensor connected to the computer responsible for monitoring the water level inside the channel. The water velocity can reach more than 0.72 m/s in this large cross-section. Moreover, emergency water level sensors were added in this section at different locations for safety so that the water level can not exceed the height of the channel, as shown in Figures 5.9 and 5.10. After the water passed through the test-section, it flows through the outlet, which consists of a weir and return pipes connected to the tank. The weir is a system designed from several rectangular blades 0.025 m in width and with the exact height of the water channel. They are placed vertically side by side and can rotate around the vertical axes. A step motor was used to drive this movement, and it is measured and recorded by a computer, as shown in Figure 5.10. In this way, the operation requirements can be easily obtained. Therefore, in order to keep the operating conditions fixed during the experiment the frequency of the three pumps, the opening of the weir, and the water level were kept fixed during the experiment, ensuring that the conditions would not change. The flow fields are measured using PIV (Particle Image Velocimetry), as explained later.
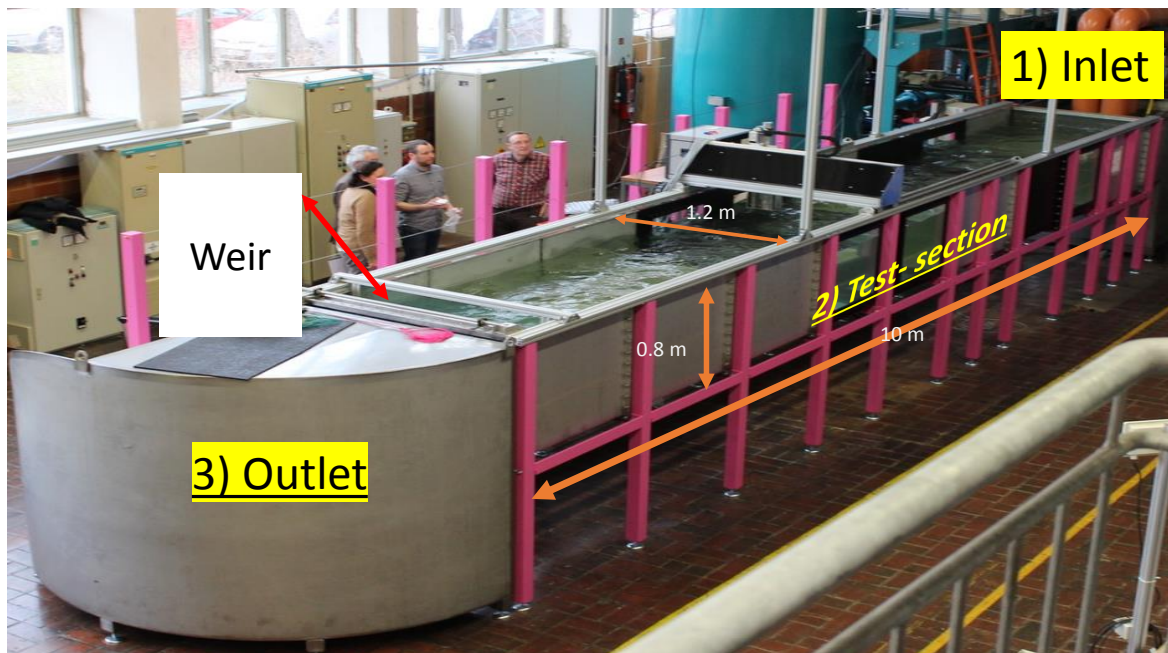
Figure 5.7: The water channel at LSS, OvGU.
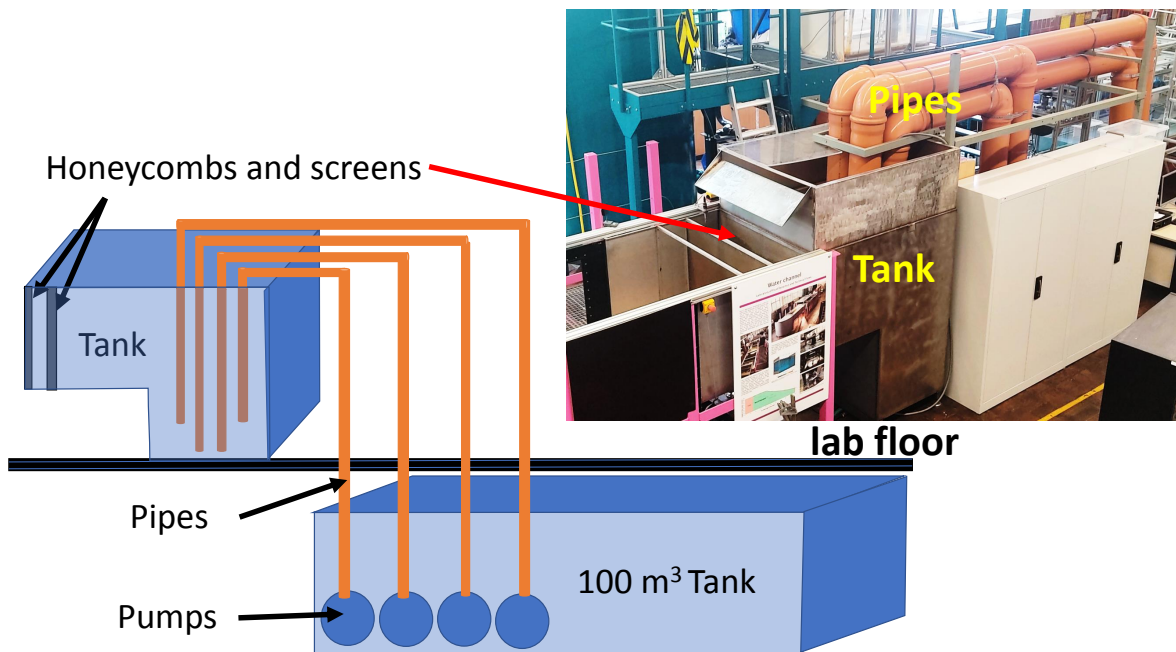
Figure 5.8: A schematic of the inlet zone of the water channel.
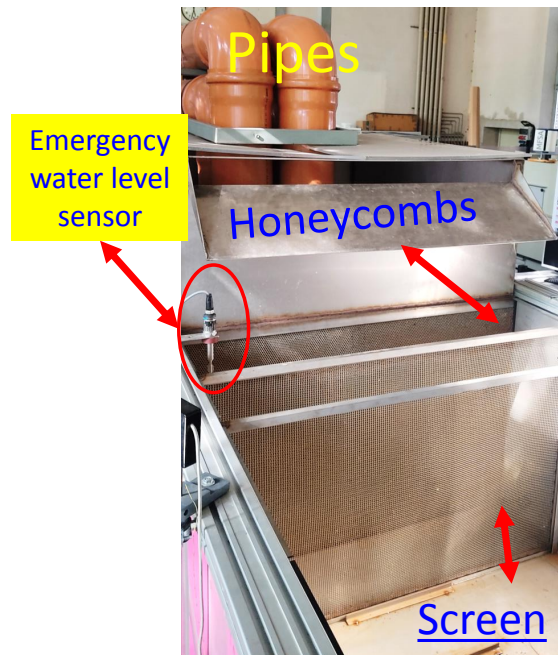
Figure 5.9: Honeycomb and screen at the inlet zone.

5.3.2 Savonius turbine

Figure 5.11 shows the turbine setup with the measurement devices. The hydraulic
Savonius turbine models were produced by cutting a stainles steel pipe into two parts,
then shifting the two parts in the axial direction, producing the two turbine blades.
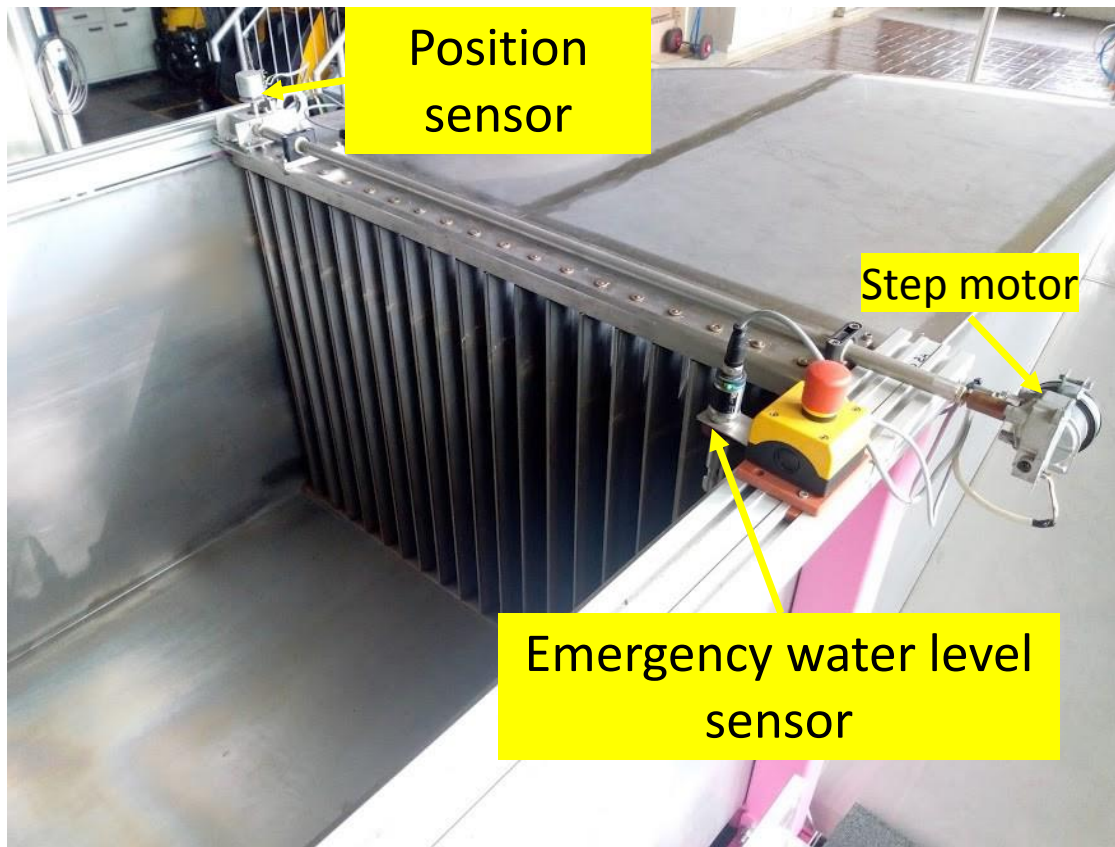
Figure 5.10: The weir system inside the channel.

The gap between the two parts was kept at 20 mm (12% of the diameter) with zero overlap between the two blades. The height of the turbine was kept at 300 mm. The turbine was connected to the top and bottom using two acrylic plates, which were connected with two axes to fix the turbine in place. The torque sensor was connected directly to the axis in order to measure the rotational speed as well as the torque produced. The rotational speed was controlled by an electric motor in order to brake the turbine to different rotational speeds. The setup was fixed on a rectangular frame to be installed inside the water channel, as shown in Figure 5.11.

5.3.3 Torque sensor

The shaft torque and the rotational speed were measured using a Burster sensor model 8661. It has a maximum measurement range of 0 to ± 0.5 Nm (Burster 8661-4500-v0200) and a maximum allowed rotary speed of 25000 rpm. A similar sensor with max ± 2 Nm (Burster 8661-5002-v0200) was used when the power was increased by use of the optimal deflector; this will be illustrated in the next chapter. Figure 5.12 shows the image of the sensor used for measurements. The accuracy of the sensor was 0.05 % F.S. Table 5.3 presents all the technical specifications for both sensors.
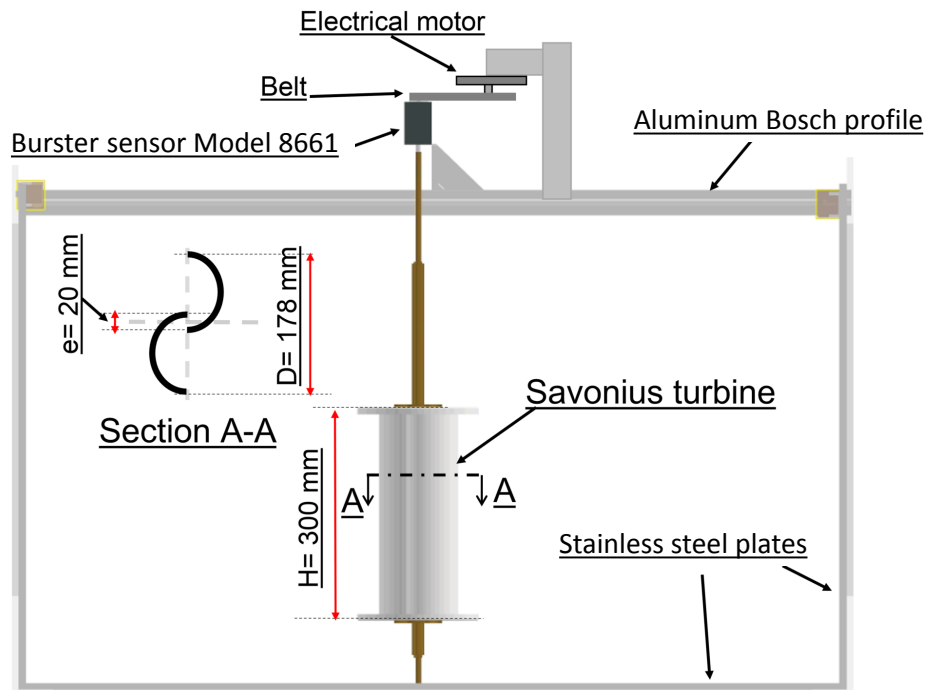
Figure 5.11: Sketch of the standard Savonius turbine setup with torque sensor and electric drive.

Figure 5.12: Burster torque sensor.

5.3.4 Particle Image Velocimetry (PIV) system

The instantaneous flow fields and vortex structures behind the turbine were investigated using particle image velocimetry. It is an optical method that delivers a two- or three-dimensional instantaneous velocity of the fluid flow.

Table 5.3: Technical specifications for the torque and rotational speed sensors

Sensor number	Measuring range	Output voltage	Speed/angle measurement	Accuracy
Burster 8661-4500-v0200	0 to $\pm$ 0.5 Nm	0 to $\pm$ 10 Volt	1024 increments	0.05 % F.S
Burster 8661-5002-v0200	0 to $\pm$ 2 Nm	0 to $\pm$ 10 Volt	1024 increments	0.05 % F.S

5.3.4.1 PIV apparatus

The PIV included: a double-pulsed Nd:YAG laser, optics for PIV, a charged-coupled device (CCD) camera. Davis 8.4 software was used for recording and processing the data. A programmable timing unit (PTU) by LaVision was used to synchronize all the devices. Table 5.4 presents all of the devices' specifications, as follows:

- The lasers used for the experiments were EverGreen series lasers for vertical plane measurements and Quantel's Q-Smart twins which include two 200 mJ Nd-YAG lasers for the horizontal plane measurements. The wavelength of the laser beam was 532 nm.

- An imager LX camera from LaVision was used for the experiments. It is a programmable CCD camera. The camera had a resolution of 3312×2488 pixels. The pixel size was 5.5 μm $\times$ 5.5 μm, and the real pixel size in our setup is 0.127 mm $\times$ 0.127 mm. The PIV velocity vectors were resolved with a window size of 32×32 pixels (as will be explained later in this chapter), an exposure time of 2 μs - 116 ms, and a double shutter with two images; 200 ns is the minimum interframing time. The interframing time was set to 1000 μs. Figure 5.13 shows the double-frame operation time for camera exposure and laser timing. While 2 ms is the time shift between two frames, the recording rate of the images was set by using a photosensor to fix the position of the turbine and change the rate according to the rotational speed of the turbine.

- Sheet optics: The PIV requires a plane of light, or light sheet, which was produced using LaVision light sheet optics. The dimensions of the light sheet were adjusted by refocusing the light sheet thickness and by interchanging different divergent lenses. The light sheet optics were designed for high-power Nd:YAG lasers and could handle beam diameters of up to 12 mm. For this research, a light sheet thickness of about 1 mm was used.
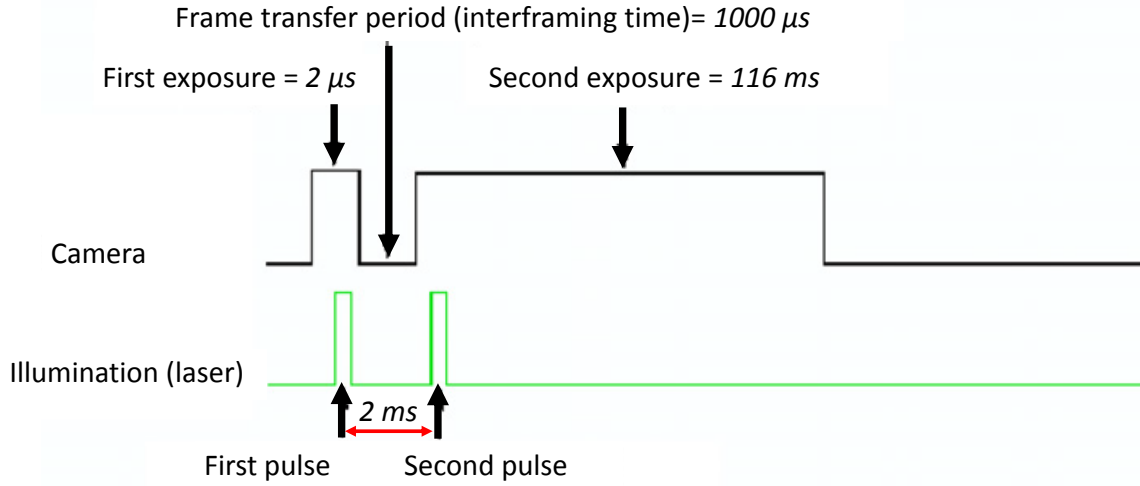
Figure 5.13: Double frame operation for camera exposures and illumination pulses (adapted from [117]).

Table 5.4: Laser and camera specifications

Laser	Type	Evergreen (200) Nd:YAG double pulse
	Output (maximum)	200 mJ/pulse
	Wave length	532 nm
	Pulse duration	$\leq$ 10 ns
Camera	Type	Imager LX 8M
	Number of pixels	3312 x 2488 pixels
	Pixel size	5.5 x 5.5 μm^2
	Frame rate	6.9 frames/s (9.3 frames/s overclocking operation)

5.3.4.2 PIV setup

This subsection contains the PIV setup details. The velocities were investigated by using standard 2-D PIV. A laser sheet of about 1 mm thickness was placed perpendicular to the turbine's direction of rotation and in the middle of the turbine's span, as shown in Figure 5.14. The camera was placed below the bottom of the water channel.

For synchronization of all the equipment, the setup used to record the images consisted of 6 different parts, i.e. the double pulse laser, LX camera, the turbine's position sensor (phototransistor sensor type SG2BC, BCD), PTU, and the computer. All of these were connected to produce two images at a given rotor angle, as shown in Figure 5.15. The data was saved as two images at one angular position of the turbine. This means that there was a trigger sensor fixed over the turbine to produce a 5V signal at a given position. The trigger rate was dependent on the rotational speed of the turbine; the trigger rate increased when increasing the rotational speed of the turbine. For the dual image recording, the time shift was 2ms which is enough time

1: Laser
2: Mirror
3: Laser Sheet Optics
4: Laser Sheet
5: Camera
6 : Turbine
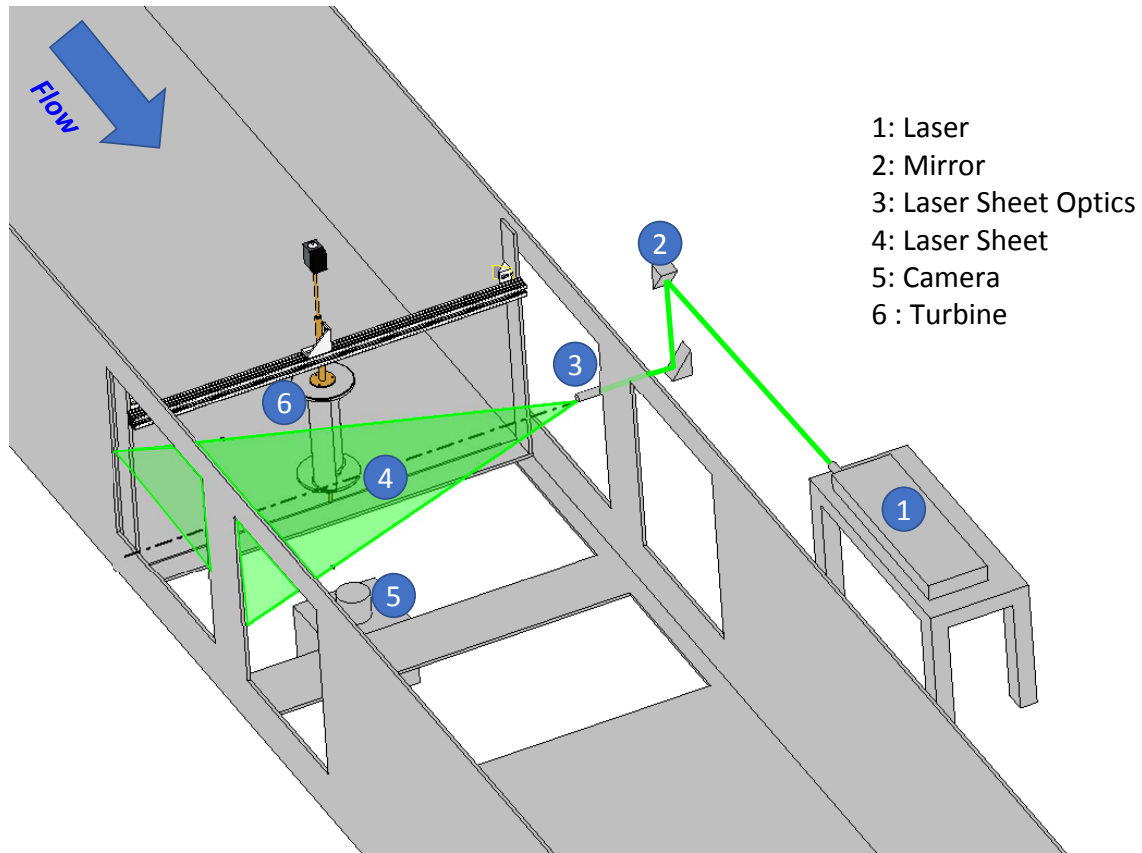
Figure 5.14: PIV setup for measuring the flow structure behind the turbine.

to let the particle move about 4-5 pixels.

A programmable timing unit (PTU) by LaVision was used to synchronize all of the devices. Davis 8.4 software was used to record and process the data, as shown in Figure 5.15. The recording starts when the signal is sent by the trigger sensor and the PTU adjusts two signals, one for the laser and the second for the camera. This leads to a set of double-frame images that can be used to calculate the velocity distribution. The recording was conducted for 500 double-frame images, and the average velocity distribution was computed.

5.3.5 Recording

After all of the connections were made, the first step was to calibrate the camera, i.e. calculating the dimension of each pixel of the camera. A 3D (31×31) type LaVision calibration plate was used to calibrate the camera, as shown in Figure 5.16. The plate contains several white points, with a fixed displacement between each point. The diameter of a point is 3 mm, and the distance between the center of two circles is 15 mm. DaVis software Version 8.4 was used to record fifteen images and take an average
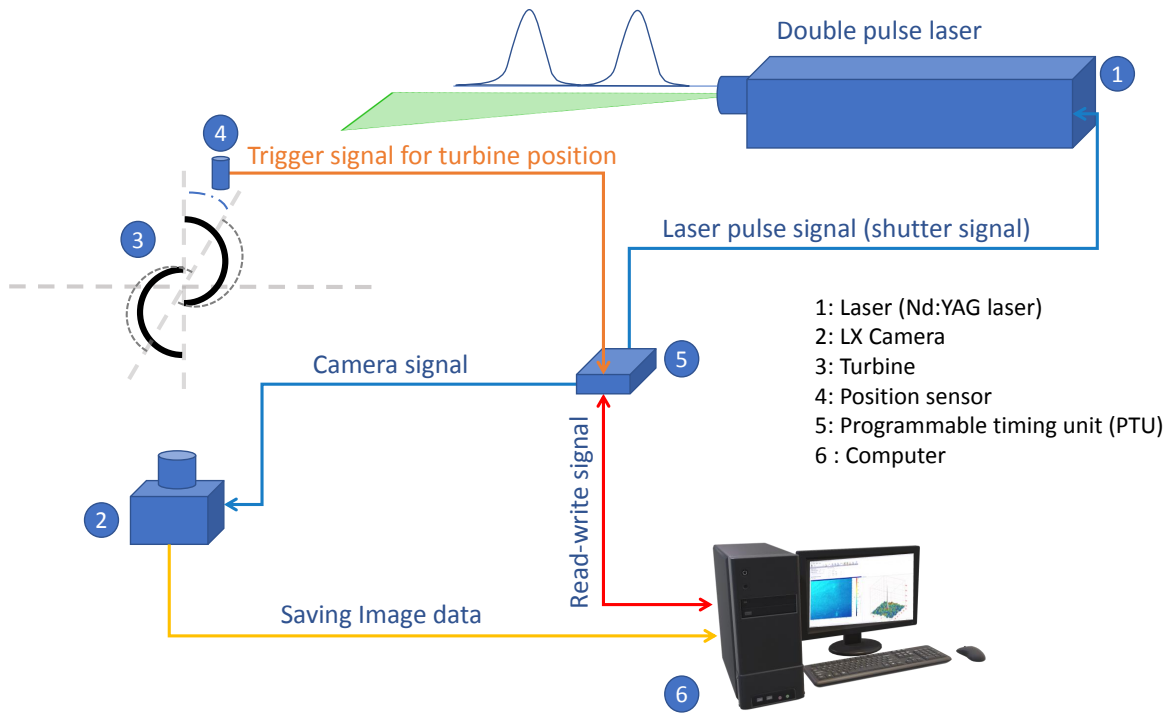
Figure 5.15: PIV connections for saving the images.

in order to increase the accuracy for the calculation of the actual point. Figure 5.16 presents the calibration sheet inside the water channel. By using these images, the camera was calibrated, and the dimension of the pixels was determined. The root-mean-square (RMS) error was determined for the calibration process, which was found to be very small, below 0.09 pixels. This means that only a very small remaining error was due to the calibration of the camera.

After the calibration of the camera was finished and the laser sheet position was adjusted in exactly the same position as the calibration plate, recording of images for different cases started. Generally, two images are enough to calculate the instantaneous vector field around the turbine. However, due to the complexity of this flow, several double-frame images have been acquired for each angular position and used for averaging.

The light sensor was used to set the same phase angle. The procedure was then repeated for different angular position and tip speed ratios (λ), as follows:

- The selected tip speed ratios are 0.6, 0.7, 0.8, 0.9, 1, 1.1, and 1.2.

- Four phase angle were selected, i.e. 0°, 45°, 90°, 135° since the cycle was repeated every 180°.
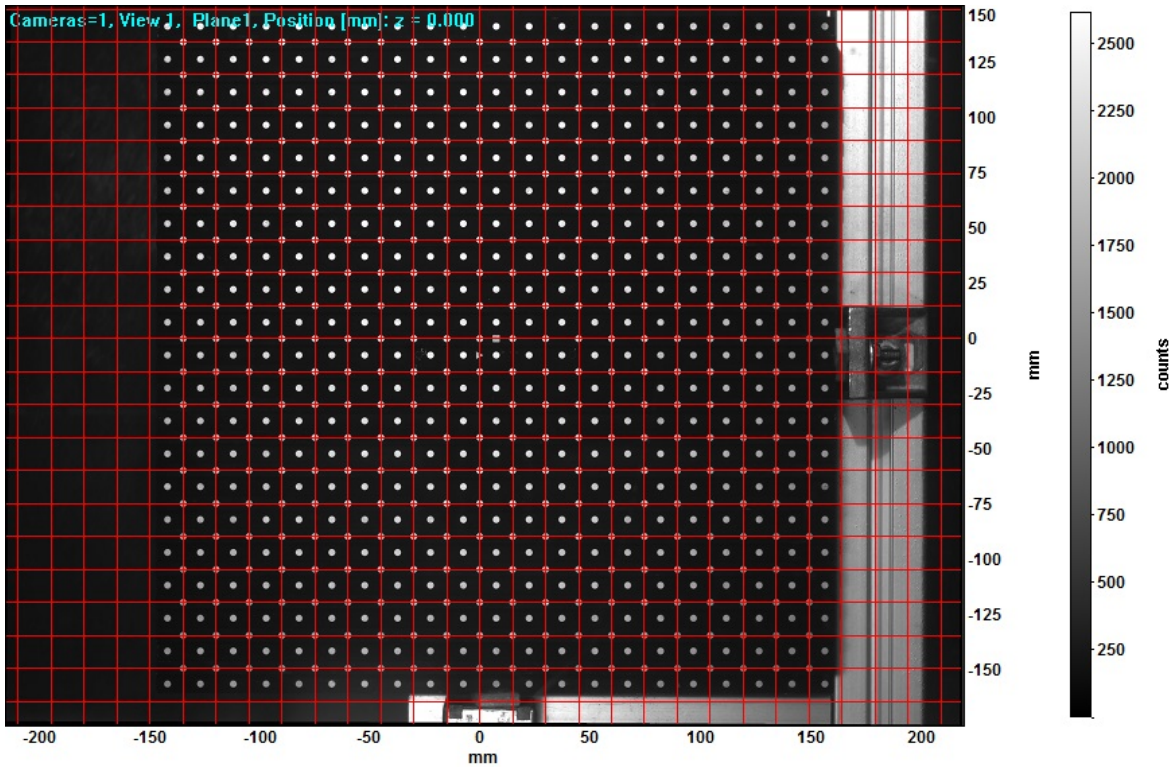
Figure 5.16: PIV image calibrations.

5.3.6 Vector calculation procedures

In PIV, there is no single particle tracking. A general correlation window, which contains from 5 to 6 particles, was used to calculate one velocity vector, as shown in Figure 5.17. Of course, the vector density depends on both of the size of the correlation window and the overlap between windows.
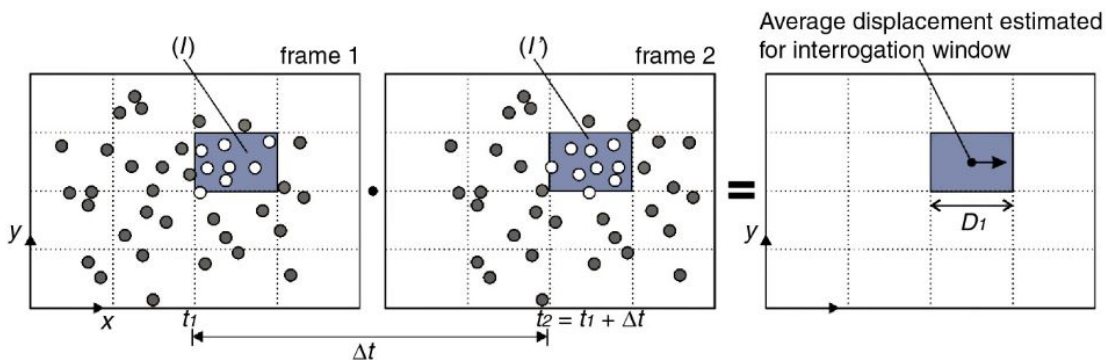
Figure 5.17: Description of correlation window and particle image [118].

To calculate the velocity vectors, the process starts with preprocessing and removing unwanted information such as the sliding background. By removing the fixed

background between the two images, the calculation error will decrease. The sliding background with a max of 5 pixels was set in the Davis program. The images were also smoothed by a 9×9 Gaussian filter.

After preprocessing, the velocity vector calculation was carried out by using cross-correlation with multi-pass, which started with 64×64 pixels and ended with 32×32 pixels with 50% overlap and a single pass. The maximum size of the correlation window and the corresponding correlation factor are presented in Figure 5.18. The maximum correlation factor was 0.9, but in some positions decreased to 0.5. In a post processing step, the results with a correlation smaller than 0.6 were removed. Each vector was calculated 500 times, and at the end, the average value was taken at this particular point.

(a)

(b)
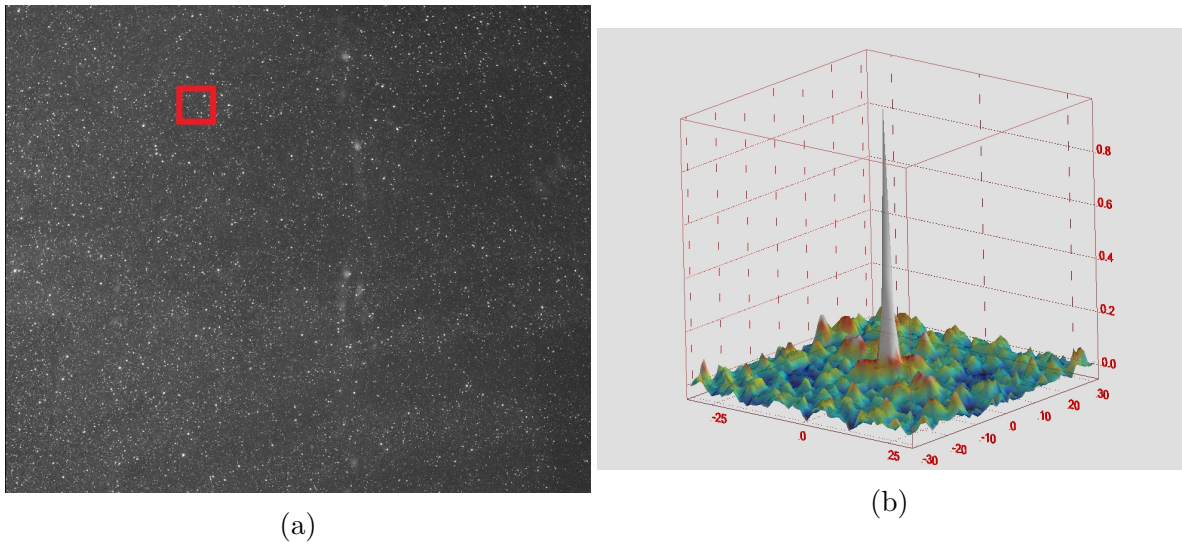
Figure 5.18: Correlation window and corresponding correlation factor: a) A magnified correlation window (64×64 pixels); b) The correlation factor for the corresponding correlation window.

5.3.7 Results and discussion

Here, the results from the experimental measurements will be presented and compared with the 3D simulations. The 3D simulation was built with the same physical models as the 2D simulation used for optimization; only the dimension of the domain was chosen to be exactly identical to the experiment. The first half of this section will deal with the analysis of the power. The second half of this discussion describes the PIV results, and presents a comparison between the velocity distribution of the turbine for simulations and experiments.

5.3.7.1 Error analysis of measured performance

In any accurate experiment, the uncertainty of the measurements should be defined. Usually, the error is defined as the difference between the measured value and the true value. However, this definition is meaningless because, in a real situation, the true value can not be found absolutely. The closest real-world experiments can come to a true value is through calibration, where the measured value is compared to a base value obtained using more accurate devices. Therefore, the error can be more accurately defined as what might be possible given the limitations of measurements as well as the effect of this limitation on the calculated results [119, 120]. The sources of error can be divided into two types: random error, and systematic error. Random error changes from measurement to measurement, while the systematic error is a fixed value consistent between the measurements. Here, the sources of error should be defined for each measured parameter, then the uncertainty of each parameter can be calculated. From these data, the total uncertainty value for the calculated parameters can be defined.

There are several sources of error in these experiments. There is a general source of error, due to changes in room temperature. The experiment was conducted in the lab, where the temperature changed slightly from 20° to 23° between seasons. This temperature change produces uncertainty in the water density of 0.07%. The other source of error is the accuracy of the torque and rotational speed measurement devices. Table 5.5 shows the uncertainty in the measuring devices as well as the other source of error for each measured parameter. The uncertainty in the velocity calculated was extracted from the PIV software, which produced the uncertainty value for each velocity, and the average is presented here. The highest source of error in this setup is the slight misalignment of the turbine axis and the bearing friction. To calculate this error, the turbine was rotated freely for different rotational speeds, without any load on the turbine (without braking forces). The measurement torque in this case is the bearing friction and the very small axial misalignment of the turbine. From these measurements, the friction and axial misalignment errors were calculated at each rotational speed. It was found that the friction increased with increasing rotational speed, thus the absolute value of the friction ranged from 0.004 to 0.008 N.m. That means that the error increased with increasing tip speed ratio.

After calculating the uncertainty in each measured term, the overall uncertainty (ΔC_p) was determined. The overall uncertainty was found according to [119, 121], as shown in Figure 5.19. The steps could be sumarized as follows:

- Calculate the value of C_p according to the measured values, this is the reference

Table 5.5: Source of error for each parameter

Measurement parameter	Source of error	Uncertainty value
Density	Room temperature changes	0.07 %
Torque	Accuracy of the sensor	0.05 % F.S
	Axis misalignment & friction losses	0.004 - 0.008 N
Rotational speed	Resolution of the sensor	0.31°
Velocity	Accuracy of PIV measurements	0.5 %

value.

- Use the uncertainty calculation with the first parameter, e.g. torque and increase the value by the uncertainty in this term and calculate the new value for the power coefficient.

- Find the difference between the new calculated power coefficient and the reference value and store the new value, ΔC_{pi}.

- Repeat the above steps with the other parameters: velocity, rotational speed, and density.

- The overall uncertainty is the root-sum-square of all of ΔC_{pi}.
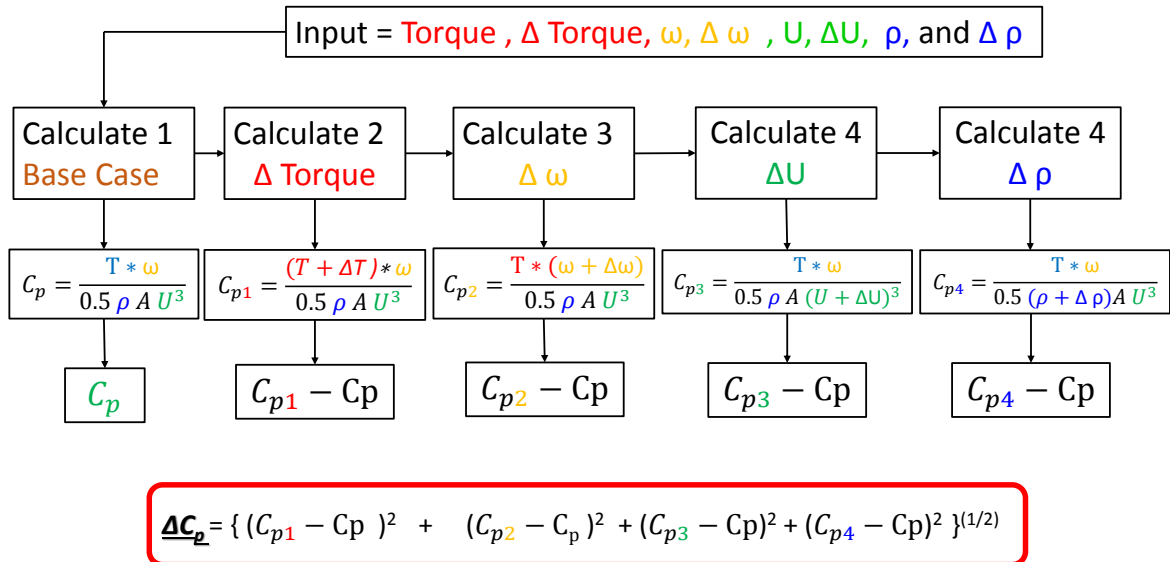
Figure 5.19: The method for uncertainty calculations for the power coefficient C_p.

From the above discussion, the uncertainties of C_p were calculated for all tip speed ratios, and it was found that the uncertainty increased with increasing tip speed ratio,

starting from 2% at $\lambda = 0.6$ and reaching 6% at $\lambda = 1.2$. On the other hand, the error on C_p from the numerical model was estimated to be less than 1 % (see Section 5.2.2). That means that any improvement in performance of less than 6% can not be safely detected by this experimental methodology. However, any improvement higher than 1% can be predicted by the numerical model. In the following discussion, an uncertainty of 6% will be indicated in connection with all experimental results.

5.3.7.2 Performance analysis

Before studying the flow structure of the Savonius turbine, it is important to understand the performance characteristics of this type of turbine. It is essential to determine the performance peaks and cutoff speeds. The values of torque and rotational speed of the model Savonius turbine were recorded using the torque sensor as explained previously. Once the load was applied or varied, time was allowed for the turbine to settle and reach a steady speed, then data samples were recorded for 300 s with a frequency of 500 Hz. Figure 5.20 represents the averaged calculated power coefficient at different values of the tip speed ratio. The figure shows the original measurements and the independently repeated measurements on another day, in order to check the repeatability of the measurements. In the same figure, the values extracted from our 3D simulations are also presented. It is clear that, the performance increases up to a maximum value and then decreases again, as expected. Overall, the performance of the turbine has been obtained experimentally, and the excellent agreement with CFD proves that our simulation can be applied for the optimization process.

5.3.7.3 Flow structure

Now the velocity distribution of the flow behind the turbine will be presented and compared to the extracted velocity field behind the turbine from the 3D simulation. First, the difference between the instantaneous velocity distribution and the average velocity distribution will be discussed. Only one image consisting of two frames is enough to compute the instantaneous velocity distribution in an area. However, in a turbulent flow, it is difficult to compare instantaneous results. Averaging leads to a smoother image and allows removing spurious values and missing values (correlation level too low, as explained previously). Therefore, 500 double frames were recorded by PIV, and the final result was averaged. Figure 5.21a presents an instantaneous velocity field for a particular angular position, and Figure 5.21b is the average velocity at the same position. The average was taken for 150, 250, 300, and 500 images, showing that starting from 300 images the average is constant and does not noticeably change with
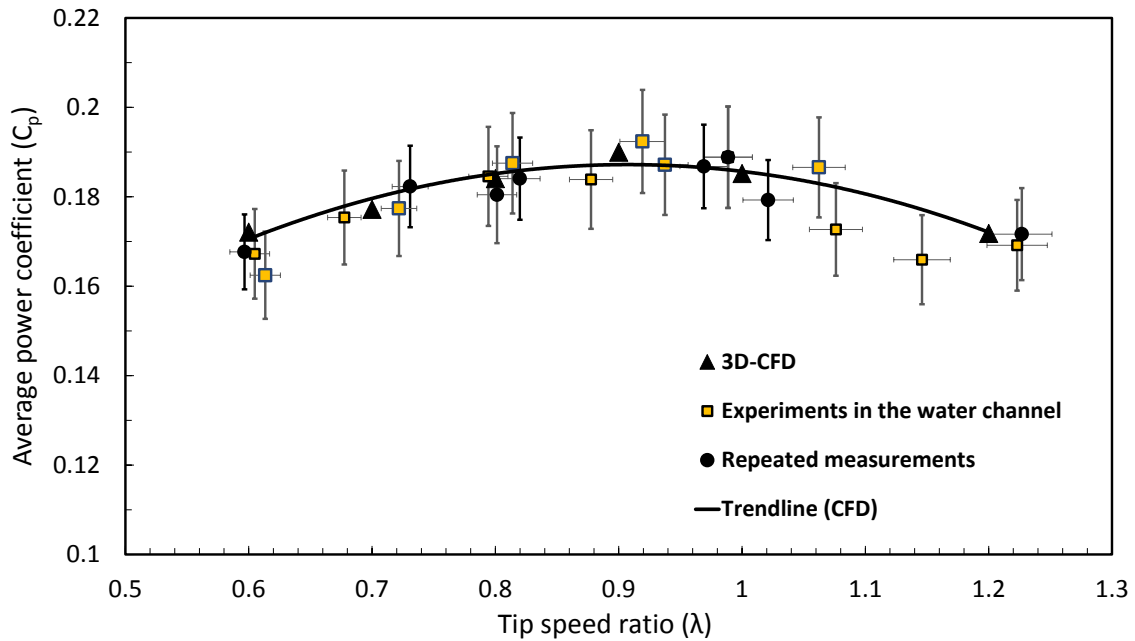
Figure 5.20: Comparison of experimental measurements in the water channel and numerical values of the power coefficient C_p obtained by 3D simulations.

increasing numbers of images. To be in the safer side, 500 images were considered for the following discussion.

(a)   (b)
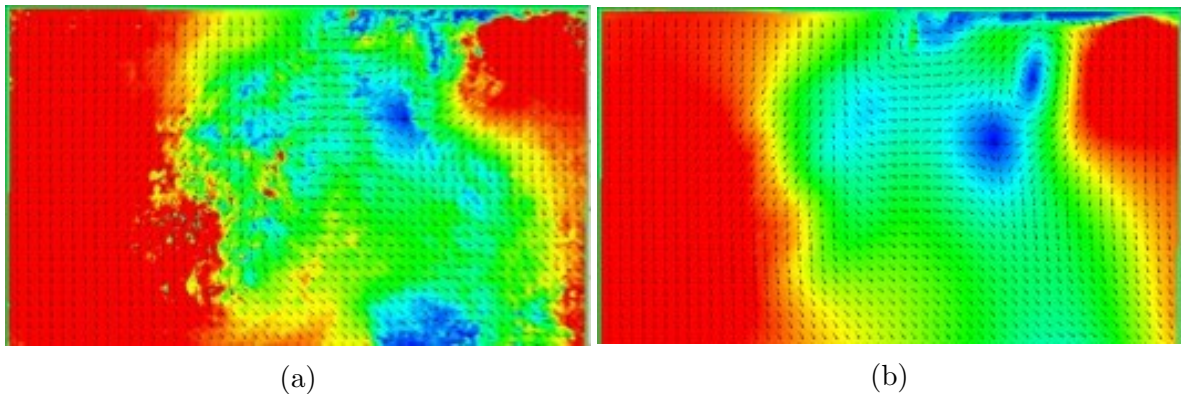
Figure 5.21: Comparison between an exemplary instantaneous velocity field and the average velocity field at the same angular position.

5.3.7.4 Comparison of the 3D simulations with the PIV measurements

Here, the flow structure from 3D simulation as well as PIV measurements will be presented. Figures 5.22 and 5.23 show a comparison of the velocities between the PIV measurement and the 3D simulations for different tip speed ratios as well as various phase angles. To simplify the presentation, all of the figures are shown as one table.

While the columns represent different tip speed ratios, every two rows represent one phase angle, one (top) for the experimental results and the second (bottom) for the simulations.

It is clear that the comparison of velocity distributions at every position for all tip speed ratios is very good. The only visible differences are due to small eddies that differ between simulation and PIV results. The reason for that is that 1) the mesh resolution in the CFD simulations and the resolution of the correlation windows in the experiment at the same position are not identical; 2) a simple RANS model can not perfectly predict such an unsteady, turbulent flow. However, the flow patterns match very well, which means that the setup for the simulation is correct and can be used for optimization.

Figure 5.22: Velocity distribution behind the turbine blades (PIV and 3D simulations).

Figure 5.23: Velocity distribution behind the turbine blades (PIV and 3D simulations).
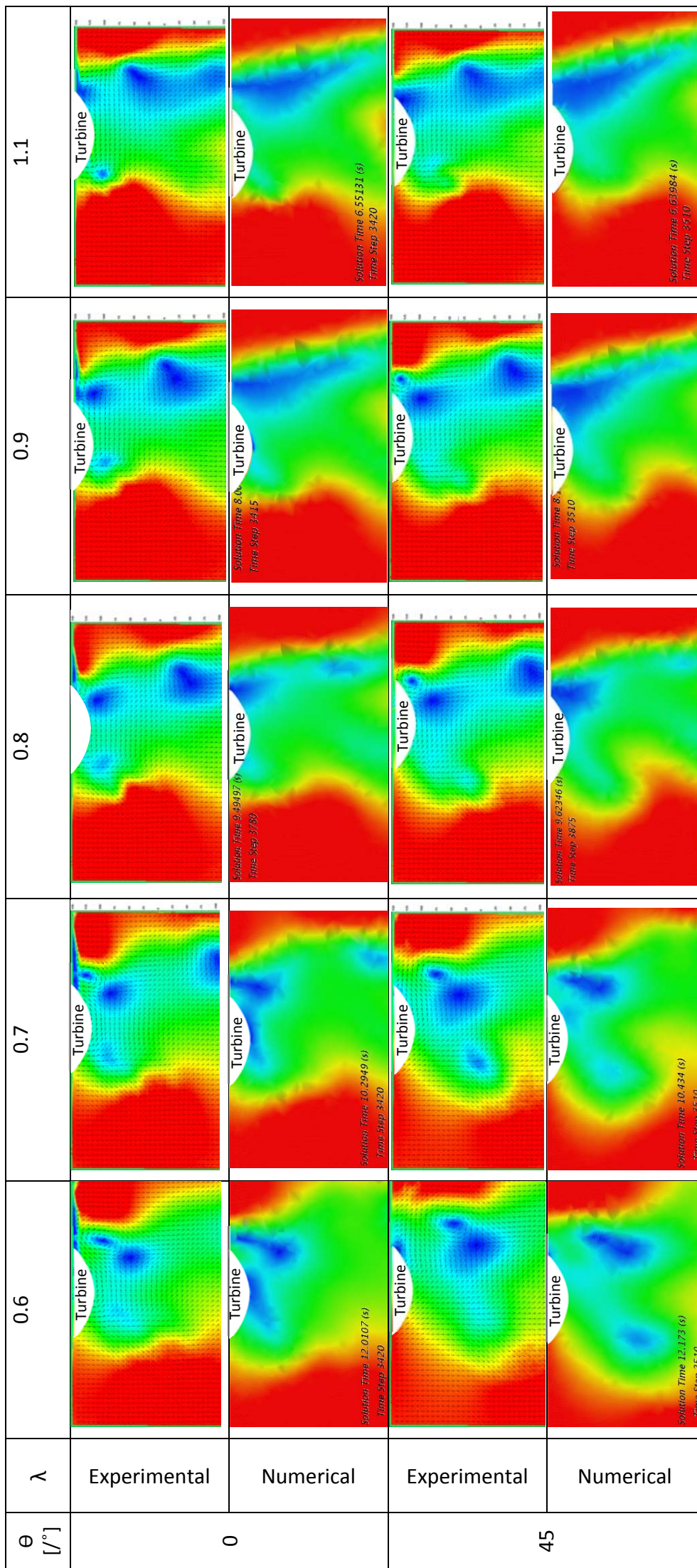
5.4 Optimization process

After completing this successful validation of our numerical model, the optimization process can be started. Since the 3D simulation requires considerable time, 2D simulations will be used for the optimization process, as discussed in Section 5.2. New geometries of the turbine are provided by the optimizer. For each configuration, Star-CCM+ is used to calculate the corresponding value of C_p, as described previously. This value is stored in an output file. By reading this value, the optimizer is able to decide the new geometrical parameters before starting the next iteration, as illustrated in Figure 5.24. This automatic procedure is driven by the OPAL++ tool developed in-house, described extensively in [104]. OPAL++ works on a normal computer, while each simulation case is carried out on a high-speed computer (Neumann cluster). This means that while OPAL++ handles the entire process, each separate run has its own script written for this research. These scripts are: 1) a script to send the data to the cluster, submit the task in the queue system (Slurm), check the completion of this process, then copy the target data to where OPAL++ is running; 2) during the execution of the previous script an other JavaScript is used with StarCCM+ for geometry modification, mesh generation, and simulation execution as well as file extraction for C_p; 3) after both of the above scripts are executed, then commands are sent to verify that the file required for C_p exists and to compute the average value of C_p for the required number of cycles. A similar optimization process has been successfully applied to a variety of flows and turbomachines in our group [122–126]. This process will be applied to all optimization steps described in the following chapter.
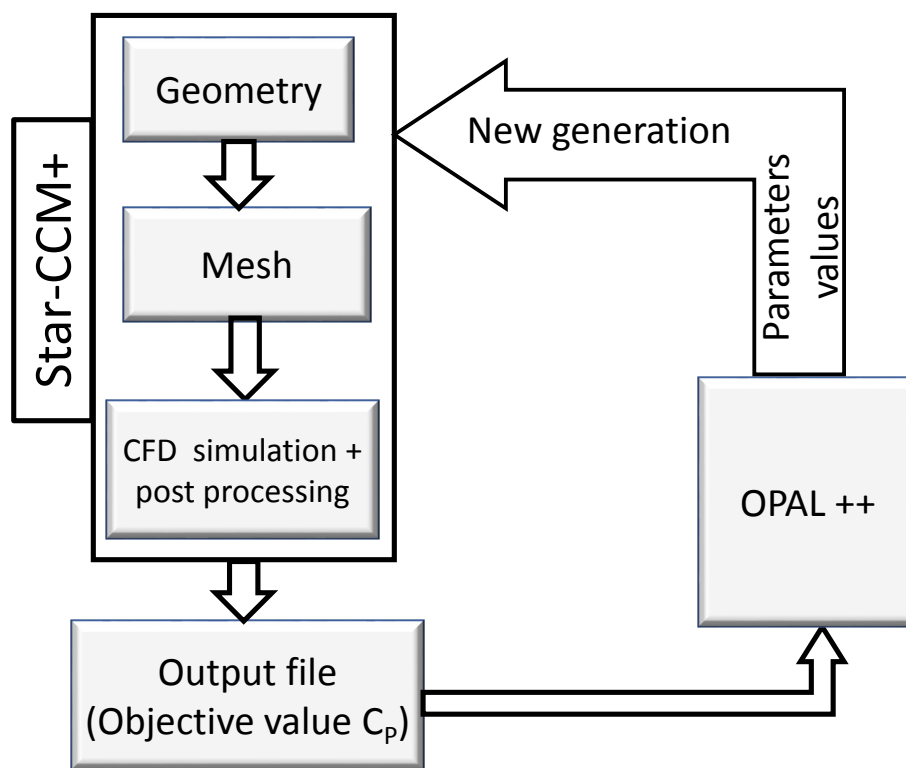
Figure 5.24: Schematic description of the optimization procedure relying on OPAL++.

Chapter 6

Optimization Results

6.1 Introduction

As discussed in chapter 3, Savonius turbines are not new. However, the idea of using Savonius turbines in water (hydraulic Savonius turbines) is quite novel. Therefore, the first part of this chapter will discuss the performance of Savonius turbines in water. Once the main concept of producing power from the Savonius turbine blades is understood, it is possible to use this knowledge to improve the performance of the turbine. The improvements will be based on the optimization of the blades, optimization of a deflector plate, and of the main parameters, i.e., overlap, gap ratio, and arc angle. At the end, all of these parameters will be combined in a very ambitious, single optimization process to obtain a highly optimized hydraulic Savonius turbine. Part of this chapter is based on previous publications [105–107].

6.2 Performance analysis of a Savonius turbine

First, the performance of a standard Savonius turbine will be discussed. At the beginning, the relationship between the power coefficient C_p and the rotational angle will be presented for different tip speed ratios. Then, the highest performance tip speed ratio will be selected, and the positions for maximum and minimum power production will be determined. Since the standard Savonius turbine has two blades, the power produced by each blade will be investigated separately. In the end, the physical behaviour behind the power distributions at different rotational angles will be discussed by analysing the pressure distribution.
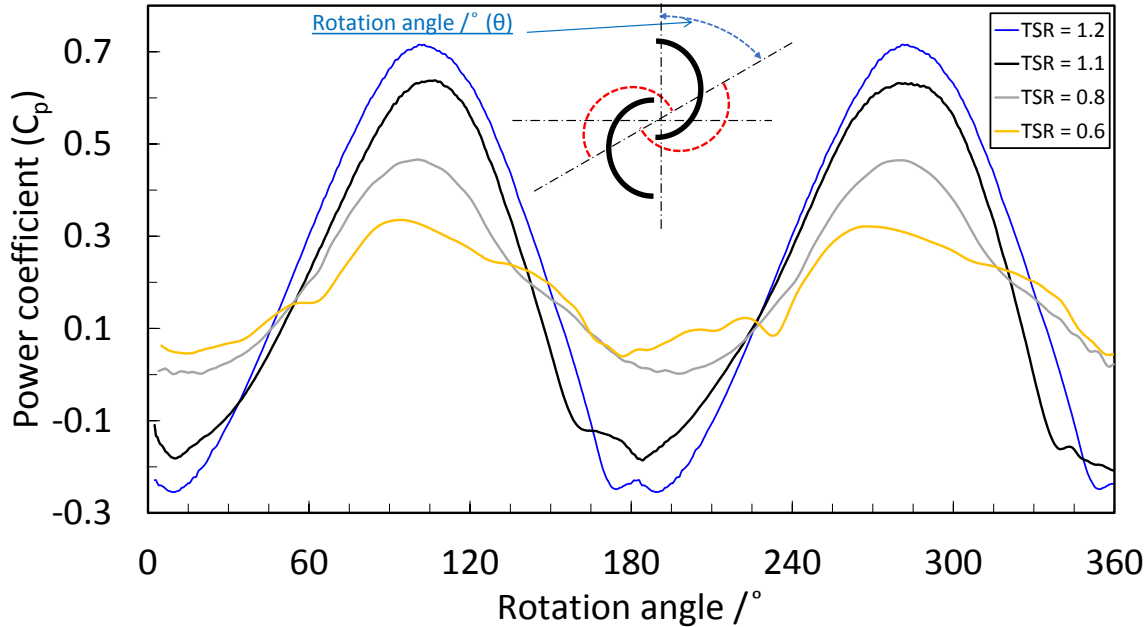
Figure 6.1: Comparison of the instantaneous torque coefficient for different tip speed ratios as a function of the rotational angle for the whole turbine.

6.2.1 Torque and power analysis

Figure 6.1 shows the instantaneous power coefficient for different tip speed ratios as a function of the rotational angle from the 2D simulation. Note that a similar trend is obtained from the 3D simulation, but with different quantitative values. It is clear that the performance is repeated twice during one cycle, as the turbine is symmetric and has two blades. The power coefficient exhibits the same trend for different tip speed ratios. However, the amplitude of C_p increases with increasing tip speed ratio.

By looking at only the black line ($\lambda = 1.1$), it is clear that the performance has two identical cycles, as stated before: the first one from 0° to 180°, and the second from 180° to 360°. For the first cycle, the performance of the turbine increases from the angle 10° to 105° and after reaching the maximum value, C_p starts to decrease to reach the minimum value just after 180°. As the standard Savonius turbine has two blades, the power coefficient presented is the summation of the power produced or absorbed by each blade. The individual power coefficient from each blade is interesting for a better understanding of such turbines.

6.2.2 Power coefficient analysis for each blade

A better understanding is obtained by looking at the instantaneous C_p values, and considering the two blades separately. Figure 6.2 shows the instantaneous C_p for each

blade separately as well as the summation for the two blades. While the red dotted line presents the instantaneous C_p for blade 1, the C_p for blade 2 is shown by the dotted blue line. The solid black line shows the summation of both blades at each rotational angle. It can be seen that blade 1 produces peak power in the range between 240° and 360°, while the peak energy is generated in the range from 60° to 180° by blade 2. Accordingly, the power curve of the whole rotor shows two corresponding peaks. In the following, blade 1 will be considered individually in order to better understand the performance.
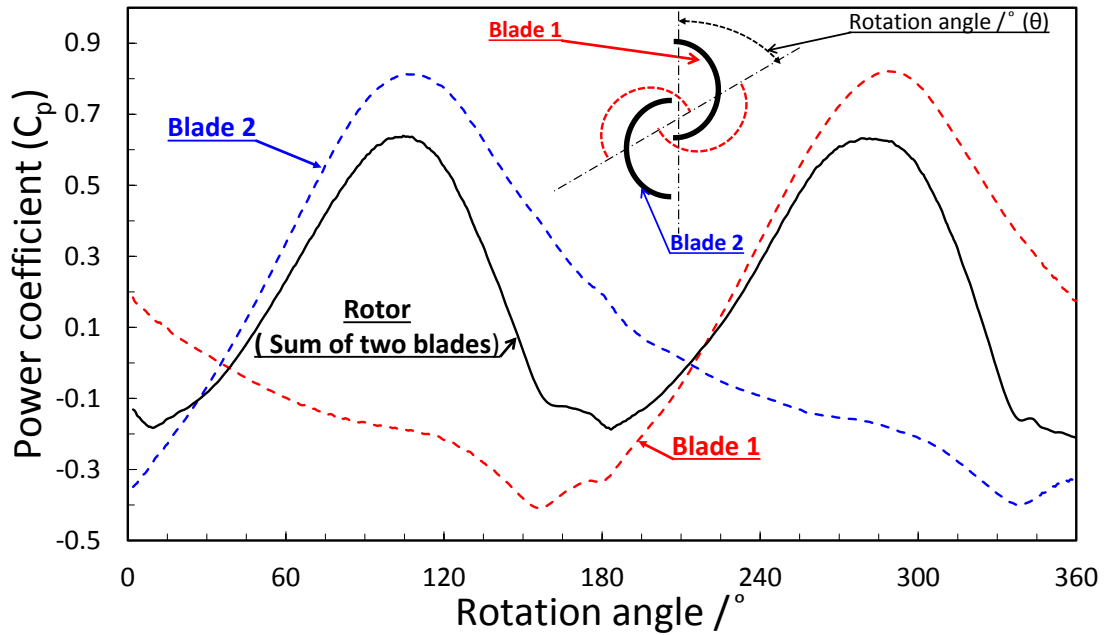
Figure 6.2: The power coefficient C_p for different rotational angles for each blade at $\lambda = 1.1$.

6.2.3 Pressure distributions

In Figure 6.3, the average C_p for blade 1 is shown together with the instantaneous pressure distributions obtained from a sample cycle (the last one) for different angular positions of the rotor between 0° and 315° discretized in steps of 45°. By focusing in particular on the pressure field along the back side of blade 1, the change in power coefficient can be best explained. From angle 0° to 180°, the pressure over the back side of blade 1 increases noticeably with the rotation angle, resulting in a reduction in blade power. Contrarily, for the range from 180° to 360°, not only the pressure over the back side of the blade decreases, but also the pressure on the front side increases. Due to the resulting pressure difference, a high positive power coefficient is produced by blade 1 in this range.
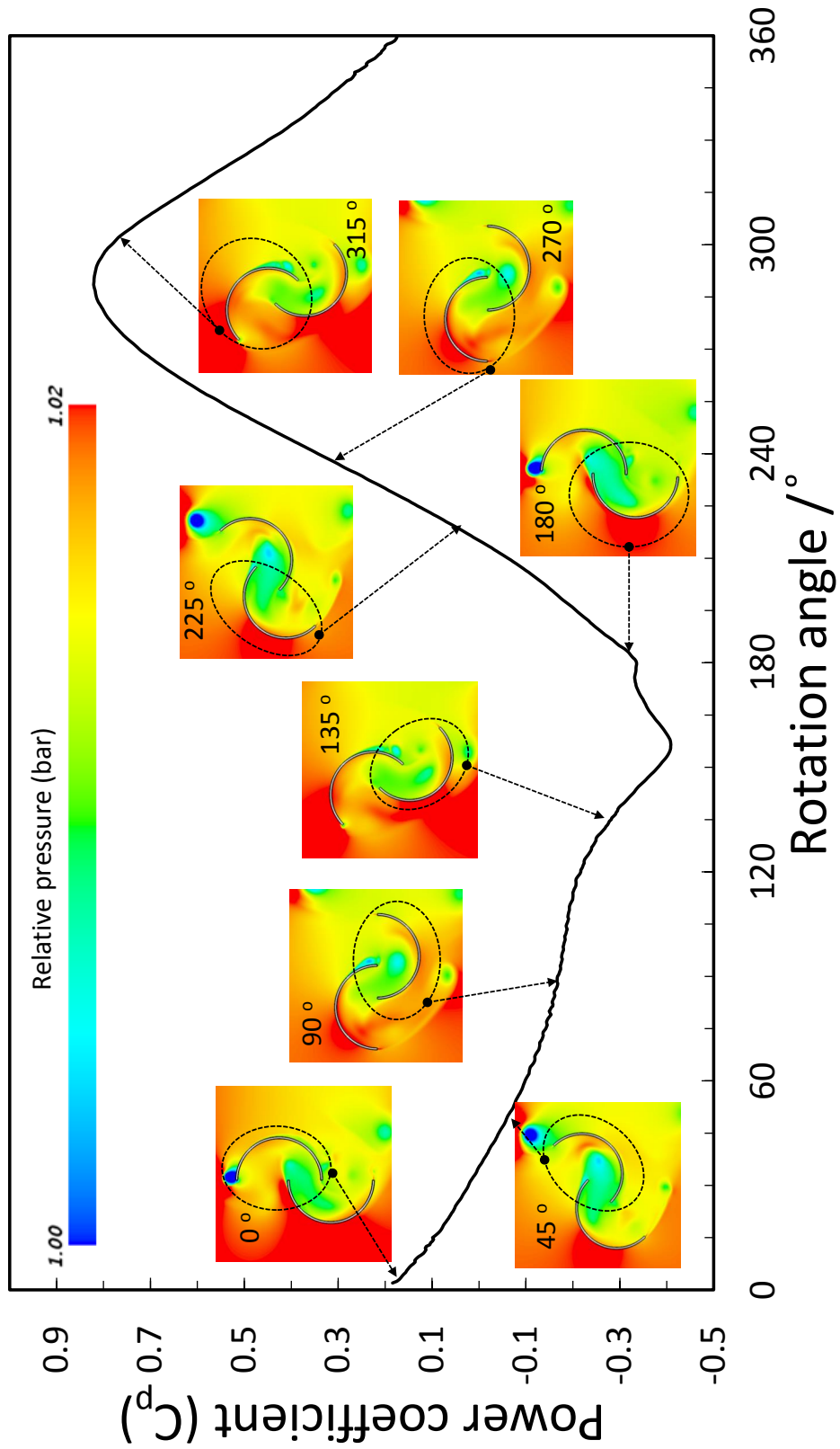
Figure 6.3: Instantaneous pressure distributions for different angular positions of the rotor overlaid on the average power coefficient C_p for blade 1 at $\lambda = 1.1$.

6.3   Optimization

It is clear that the performance of such turbines is mainly dependent on the pressure distribution around the blade, around the concave side as well as at the convex side. Therefore, the performance of such turbines will be greatly improved by increasing the pressure on the concave side, decreasing the pressure on the convex side, or both. To change the pressure distribution, several techniques will be used. First, the two sides of the turbine blade are optimized separately, as shown in Figure 6.4 part one. Second, a deflector plate is added in front of the turbine, as shown in Figure 6.4 part two. Third, the main parameters of the turbine such as gap ratio, overlap, and arc angle are optimized together, as shown in Figure 6.4 part three. Fourth, the optimal plate will be kept while optimizing the thick blades, and vice versa optimizing the thick plate using the optimal blade in order to determine the effect of both on the performance. Finally, the thick blades and the thick plate will be optimized together to determine the maximum improvement.

As a basis for the numerical optimization, all of the dimensions and operating conditions of a standard Savonius turbine were selected based on the experiments conducted in [115], which were already used in the previous chapter for validation. The only modification is that the central shaft was removed, because 1) the shaft impacts – usually negatively – turbine performance [41], 2) it is not needed, since structural rigidity and torque transmission can take place through the end plates, 3) and most importantly, the shaft would constrain the changes in blade geometry tested during optimization, since wall collisions obviously must be avoided. The optimization process was carried out for a single value of tip speed ratio, $\lambda = 1.1$, since it delivers the peak power coefficient for the standard design according to the literature (see also the previous chapter). The optimization process itself will be finally validated with the turbine that was also used to validate the 3D model in the previous chapter: the optimal deflector will be installed in the channel and changes in the performance will be measured.

6.4   Optimization of the thick blade

Now, the first part of the optimization process (optimization of the thick blade) will be discussed. The blade will be divided into two separate parts, the concave side and the convex side. The shapes are optimized, separately.
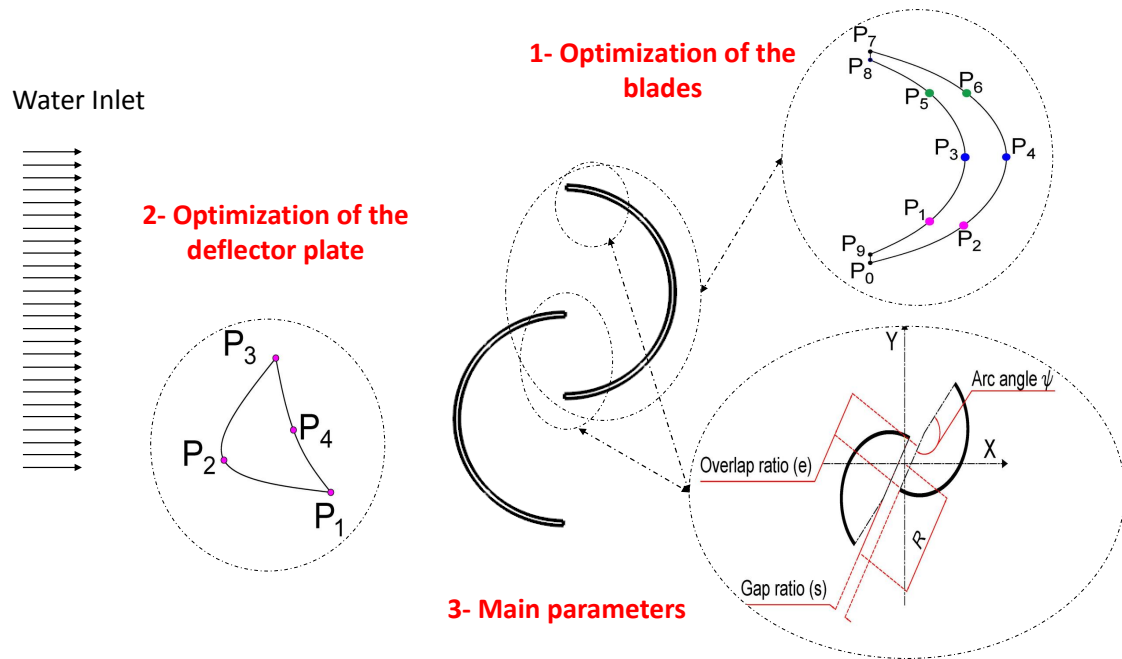
Figure 6.4: Optimization parameters.

6.4.1   Parametrization and optimization procedure

The modified Savonius turbine blade was formed by changing the shape of the concave and the convex sides independently. The two blades are always identical in order to avoid torque imbalance. Each blade side was created by connecting five points with a NURBS-spline, as exemplified in Figure 6.5; in this process, four points (P_0, P_7, P_8, P_9) are kept fixed in order to maintain the diameter of the turbine and to preserve a central open space, while the three inner points are allowed to move freely within a given range, their position being simply specified by two variables (X_i and Y_i for point number i). Therefore, each blade side is finally defined by five points (two fixed, three moving), in other words, six geometrical variables (the X and Y coordinates of the three moving points). The convex side is uniquely determined by X_2, Y_2, X_4, Y_4, X_6, and Y_6, while the concave side is prescribed knowing X_1, Y_1, X_3, Y_3, X_5, and Y_5.

During optimization, it must be ensured that the blade retains a minimum thickness in order to have sufficient rigidity. In the work presented here, this minimum thickness was set at 2 mm. Additionally, collisions between the opposite sides of the two rotor blades must be avoided. Finally, any overlap of points in the Y direction must be avoided; a minimum distance is needed to keep acceptably smooth shapes. At the end, the domains retained for all geometrical parameters are shown in Table 6.1 and Fig. 6.5, where r is the radius of the standard, semi-cylindrical blade.

Table 6.1: Acceptable ranges for the input parameters

	Minimum allowed	Maximum allowed
X_1/r	0.1	1.0
X_2/r	0.1	1.0
X_3/r	0.1	1.5
X_4/r	0.1	1.5
X_5/r	0.1	1.0
X_6/r	0.1	1.0
Y_1/r	0.1	0.67
Y_2/r	0.1	0.67
Y_3/r	0.67	1.32
Y_4/r	0.67	1.32
Y_5/r	1.32	1.92
Y_6/r	1.32	1.92
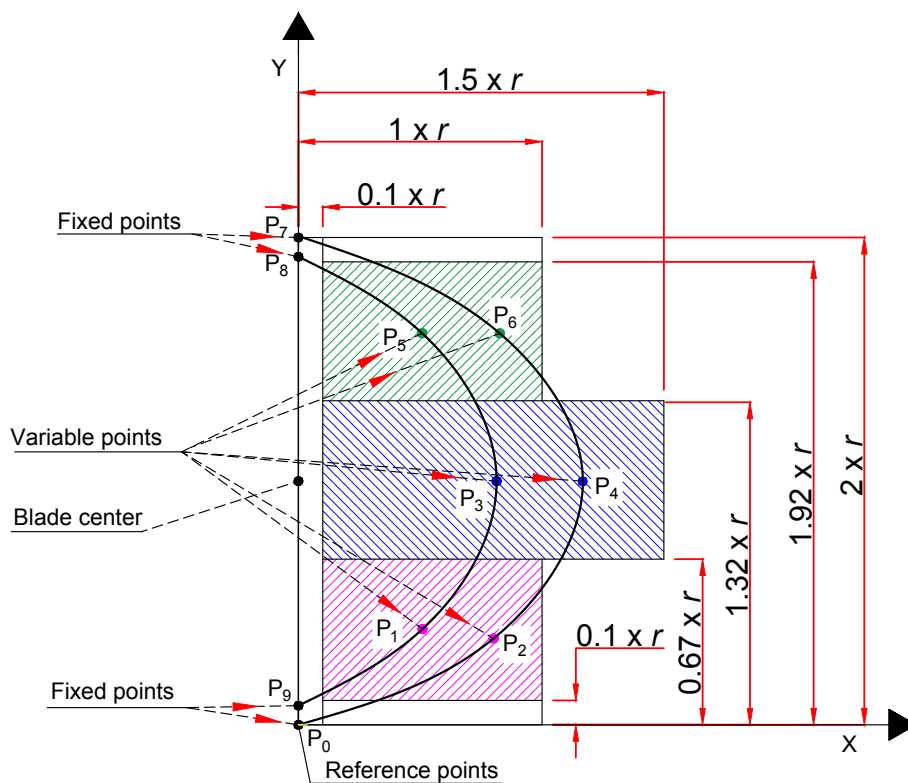
Figure 6.5: Geometrical description of the blade's shape.

6.4.2 Results and discussions

6.4.2.1 Optimal configuration

Figure 6.6 represents the results of the optimization in the form of parallel coordinates, connecting the twelve input parameters (the geometrical positions of the moving points) in the twelve columns on the left, to the objective function C_p on the right. Overall, 636 different blade shapes have been tested, each of them with its own CFD computation. Each of these configurations correspond to a thin line in Figure 6.6. The optimal configuration is shown by a thick black line. It should be noted that this line does not reach the minimum or maximum values prescribed in Table 6.1, meaning that the parameter space is large enough to contain the optimal solution. In the right column, it is clearly seen that the performance of a standard Savonius turbine can be greatly improved by changing the shape of the concave and convex sides of the blades. At $\lambda = 1.1$, the power coefficient is increased by 0.03 (absolute), or 12% in relative terms. Table 6.2 contains the coordinates of the moving points leading to the optimal power coefficient.
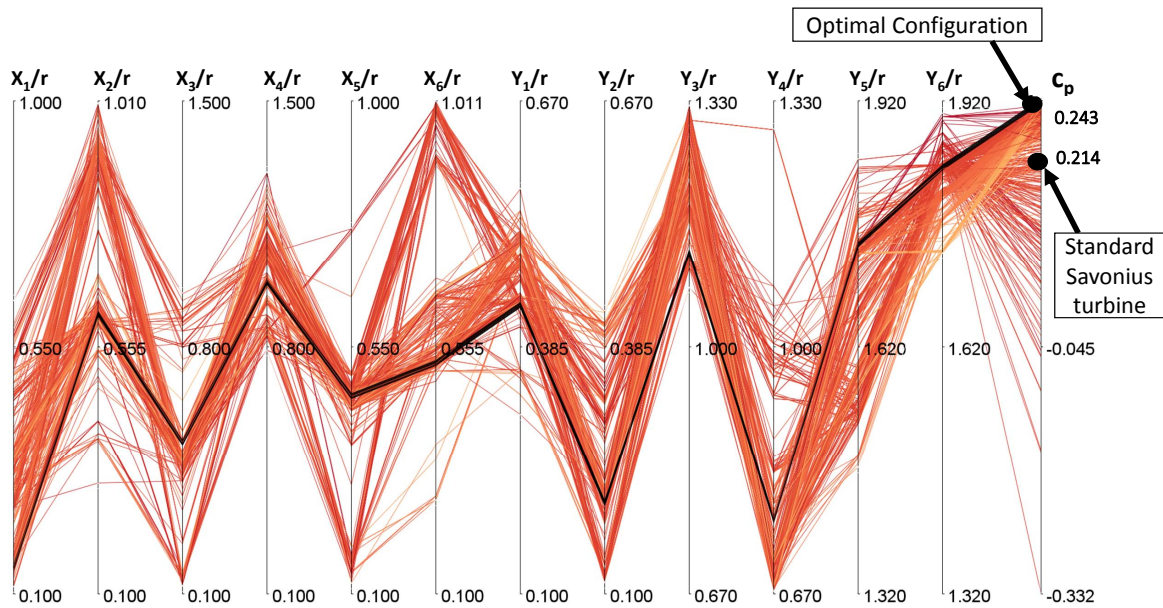
Figure 6.6: Parallel coordinates showing the input parameters of the optimization on the left side (each on its own scale between the bottom and top boundaries) and the target value (power coefficient C_p) on the right side.

6.4.2.2 Comparison of geometries

The optimal and the standard blade shapes are compared in Figure 6.7. For the concave sides, the optimal blade is flatter along the blade length, except at the outer

Table 6.2: Optimal parameter values

	X/r	Y/r
P_1	0.148368	0.434196
P_2	0.618185	0.204772
P_3	0.529482	1.128993
P_4	0.987394	0.769296
P_5	0.461322	1.747061
P_6	0.526977	1.839818

part, which is bent far more strongly than the standard Savonius turbine, leading to a hooked shape. On the other hand, on the convex sides, only small changes are observed, and the two turbines have nearly the same half-circular profile.
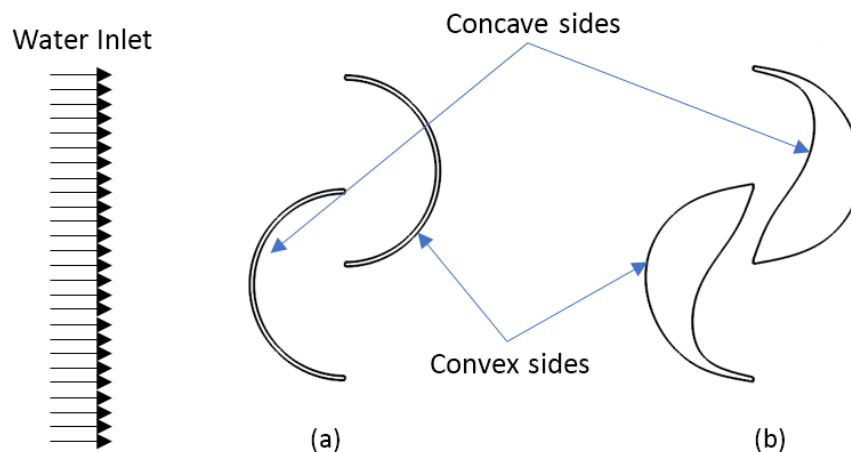
Figure 6.7: Comparison of the shapes of (a) a standard Savonius turbine (b) an optimally shaped Savonius.

6.4.3 Power analysis

The C_p values have been further compared during the last rotation at $\lambda = 1.1$. Figure 6.8 shows the instantaneous C_p as a function of the rotational angle, both for the conventional and the optimal blade shapes for the whole rotor and a single blade, respectively. It can be seen that the instantaneous C_p is greatly improved in the angular range between 0° and 90°, as shown in Figure 6.8a. A better comparison can be made by using the instantaneous C_p values for a single blade because the rotor power output is a result of the combination of the power of two blades. As shown

in Figure 6.8b, the instantaneous value C_p is greatly increased in the angular range between 170° and 280°, while the value of C_p is slightly decreased in the range of 300° to 20°. Variations in the instantaneous C_p values can be explained by comparing the pressure distribution around a single blade. Figure 6.9 shows the pressure distribution for two different rotational angles (180°, and 360°). An angle of 180° lies within the improved range, while an angle of 360° is found in the reduced range. It can be seen that the pressure around the optimal blades is overall lower compared to the standard shape. For a more quantitative explanation, the pressure distribution along the blades will be presented as a function of the projected location on the Y axis, y/R, where y is the projected position and R is the radius of the turbine. Figure 6.10 shows the pressure distribution for angles of 180° and 360°, respectively. At an angle of 180°, the pressure distribution on the concave side of the optimal blade slightly decreases compared to the standard one. However, the pressure on the convex side is significantly reduced. As has been noted, the net pressure decreased and the net-produced power improved in the regions of 170° to 280°. At 360°, the pressure along the convex side of the optimal blades also decreases somewhat. However, the pressure on the concave surface of the standard shape is still high compared to the optimal shape. Therefore, the power produced is slightly worse compared to the standard shape in the region of 300° to 20°. Concerning the velocity field, a video describing its evolution during the last rotation cycle is available as a supplemental material Video(2).
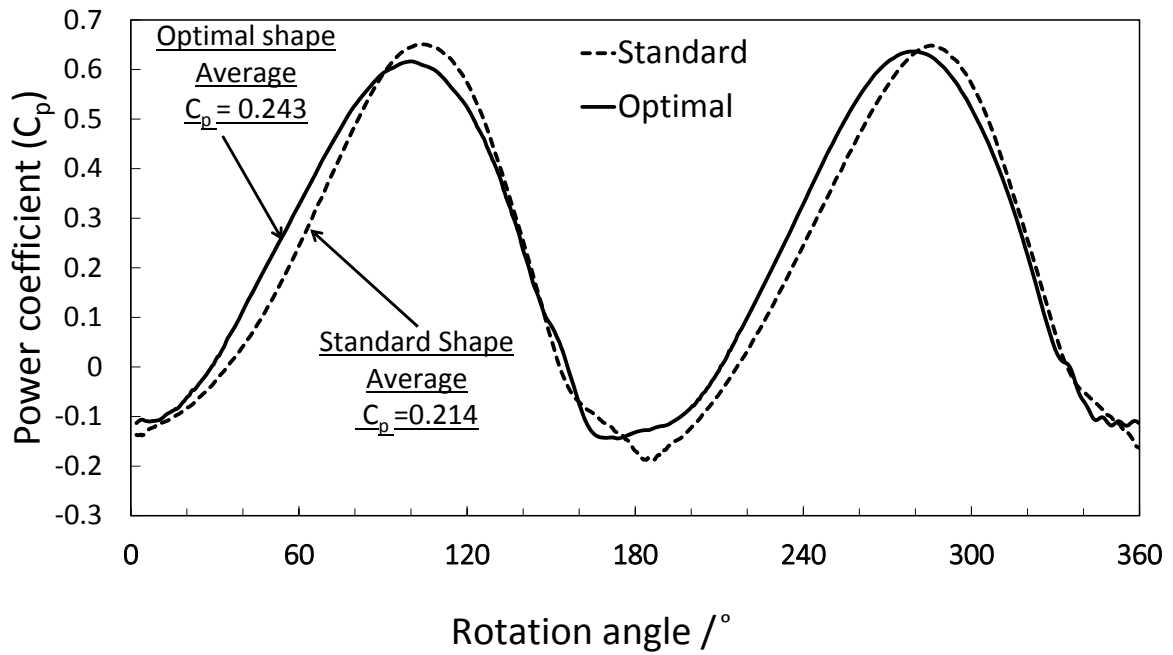
(a) Instantaneous C_p of the rotor
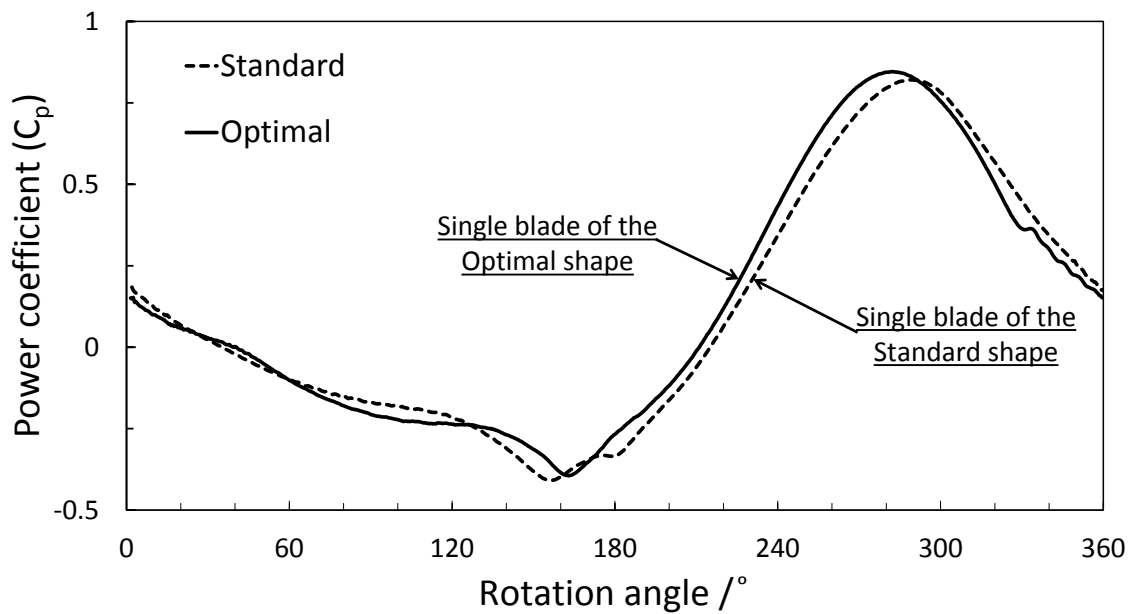
(b) Instantaneous C_p of a single blade

Figure 6.8: Comparison of the instantaneous C_p at $\lambda = 1.1$ (a) for the rotor (b) for a single blade.
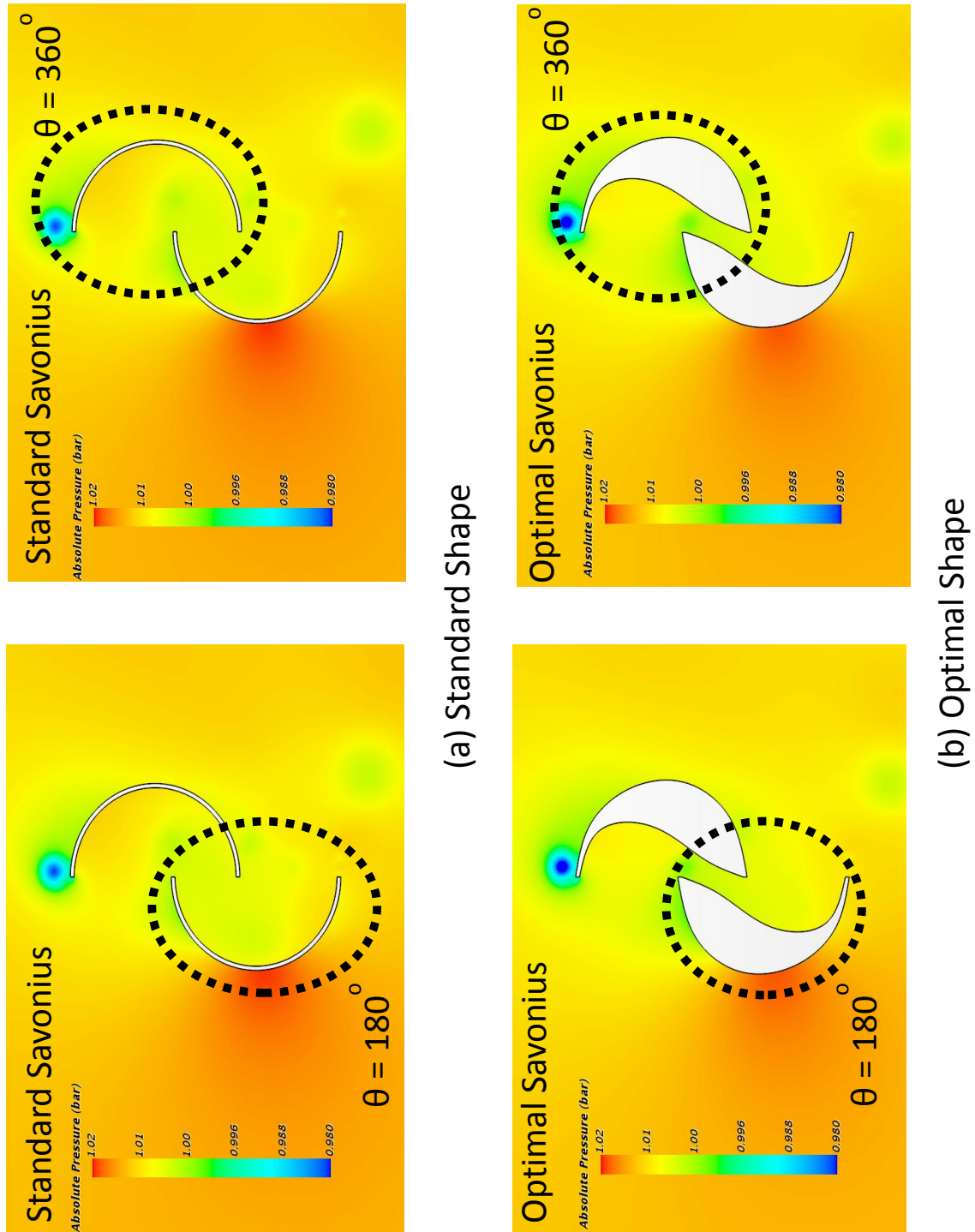
Figure 6.9: Comparison of the pressure distribution around the blades for (a) the standard shape (b) the optimal shape at rotational angles of 180° and 360°.
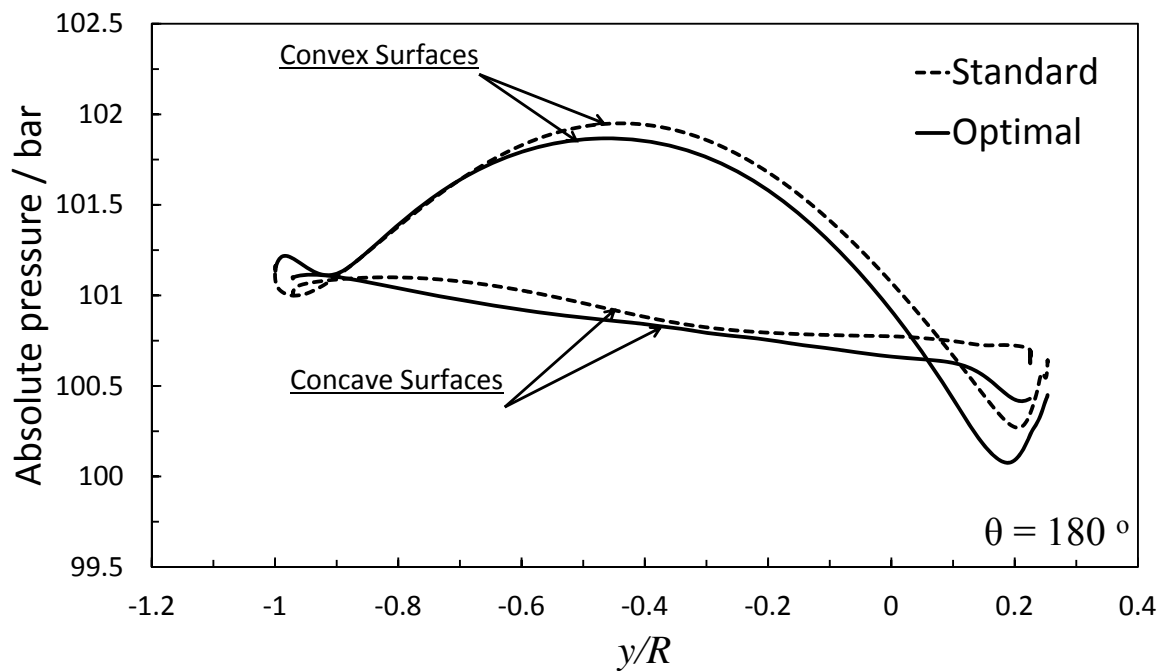
(a) 180°
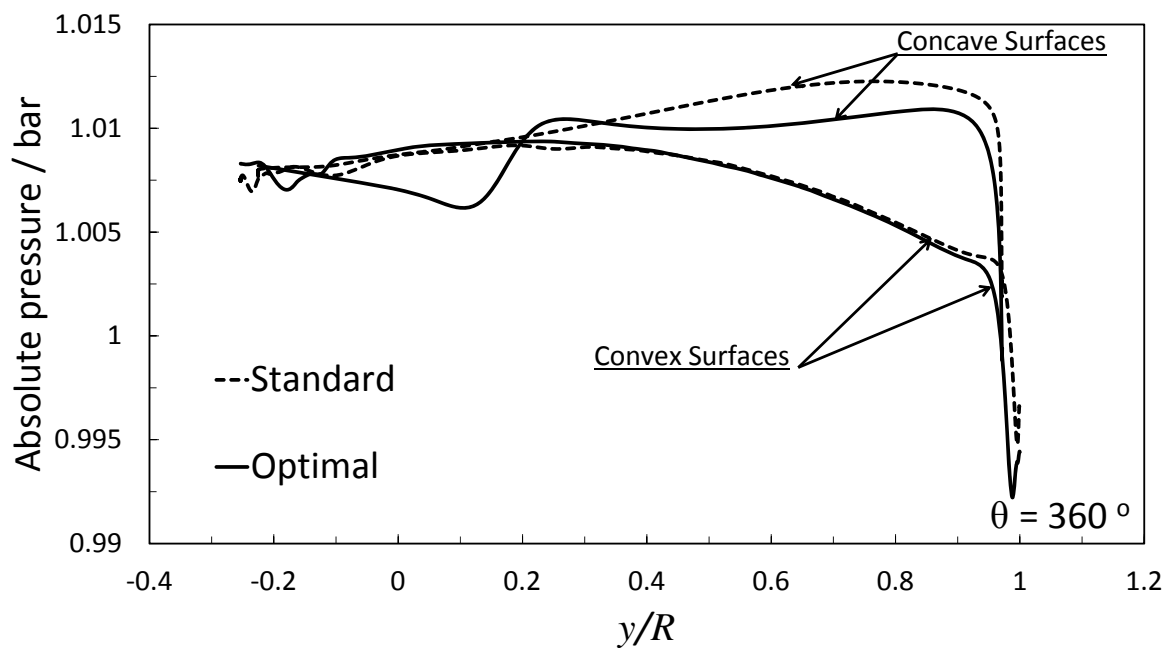
(b) 360°

Figure 6.10: Comparison of the pressure distribution around the blades at rotational angles of (a) 180° (b) 360°.

6.4.4 Complete operating range

Finally, the performance of the optimal and of the standard turbines have been simulated for the full relevant operating range, $0.6 \leq \lambda \leq 1.2$, as shown in Figure 6.11. The

average torque coefficient C_t decreases for both the standard and optimal turbines for increasing λ, which is expected from results reported in the literature [38, 60, 63], but this decrease is noticeably less pronounced with the optimal blade shape.

While the performances of the standard and optimal designs are quite similar for $\lambda < 0.8$, the optimal blade shape always leads to improved performance, and the gain becomes particularly strong with increasing tip speed ratio, by 12% at $\lambda = 1.1$ and almost 15% at $\lambda = 1.2$.
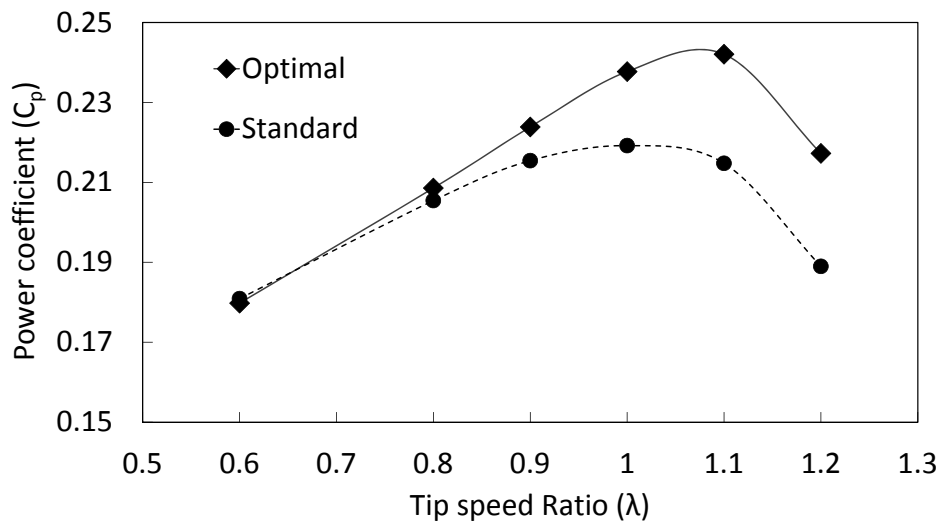
(a) Power coefficient
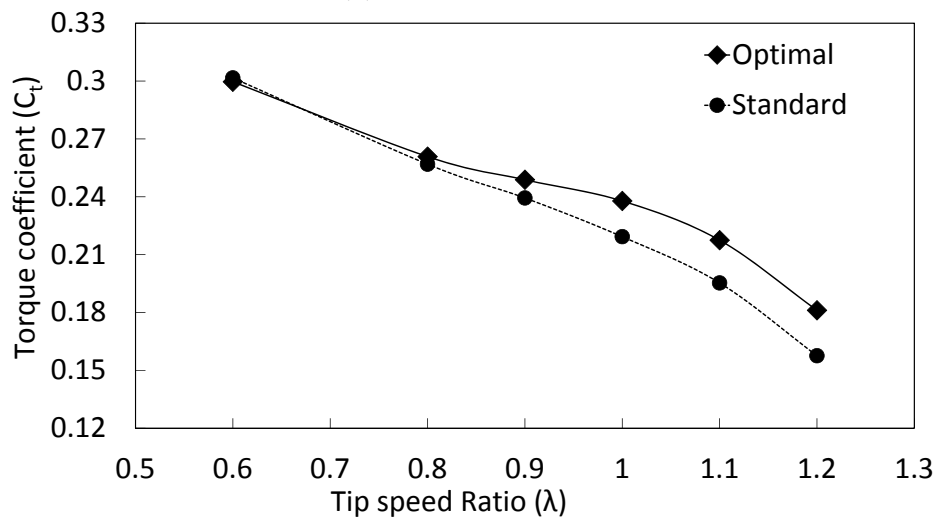
(b) Torque coefficient

Figure 6.11: Comparison of (a) the average power coefficient C_p and (b) the average torque coefficient C_t as function of the tip speed ratio for standard (dashed line) and optimal (solid line) Savonius turbines.

6.4.5 Self-starting performance

Finally, in order to check the ability of the improved system to self-start, the static torque was computed for both turbines at different fixed angles. Figure 6.12 shows the variation of the static torque coefficient for both the standard and the optimal shape as a function of θ. Due to periodicity, the results are only plotted for angles between 0° and 180°. It can be seen that, both standard and optimal shapes show a similar curve concerning static torque characteristics. The standard shape has a somewhat higher static torque coefficient for θ in the ranges from 0° to 50° and from 120° to 180°, while the optimal design shows slightly higher values for θ between 60° and 75°. What is most important is that, both shapes have self-starting ability ($C_{ts} > 0$) at all angles. It is well known that the standard Savonius design is self-starting; this property is conserved for the optimal shape.
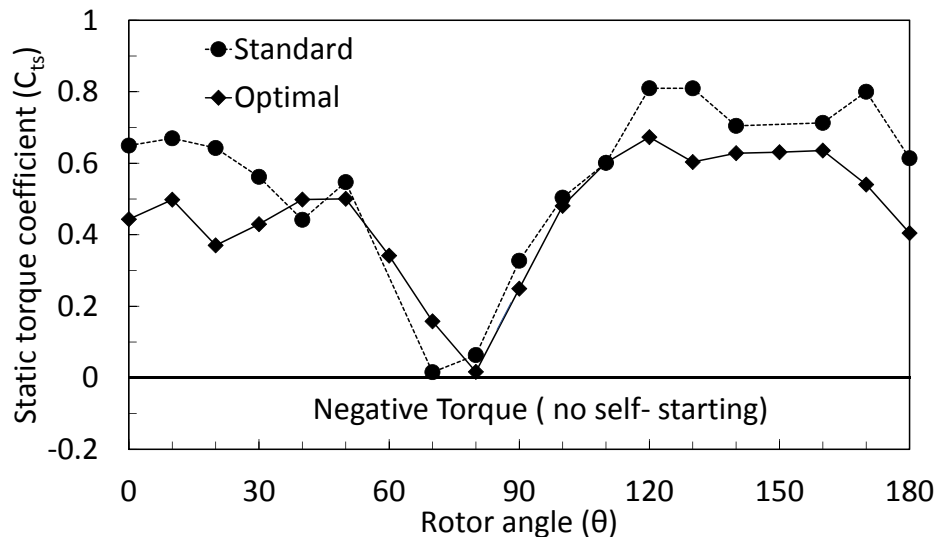
Figure 6.12: Static torque coefficient C_{ts} as a function of the fixed rotor angle θ for optimal and standard shapes.

6.5 Optimization of thick plate

In a second step the use of a deflector (or guiding) plate at the front of the turbine will be discussed. The deflector will be added first to the classical Savonius turbine in order to investigate the effect of the deflector without the effect of the thick blades.

6.5.1 Parametrization and optimization procedure

The focus of the following sections is on the deflector plate's position and geometry. The optimization process takes into consideration the constraint that the frontal area

of the system should not be larger than that of the turbine alone, which allows direct and fair comparisons between the obtained power outcome. As stated before, the optimization is carried out for a fixed value of the tip speed ratio, $\lambda = 1.1$, since this value is known from the literature to deliver the peak power coefficient for the standard design.

For the optimization process, the shape and the position of the deflector plate are simultaneously optimized. The plate's upstream and downstream sides are described by two separate NURBS splines; each spline is created by connecting three points, as explained in Figure 6.13, with P_1 and P_3 being the endpoints of both sides. To allow numerous configurations of the deflector plate, these points must be allowed to move freely in the specific domain. Each point is described by two coordinates, X_i and Y_i for point number i. However, point P_1 is allowed to move only in the X direction, keeping a fixed value of Y_1 equal to the radius of the turbine, ensuring that the frontal area of the system (deflector plate + turbine) is the same as for the original turbine. Finally, the geometry of the deflector plate is uniquely defined by four points and seven geometrical variables (X_1, X_2, X_3, X_4, Y_2, Y_3, and Y_4). Additional geometrical constraints given by Eq. 6.1 are taken into account to ensure that all of the resulting shapes could be produced in reality. The minimum thickness of the plate was set to 2 mm in order to give the deflector plate sufficient rigidity, which protects the returning blade against floating objects. Table 6.3 and Fig. 6.13 present the ranges maintained for all entry parameters, where R denotes the radius of the turbine. These values ensure a sufficient gap between deflector and turbine.

Table 6.3: Acceptable domain for the entry parameters

	Upper limit	Lower limit
X_1/R	-0.63	-2.25
X_2/R	-0.9	-2.25
X_3/R	-0.9	-2.25
X_4/R	-0.9	-2.25
Y_2/R	0	-0.99
Y_3/R	0	-0.99
Y_4/R	0	-0.99

$$\text{Constraints} \begin{cases} \mid Y_2 \mid > \mid Y_3 \mid \\ \mid Y_4 \mid > \mid Y_3 \mid \\ \mid X_2 \mid +0.002 > \mid X_4 \mid \\ (X_i)^2 + (Y_i)^2 > (1.2R)^2 \quad \text{for all points} \end{cases} \tag{6.1}$$

In the optimization process, Star-CCM+ simulated the flow around the turbine and then calculated the average value of C_p for each configuration, as illustrated earlier. However, the average was taken here for the last 15 cycles since using a deflector produces larger fluctuations in the performance from one cycle to another. Then, the average C_p value was saved in an output file, which was read by the optimizer to determine the new geometrical variables used to initiate the next generation, as shown in Fig. 6.14. This automatic process was controlled by the OPAL++ tool, which was explained in the previous chapter.
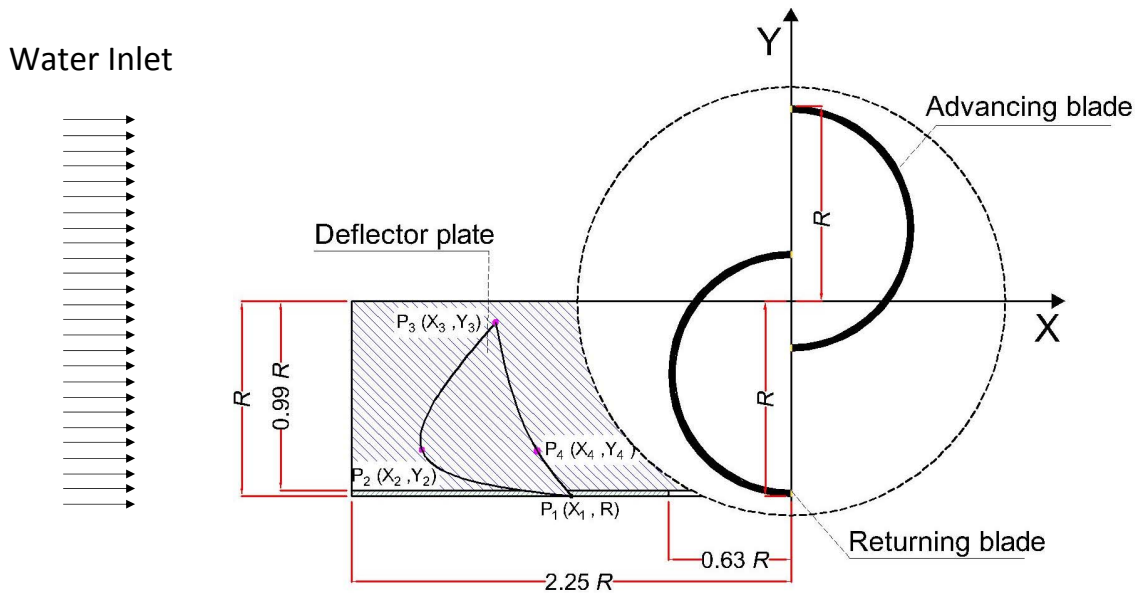
Figure 6.13: Geometrical description of the deflector plate in the optimization.

6.5.2 Results and discussion

6.5.2.1 Optimization process output

Figure 6.15 shows the parallel coordinates for the optimization process outputs, coupling the seven columns on the left, describing the positions of the seven input pa-
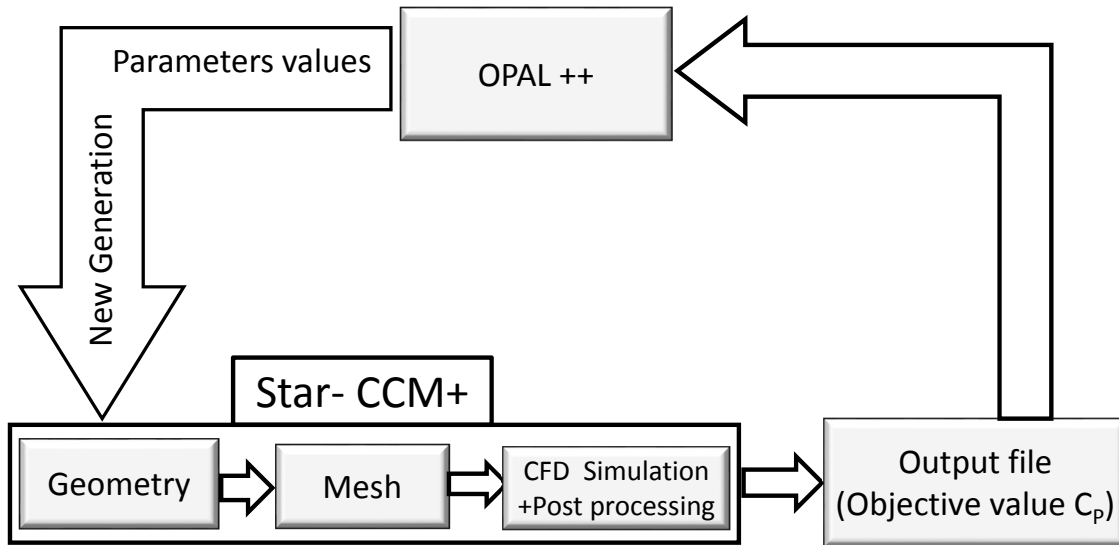
Figure 6.14: Graphical description of the optimization process.

rameters, with the C_p (target objective) on the end right; 463 configurations were simulated. Each configuration is shown by a thin line in Figure 6.15, while the optimal configuration is presented by a thick black line. The optimal configuration is close to the lower limit for Y_4, indicating that the optimizer tries to increase the frontal area of the deflector plate beyond that of the turbine, which is not allowed in this reaserch in order to ensure a fair comparison between all configurations. For the other design variables, it can be observed that the thick black line lies well within the applied range prescribed in Table 6.3, which means that all of the other optimal parameters are far from their respective boundaries. By focusing on the power coefficient column on the right, it is obvious that the power coefficient of a standard Savonius turbine can be greatly improved by adding an optimized deflector plate. The efficiency of the turbine is increased by 0.025 at the maximum tip speed ratio, which indicates a relative increase of 11.6%. Table 6.4 lists the coordinates leading to the maximum average power coefficient.

Table 6.4: Optimal values for the entry parameters

	X/R	Y/R
P_1	-1.490	-1 (Fixed)
P_2	-1.734	-0.48
P_3	-1.58	-0.317
P_4	-1.165	-0.98
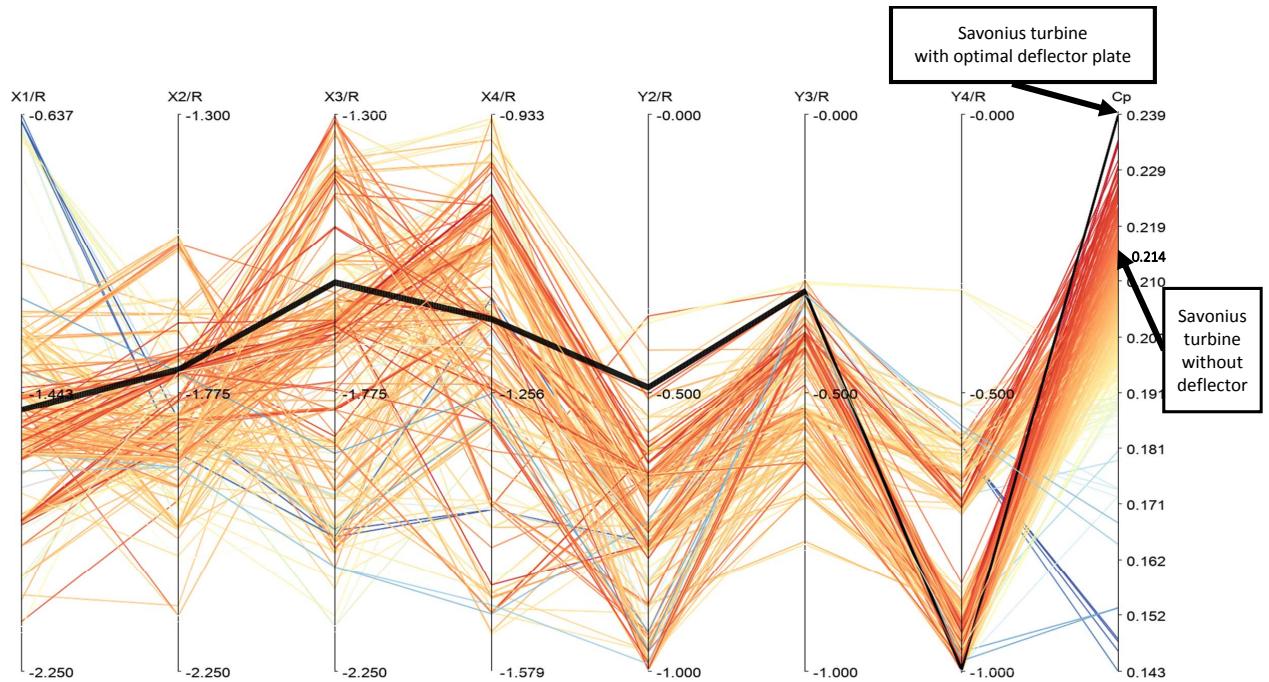
Figure 6.15: Parallel coordinates for the optimization output; the 7 columns on the left side indicate the entry parameters, and the right column presents the objective value.

6.5.2.2 Optimal deflector plate

The optimal position and configuration of the deflector plate are now discussed in detail, as shown in Figure 6.16. When it is in the optimal position, the deflector plate covers roughly only the outer half of the returning blade in the Y direction. Extending the deflector further towards the rotational center of the turbine might be advantageous in protecting the blade, but it obviously leads to a degradation of performance and has, therefore, not been favoured by the optimizer. Furthermore, the deflector plate is located relatively far away from the turbine at about $1.4R$. This is apparently preferable for the performance and will additionally reduce cyclic load variations induced by the interaction between the deflector plate and the turbine, reducing fatigue on the system. The shape of the deflector plate can be simply described by its sides, side 1 (upstream) and side 2 (downstream). Side 1, facing the water stream, shows a clearly curved profile re-directing the flow toward the advancing blade while side 2, facing the turbine and depicted with a thick blue line, is almost straight.
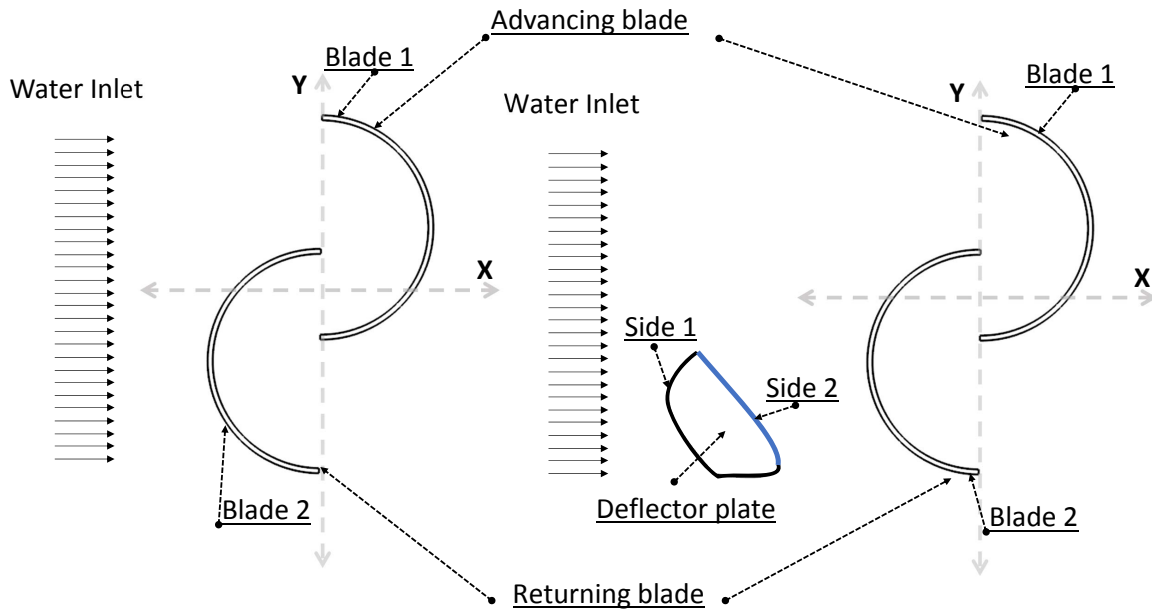
Figure 6.16: The optimum configuration obtained (right) compared to a classical Savonius turbine without a deflector (left).

6.5.2.3   Power coefficient analysis

Figure 6.17 shows C_p as a function of the rotational angle for both cases, the standard design and with the optimal deflector plate, at $\lambda = 1.1$. It can be seen that the power coefficient clearly increases in the angular ranges between approximately $90° - 200°$ and $270° - 20°$, while it is moderately reduced in other ranges of the rotational angle. A better comparison is obtained by looking at the instantaneous C_p values, and considering the two blades separately, as shown in Figure 6.18. It can be seen that blade 1 produces a peak power in the range between $240°$ and $360°$, while the peak energy is generated in the range from $60°$ to $180°$ by blade 2. Accordingly, the power curve of the whole rotor shows two corresponding peaks. Here, blade 1 will be considered and compared individually for both cases, the standard design, and with the optimal deflector plate. The comparison is shown in Figure 6.19. As can be seen, the C_p value improved considerably in the angular range from $80°$ to $200°$, while the power coefficient was reduced slightly between $200°$ and $285°$. The reason for the behavior of C_p will be further explained in the next section.

6.5.2.4   Pressure distributions

In Figure 6.20, the average C_p of blade 1 using the optimal deflector plate is shown together with the instantaneous pressure distributions obtained from a sample cycle
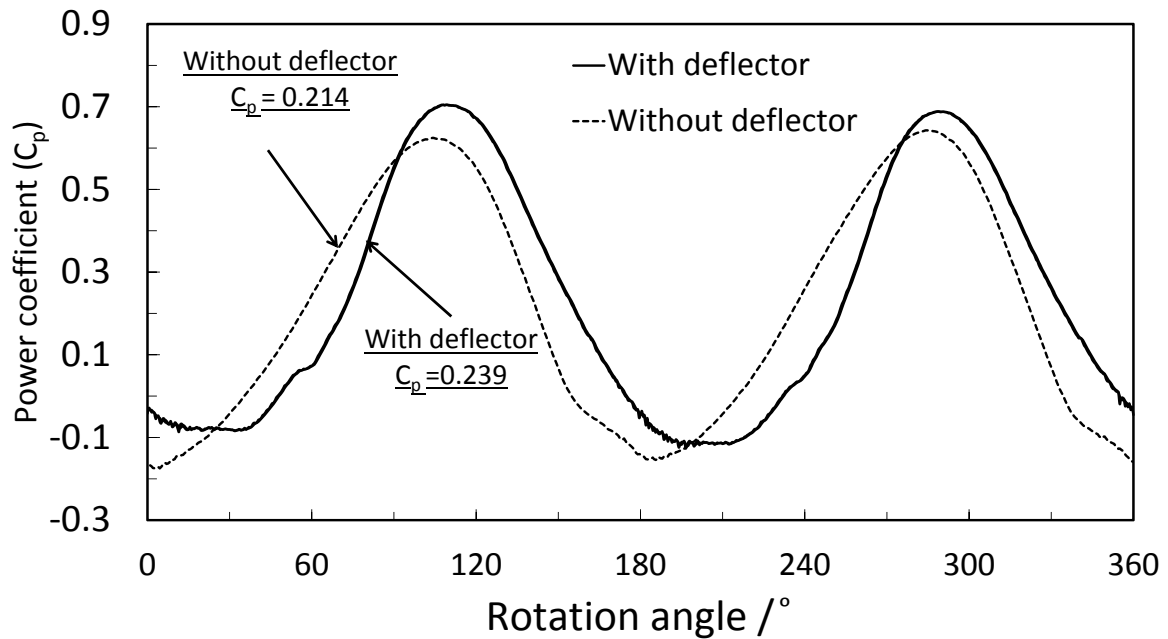
Figure 6.17: Comparison of the power coefficient C_p between the standard design and the configuration with the optimal deflector plate at $\lambda = 1.1$ for the whole rotor.
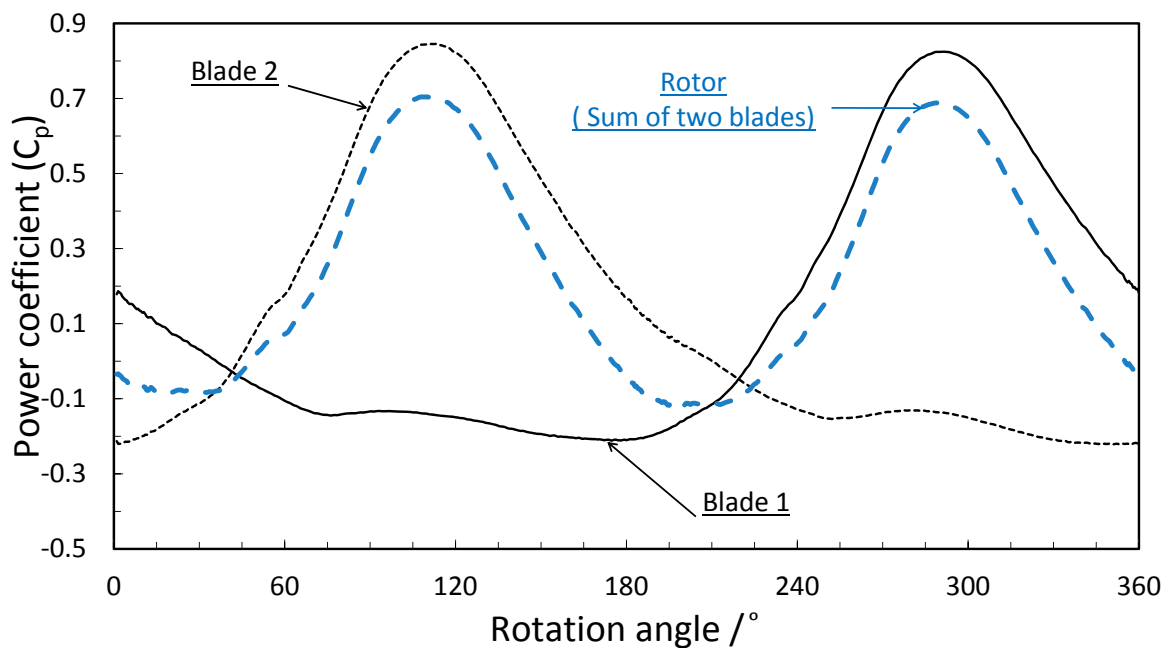
Figure 6.18: Power coefficient of blade 1, blade 2 and of the whole rotor for different angular positions.

(the last one, number 30) for different angular positions of the rotor between 0° and 315° discretized in 45° steps. By focusing on the pressure field along the back side of blade 1, the change in power coefficient can be best explained. For angles range
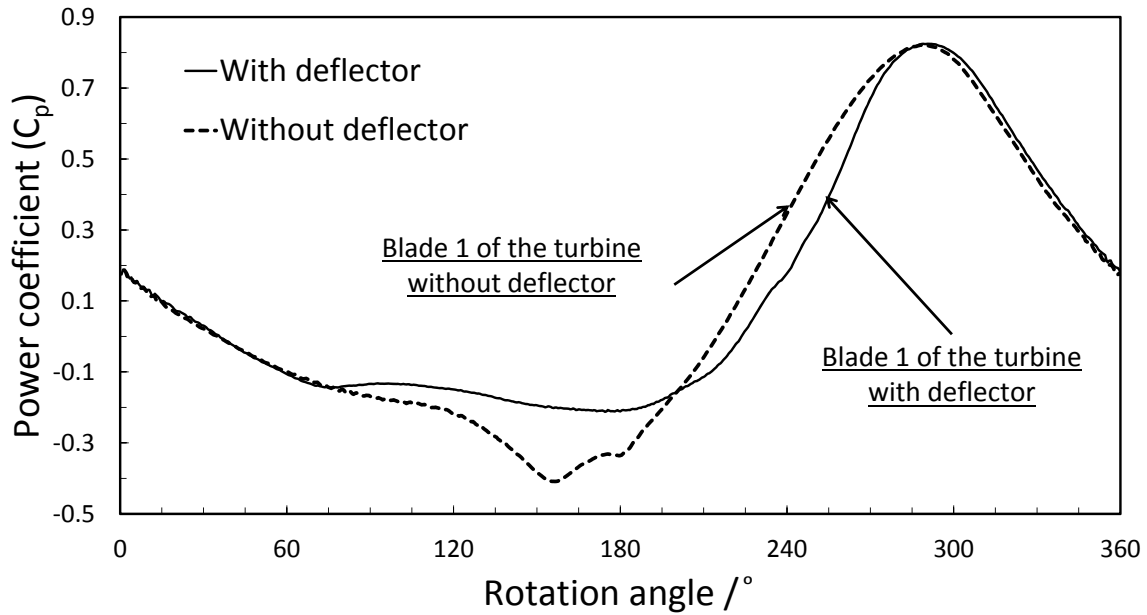
Figure 6.19: Comparison of the power coefficient C_p between the standard design and the configuration with the optimal deflector plate at $\lambda = 1.1$ for blade 1.

from 0° to 180°, the pressure over the back side of blade 1 increased noticeably with the rotational angle, resulting in a reduction in blade power. Contrarily, for the range from 180° to 315°, not only can a decreasing pressure over the back side of the blade be noticed, but also a sharp increase in the pressure on the front concave side. Due to the resulting pressure difference, a high positive power coefficient is produced by blade 1 in most of this range.

As already mentioned, it can be observed from Figure 6.19 that the main increase in instantaneous C_p when comparing the results with and without the deflector plate occurs in the range from 80° to 200°, with a slight reduction in C_p between 200° and 285°. These variations can be understood by looking at the pressure distributions around blade 1. Figure 6.21 represents the pressure distribution at two specific rotational angles (150° shown in Figures 6.21a and 6.21b, and 240° shown in Figures 6.21c and 6.21d) for both the standard design, and with the optimal deflector plate. While the angle 150° is clearly located within the improved domain, the angle 240° is in the reduced performance zone. By looking at the pressure distribution over the convex side (see next page) at 150° angle for both cases, it is evident that the pressure over the convex side of the turbine with a deflector plate is less than that of the turbine without a deflector plate, leading to a higher power in this range. On the other hand, at angle 240°, the pressure over the concave surface of the turbine with the deflector plate is lower than that of the turbine without the deflector plate, reducing the corresponding
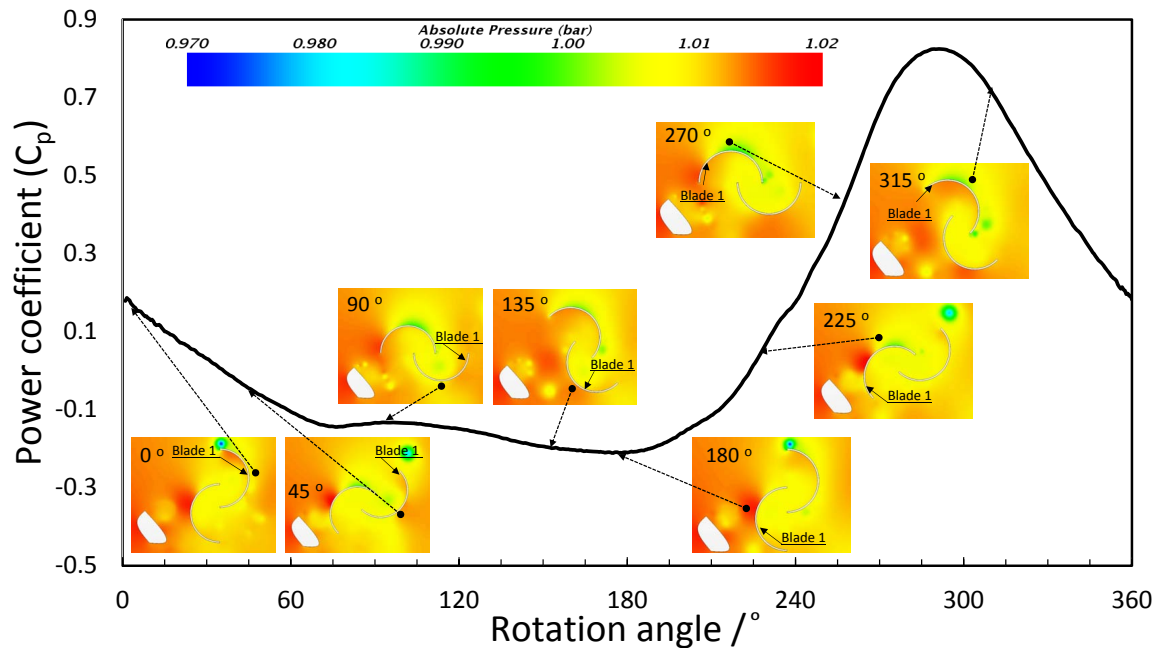
Figure 6.20: Instantaneous pressure distributions for different angular positions of the rotor with the optimal deflector plate overlaid on the average power coefficient C_p for blade 1.

C_p at this angular position.

For a better quantitative analysis, the pressure distribution along the advancing blade is now presented in the form of polar curves. Figure 6.22 shows the instantaneous pressure distributions obtained from a sample cycle (the last one, cycle 30) for the angular positions of 150° and 240°. At 150°, the pressure distribution of the concave surface for the turbine with the optimal deflector plate decreases slightly in comparison with the standard configuration. On the other hand, on the convex side, the pressure is greatly decreased, resulting overall in a high increase in the net produced power at this angular position. At 240°, the pressure does not change much along the convex side. At the same time, the pressure on the concave side decreases moderately. Consequently, the output energy is slightly reduced compared to the traditional configuration at this angular position. For a better view of the associated velocity field, Video (3) is available as supplementary material, which shows the results during the last 15 rotation cycles.

6.5.2.5 Complete operating range

Since many turbines will also be operated at off-design conditions, it is useful to check additionally how the optimal deflector plate will affect the operation of the turbine at any tip speed ratio. Therefore, the performance of the turbine has been computed for

(a) Turbine without a deflector plate (standard design) at 150°

(b) Turbine with the optimal deflector plate at 150°

(c) Turbine without a deflector plate (standard design) at 240°

(d) Turbine with the optimal deflector plate at 240°
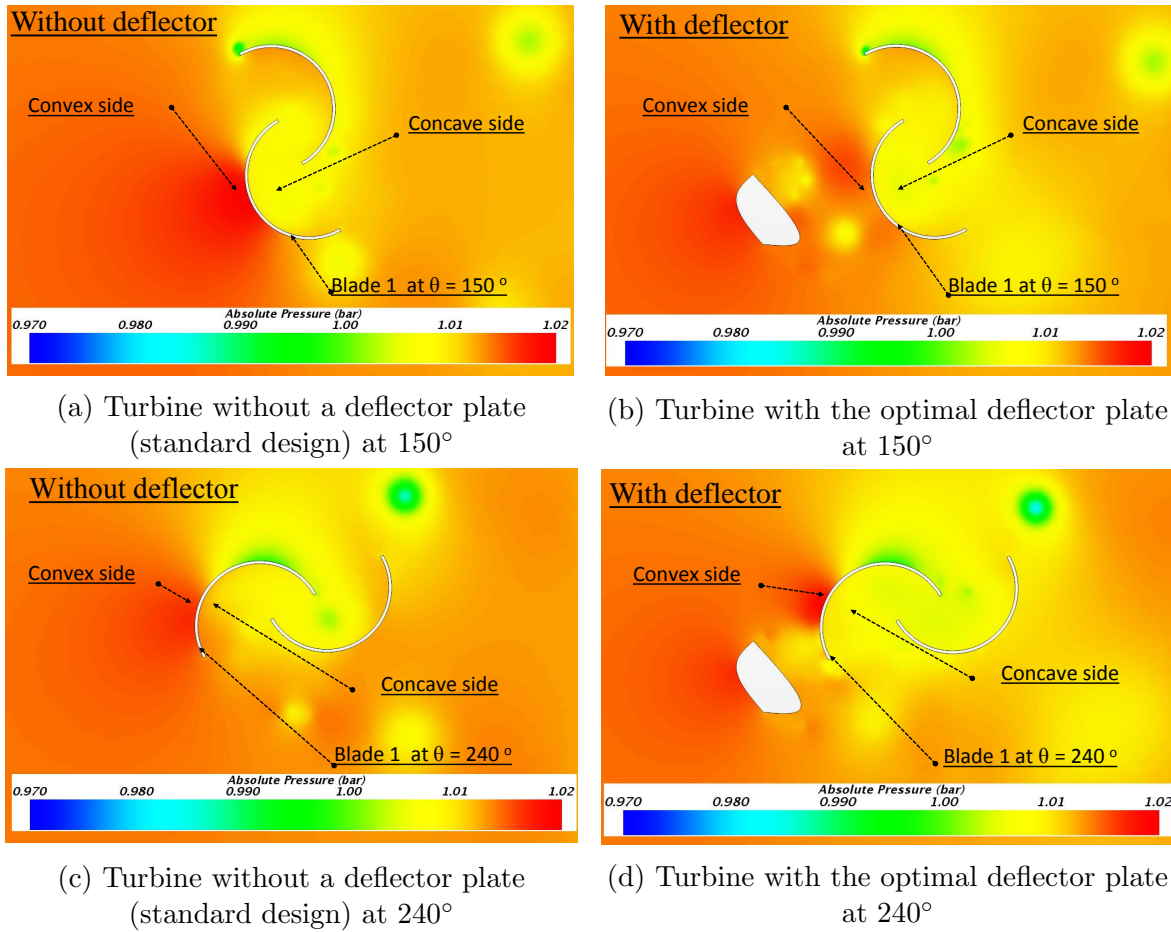
Figure 6.21: Pressure distribution around the blades for the standard design and for the configuration with the optimal deflector plate, at rotational angles of 150° and 240°, respectively.

both the standard design, and with the optimal deflector plate for the whole relevant range of tip speed ratio ($0.8 \leq \lambda \leq 1.2$), as shown in Fig. 6.23. As expected, the average torque coefficient decreases with increasing λ for both cases [38, 63, 105]. On the other hand, the improvement of both torque and power coefficient induced by the optimal deflector plate are clearly observed at all values of λ compared to the standard design without deflector plate. Moreover, the gain in C_p becomes particularly strong at higher λ, reaching 12% at $\lambda = 1.1$ and almost 15% at $\lambda = 1.2$. Thus, the optimal deflector plate is very effective at improving the power of the turbine at constant frontal area and without any additional complexity concerning the turbine blades.

6.5.3 Self-starting performance

Finally, the self-starting ability of the optimized system was checked by computing the static torque for each case (the standard design and the configuration with the
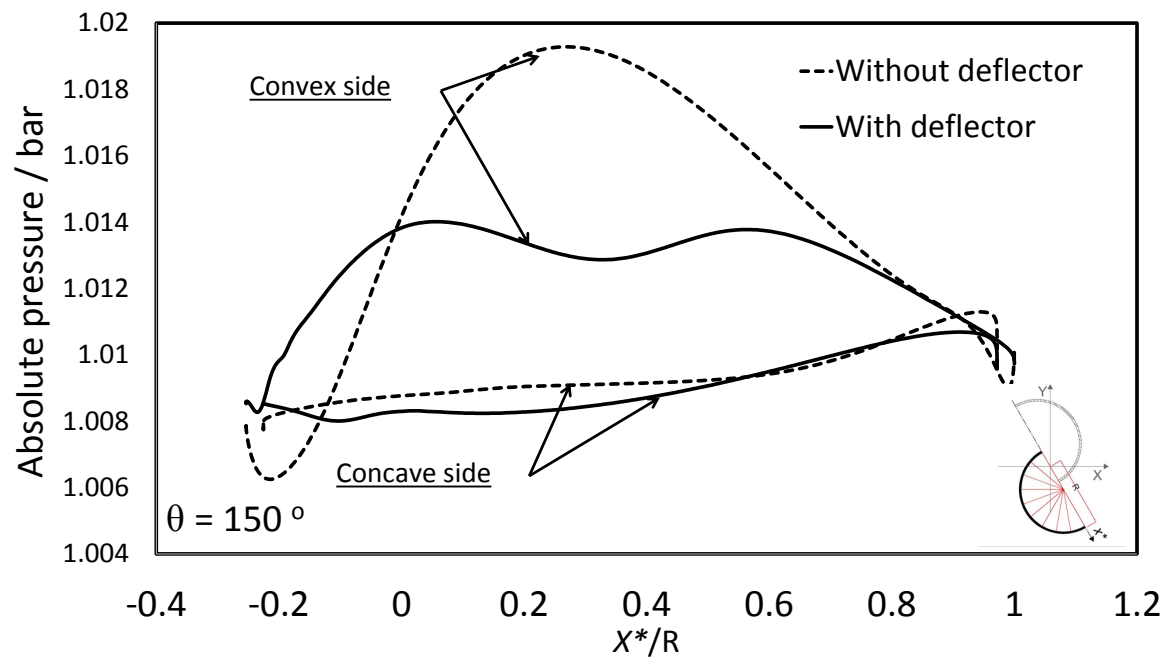
(a) 150°
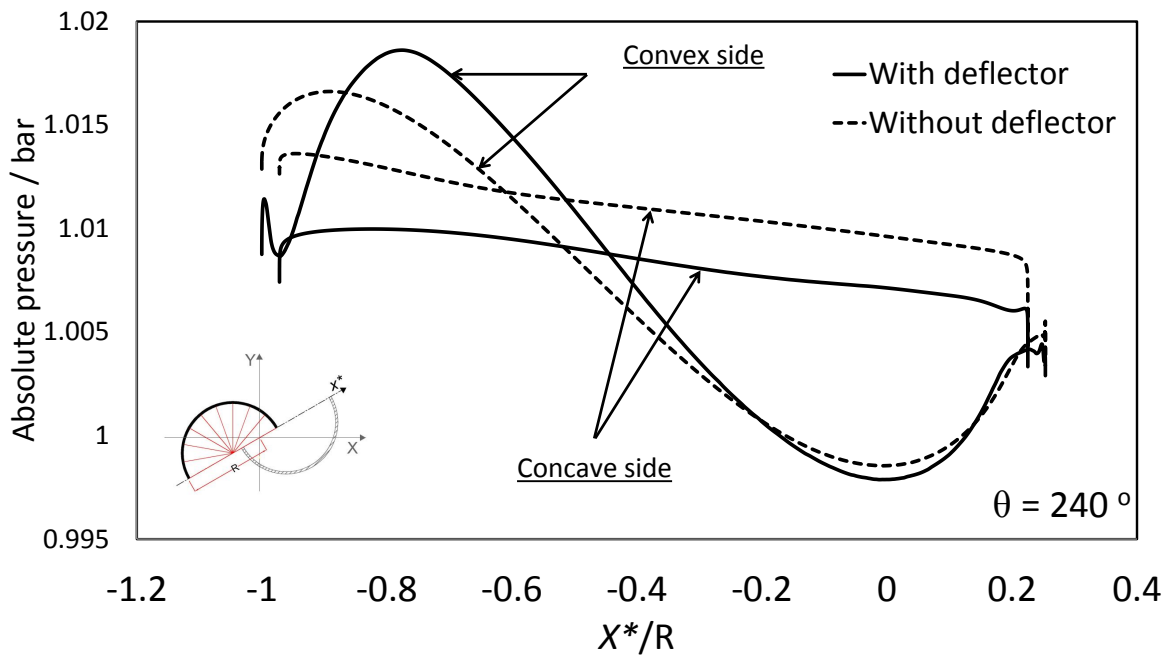
(b) 240°

Figure 6.22: The pressure distribution over the surfaces of the blades for the standard design and for the optimal configuration at angular position of (a) 150° (b) 240°.

optimal deflector plate) at fixed rotational angles. Figure 6.24 presents the relationship between the static torque coefficient for both configurations as a function of the fixed rotational angles (θ). The outcome is only presented for angles ranging from 0° to 180°. It is evident that both configurations show similar curves. For values of θ ranging
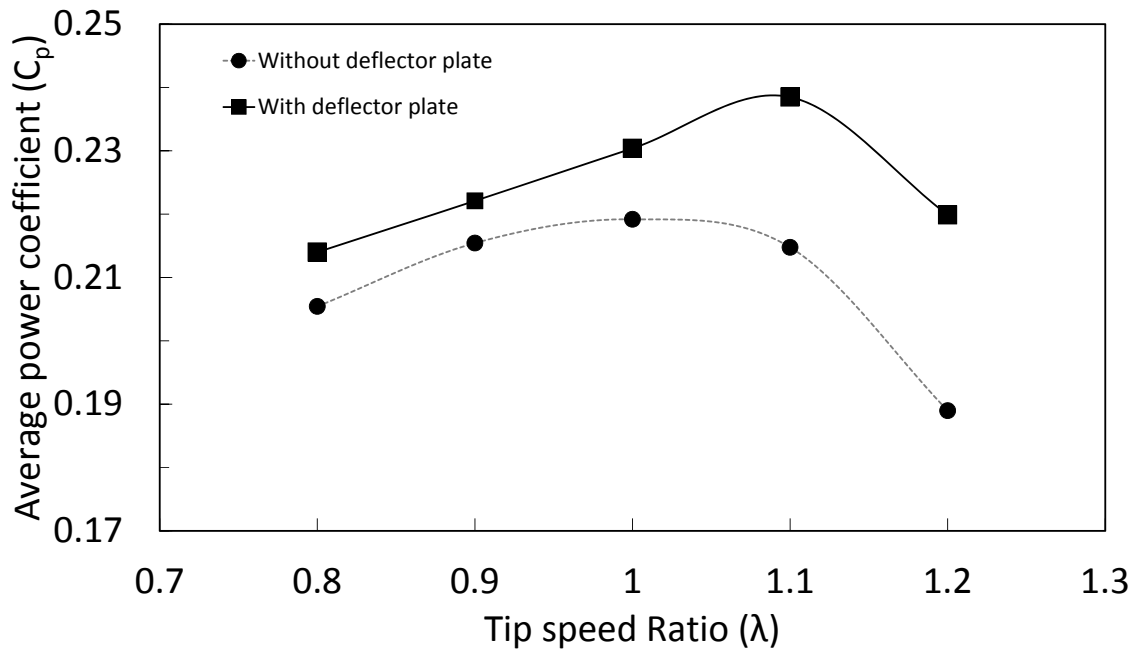
(a) Average power coefficient
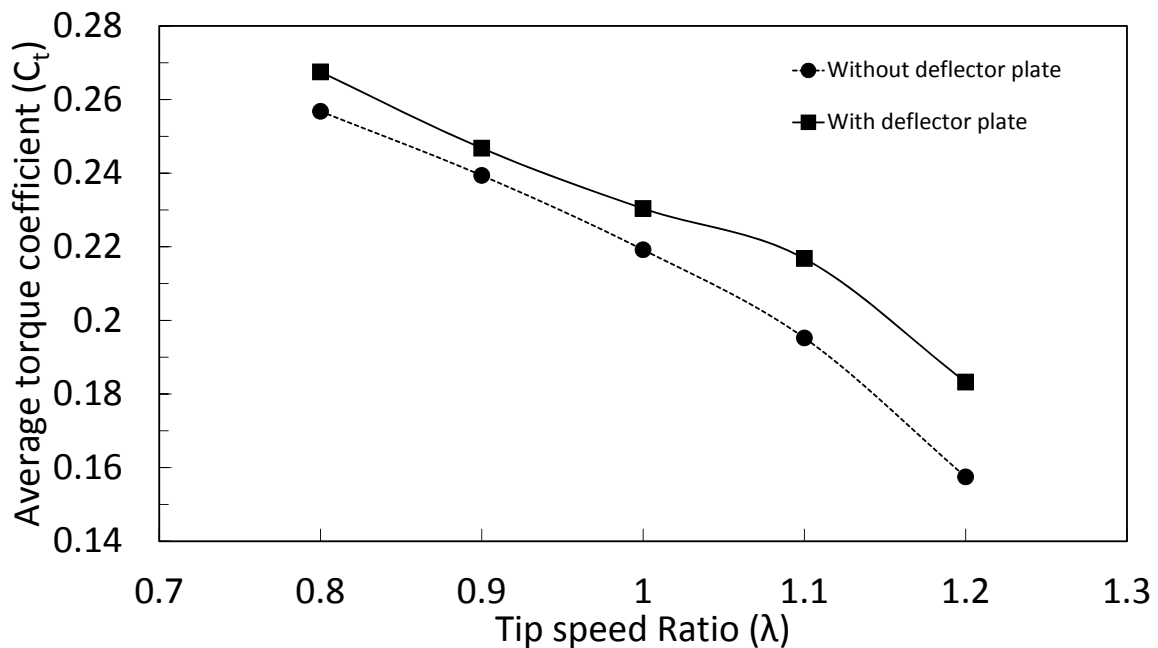
(b) Average torque coefficient

Figure 6.23: Comparison of the (a) average C_p and (b) average C_t at different tip speed ratios for the standard design (without deflector plate, dashed line) and for a turbine with the optimal deflector plate (solid line).

from 80° to 120°, the standard design has a slightly higher static torque coefficient compared to the optimal configuration, while the turbine with the optimal deflector plate shows better values for θ in the ranges 0°-40° and 140°-180°. Most importantly,

94

both configurations show self-starting ability ($C_{ts} > 0$) at all angles.
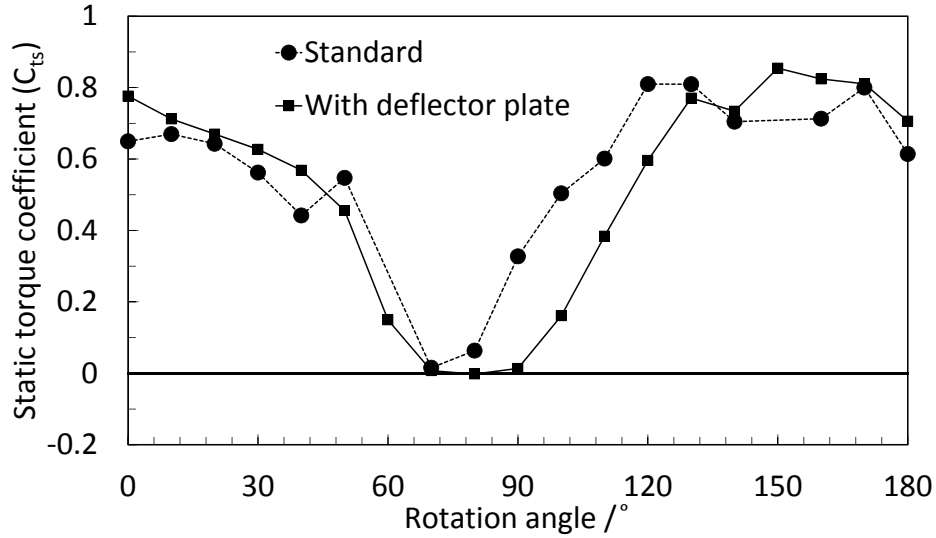
Figure 6.24: Static torque coefficient C_{ts} as a function of the fixed rotor angle θ for the standard design and for the turbine with the optimal deflector plate.

6.6 Experimental validation of the optimal deflector

Nowm it is important to check if this numerically predicted improvement is found in reality. Therefore, a 3D deflector plate was printed with the same shape and dimensions as the optimal deflector (Table 6.4) and added in the water channel in front of the standard turbine to check the improvement in performance. Figure 6.25 shows the standard Savonius turbine with the deflector inside the water channel. The same experimental setup, which was explained in detail in the previous chapter, was used but the deflector was now added at the front of the turbine. The measurements for the torque and the rotational speed were again recorded but with a larger-scale sensor (max reading of 2 N.m), as discussed in detail in the previous chapter. The performance of the turbine with a deflector plate was measured and compared with the standard Savonius turbine, as shown in Figure 6.26. It is clear now that the performance improved over all of tip speed ratios, in agreement with the numerical study. The calculation of the relative improvement now becomes more difficult because of the larger error in the experiments compared to the numerical model. The measurements have been repeated twice on different days. Figure 6.26 shows the experimental uncertainty with error bars. The difference between Figure 6.23a and Figure 6.26 is due to 3D effects (remember here that only 2D simulations are used for optimization) and the

limitations in the numerical model, for instance regarding turbulence. At $\lambda = 1.1$ the numerical model predicts an increase of C_p by 12 % . Taking into account all uncertainties, the experiments reveal an increase in between 10 % (minimum) and almost 40 % (maximum); both predictions are in good agreement and the numerical model error appears to be quite conservative, under-predicting the improvements found in reality. Overall, the optimization process is valid and goes in the correct direction, so that we can safely proceed further.
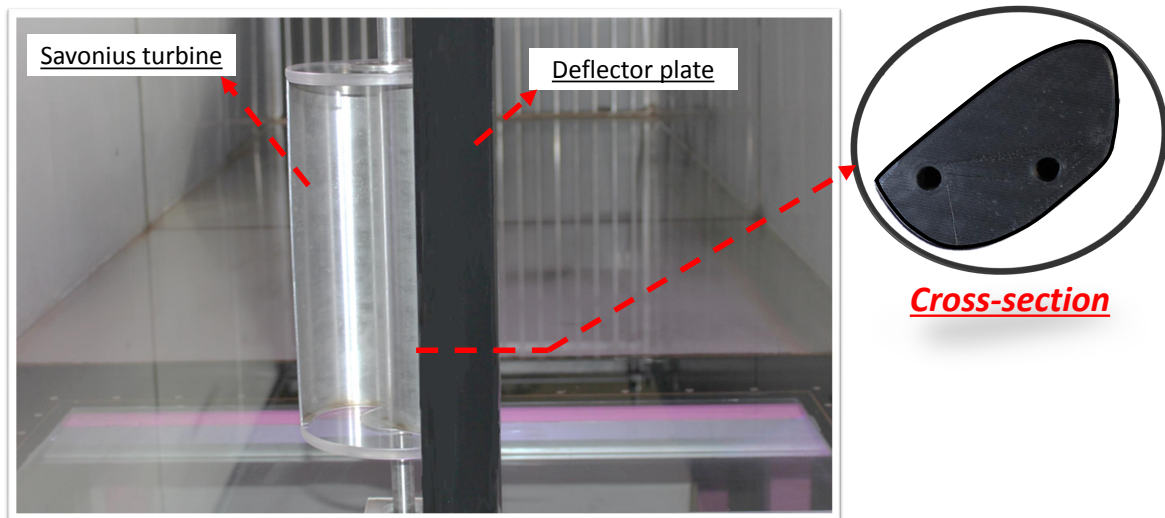
Figure 6.25: Frontal view of the standard Savonius turbine with the deflector plate inside our water channel.

6.7   Optimizing overlap, gap ratios and arc angles

6.7.1   Standard values for a Savonius turbine

Concerning the overlap ratio, there is no consensus for the best possible value in the published studies. Table 6.5 shows a summary from the literature of the optimal values for the overlap ratio; it fluctuates in a broad range between 0 and 0.3. Several studies concluded that a null gap ratio gives the best performance. At the end of this literature survey, a Savonius turbine with an overlap ratio of 0.22, a null gap ratio, and an arc angle of 180°, following [24] was considered as standard Savonius turbine in this study.
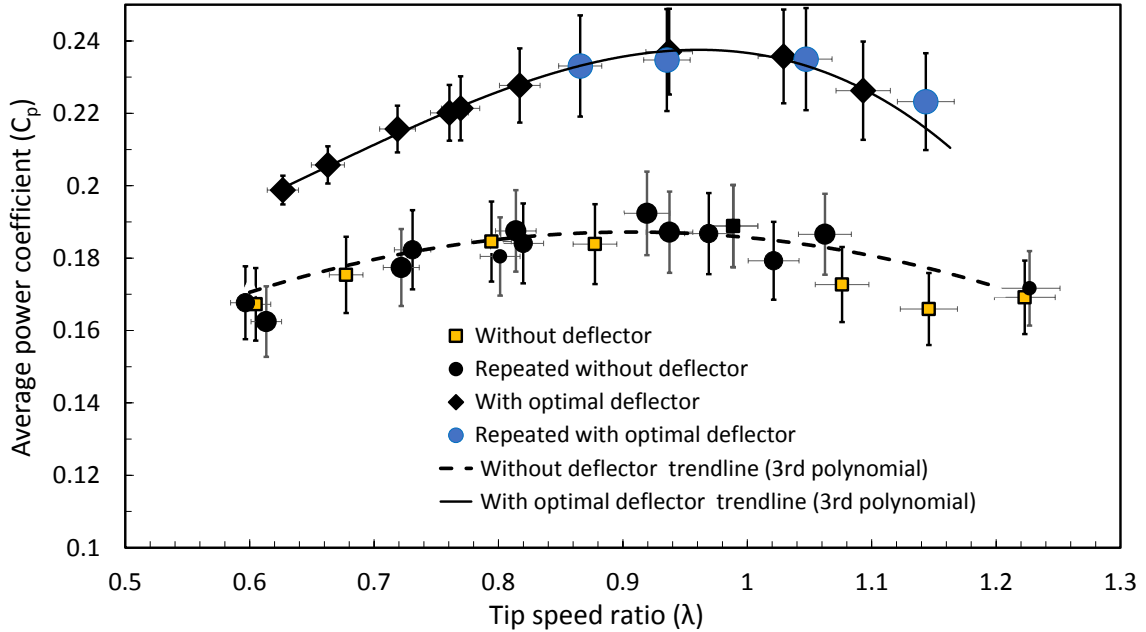
Figure 6.26: Experimental comparison of the average C_p at different tip speed ratios for the standard design (without deflector plate, dashed line) and for a turbine with the optimal deflector plate (solid line).

Table 6.5: Summary of studies concerning overlap ratio and corresponding optimal value

Author(s)	Year of publication	Optimal overlap ratio
Blackwell [18]	1977	$0.1 - 0.15$
Alexander and Holownia [19]	1978	0.2
Mojola [20]	1985	0.25
Ushiyama and Nagai [23]	1988	$0.2 - 0.3$
Modi and Fernando [21]	1989	0
Fujisawa and Gotoh [22]	1994	0.15
Menet [25]	2004	$0.15 - 0.3$
Jian et al. [26]	2012	0.167
Damak et al. [27]	2013	0.242

6.7.2 Parametrization and optimization procedure

The optimization process was again conducted at a fixed value of the tip speed ratio $\lambda = 1.1$, which is known to deliver the maximum power coefficient for the standard design.

Figure 6.27 shows a detailed diagram of the three parameters that were optimized. Table 6.6 presents the corresponding domain for each parameter, where $D(= 2R)$ is the total diameter of the turbine.
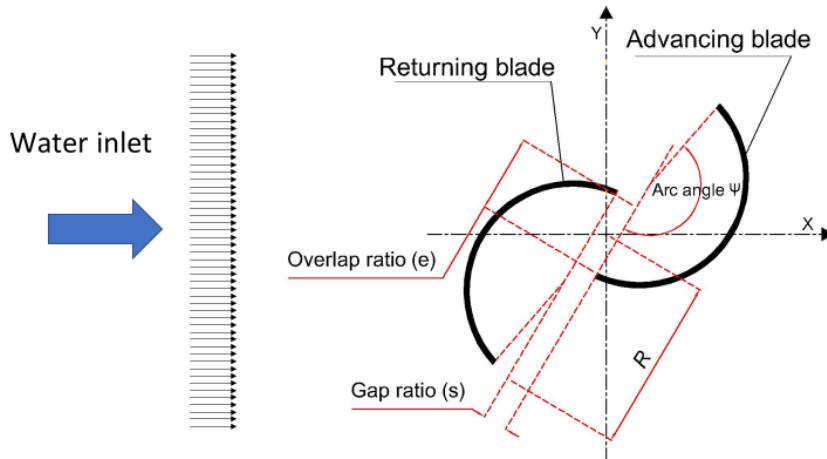
Figure 6.27: Schematic diagram of the geometry and free optimization parameters.

Table 6.6: Acceptable range for the input parameters

	Minimum	Maximum
Overlap ratio e/D	0	0.42
Gap ratio s/D	0	0.42
Arc angle ψ	90°	180°

6.7.3 Results and discussion

6.7.4 Optimal configuration

Figure 6.28 shows a parallel coordinate plot for the three input parameters on the left side and the target function in the right column. Each configuration is represented by a thin line while the thick black line depicts the optimal condition. Thin green lines show all of the improved turbines, i.e., all of the configurations corresponding to $C_p > 0.22$, clearly above the standard design value of 0.214. According to the green lines, the best operating range for the overlap ratio is between 0.1 and 0.2, with an optimal condition of 0.161. For the gap ratio, the range from 0 to 0.09 is the best operating range, with the optimal value being at 0.0233, close to 0. The optimal domain for the arc angle is between 162.5° and 170°, with the optimal value at 166.5°. Based on these findings,

the optimal configuration for a hydraulic Savonius turbine corresponds to $e = 0.161D$, $s = 0.0233D$, and $\psi = 166.5°$. When maintaining the same overlap and gap ratios but using the standard arc angle ($\psi = 180°$), the turbine performance only slightly decreased. Consequently, these two configurations will be compared with the standard turbine, denoted $S0$, in the next sections: $S1$, the fully optimal configuration, $S2$, a Savonius turbine with the optimal e and s, but the standard ψ. In that manner, the increase in power in both cases due to the change in overlap and gap ratios or the impact of changing the arc angle, can be clearly distinguished. These different Savonius turbines ($S0$, $S1$, and $S2$) will be simulated in a wide range of operating parameters to get a general view of the controlling processes.
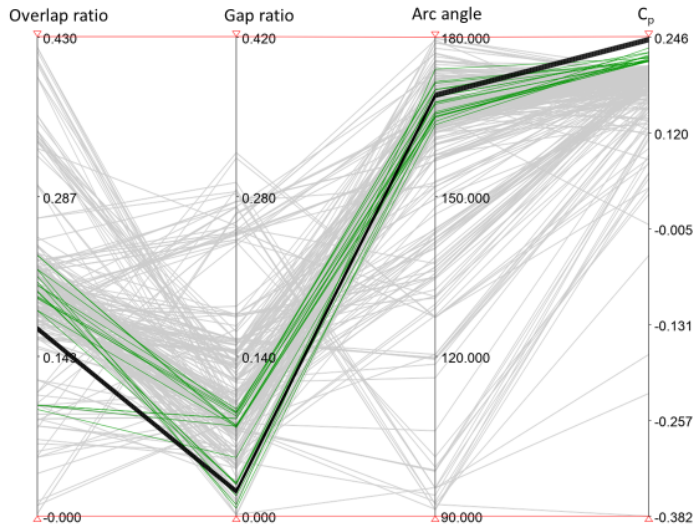
Figure 6.28: Input variables and objective function (power coefficient C_p) in a parallel coordinate system.

6.7.5 Effect of the overlap and gap ratios

Here, the performance of these configurations have been simulated for the entire operating range, $0.6 \leq \lambda \leq 1.2$, as shown in Figure 6.29. For each configuration, the performance usually increases with increasing tip speed ratio until it reaches its peak value, before decreasing again at high values of λ. The shape of the performance curve is standard and expected from the previous sections. It can be noted that the full optimal configuration $S1$ leads to the best performance over the whole range of tip speed ratios, not only at $\lambda = 1.1$, which was retained for the optimization process. As expected, configuration $S2$ with the standard arc angle lies between $S0$ and $S1$. This is again true over the whole range of operation. At $\lambda = 1.2$, the performance of all three designs is almost identical.
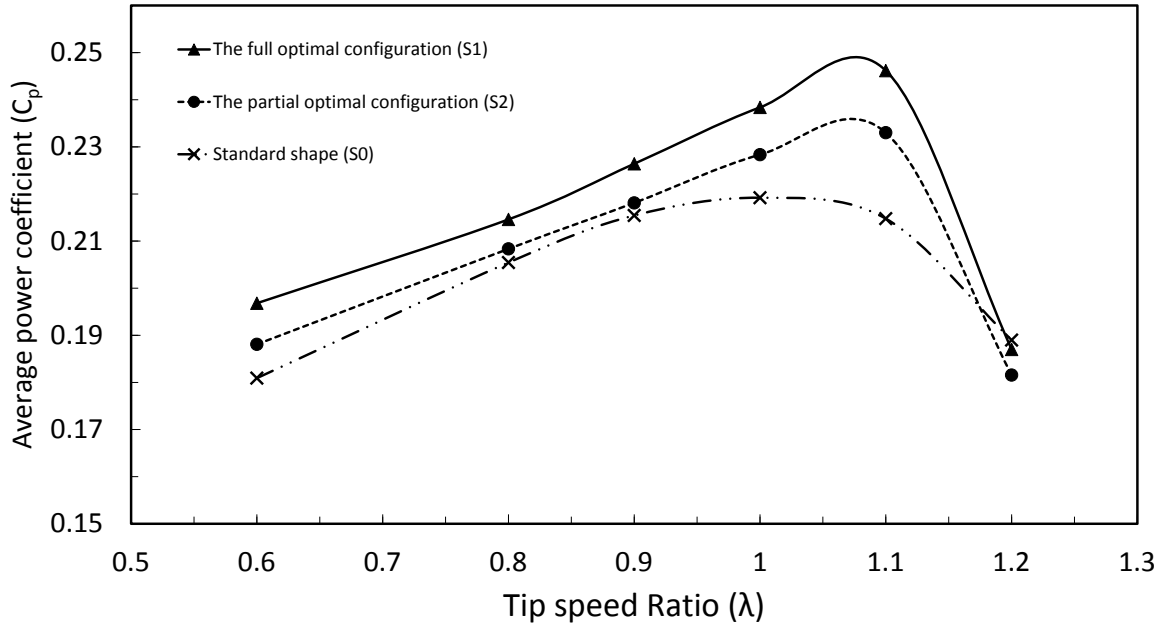
Figure 6.29: Comparison of the average power coefficient (C_p) for different tip speed ratios and different Savonius turbines: standard ($S0$, long dashed-and-dotted line), full optimal configuration ($S1$, solid line), and optimal overlap and gap ratio with standard arc angle ($S2$, dashed line).

At $\lambda = 1.1$, which was the value retained for the optimization, configuration $S2$ (optimized, but with the standard arc angle) enhances the performance of the turbine by about 6% in comparison with the standard shape, $S0$. By comparison, the optimal design ($S1$) leads to an increase in power coefficient by 11.5 %. This means that the performance gain is almost equally distributed between the arc angle and the overlap and gap ratios at this particular TSR value. For the rest of the characteristic line, the gain associated to the arc angle supersedes in general the impact of overlap and gap ratios.

6.7.6 Effect of the arc angle

As a consequence, the effect of the blade arc angle on the performance of the turbine has been analyzed in more detail. To quantify the impact of ψ on the power output of the turbine, the overlap and gap ratios were kept constant and optimal ($e = 0.161D$ and $s = 0.0233D$). Four configurations with different arc angles (140°, 150°, 166.5°, and 180°) were simulated over the entire range of operation ($0.6 \leq \lambda \leq 1.2$).

Figure 6.30 presents the average power coefficient as a function of the arc angle over the entire operation range. The peak power coefficient was obtained at $\lambda = 1.1$, as expected from the literature and already visible on Figure 6.29.
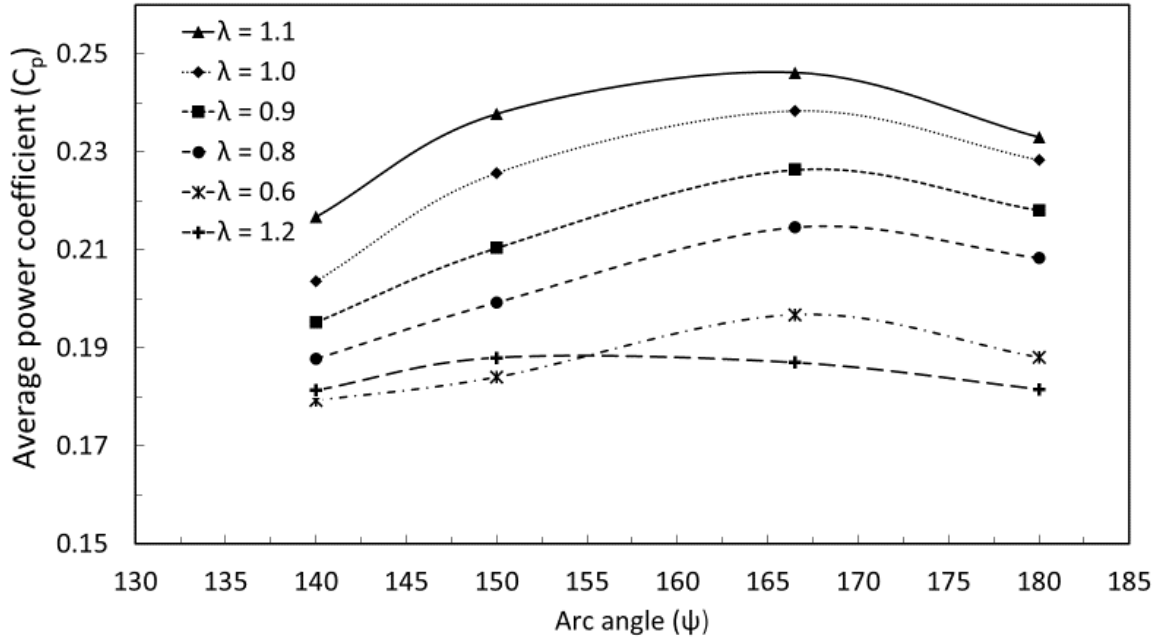
Figure 6.30: Comparison of average power coefficient (C_p) as a function of the arc angle for different tip speed ratios ($0.6 \leq \lambda \leq 1.2$) for Savonius turbines.

It can be seen from Figure 6.30 that there is a peak value for each curve. The power coefficient improves with increasing arc angle until it reaches a peak value; after that, it decreases when further increasing the arc angle. However, at $\lambda = 1.2$, the power coefficient is quite constant and low at any arc angle. Apart from this value, the peak values of the power coefficient C_p are always obtained for $\psi = 166.5°$, confirming that this is the optimal value quite independently from the tip speed ratio.

6.7.7   Self-starting performance

Finally, the static torque coefficient (C_{ts}) is computed as a function of the angular position for the standard ($S0$) and the optimal configurations ($S1$) in order to check if the resulting turbines are still self-starting. Figure 6.31 shows the results as a function of the angular position using a standard (Figure 6.31a) or polar representation (Figure 6.31b). Due to periodicity, Figure 6.31a is drawn only for angles between 0° and 180°. It can be seen that both turbines show a very similar self-starting curve. The standard turbine has a somewhat higher static torque coefficient in the range of 0° to 30°, while the optimal configuration shows a better static torque coefficient in the range between 70° and 110°. Both turbines show self-starting ability.
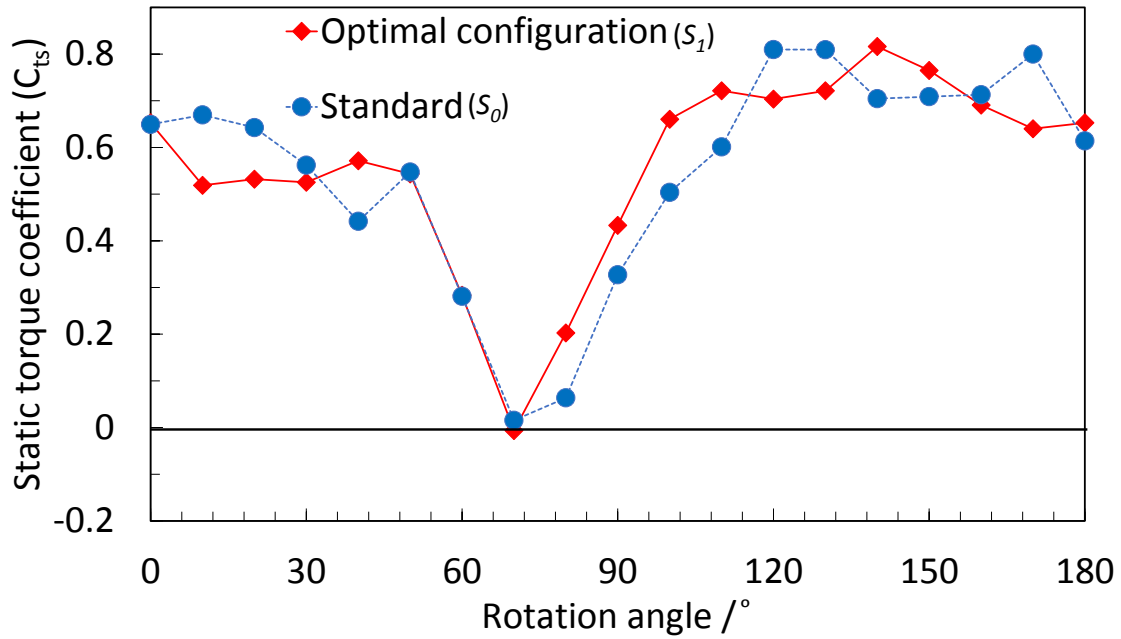
(a)
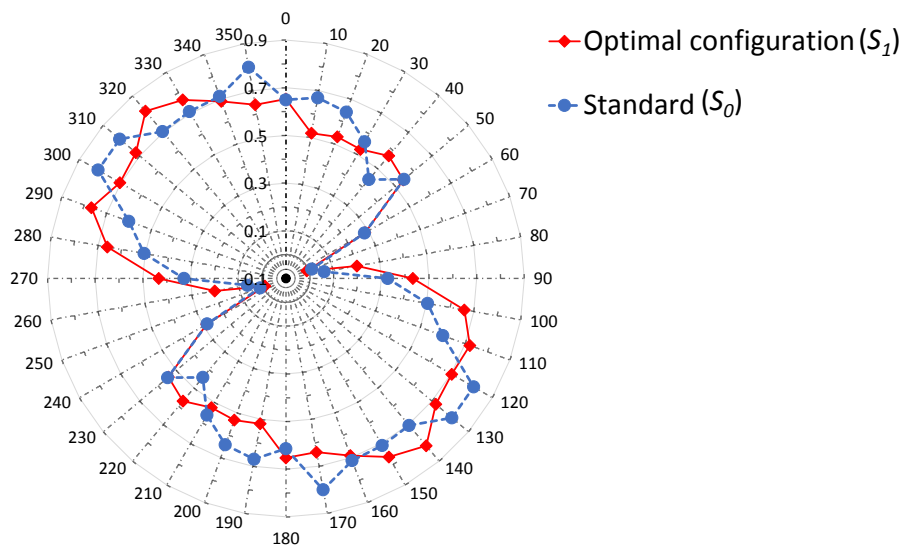
(b)

Figure 6.31: Static torque coefficient C_{ts} as a function of the fixed angular position of the rotor θ for optimal configuration (S_1) and standard turbine (S_0) in (a) standard (b) polar representations.

6.8 Optimization of thick blades with the optimal thick deflector plate

After optimizing separately deflector and blade, the optimal configuration of the deflector was now kept and the shape of the blade was adjusted to find the optimal configuration. The optimization process was performed similarly to the optimization of the blade, but the geometry was modified to add the deflector in front of the turbine. Figure 6.32 shows the fixed deflector plate with the blades described again by six adjustable points. Each point has two coordinates, so that twelve different input parameters are optimized simultaneously.

During the optimization process, 450 different configurations were simulated and the power coefficients were determined. Figure 6.33 presents the parallel coordinates for all the twelve input parameters in the 12 columns from the left. The objective function (C_P) is presented in the last column on the right. While the thin lines represent all configurations, the thick black line represents the optimal configuration. It is clear that the improvement compared to the standard Savonius turbine without deflector is almost 15%. However, the improvement compared to the standard Savonius turbine with an optimal deflector plate is only 3%. This is not a large increase in performance. However, the deflector was not optimized to fit the optimal thick blades. Therefore, this is only one step forward in the entire optimization process. Table 6.7 presents the optimal values for all adjustable points.
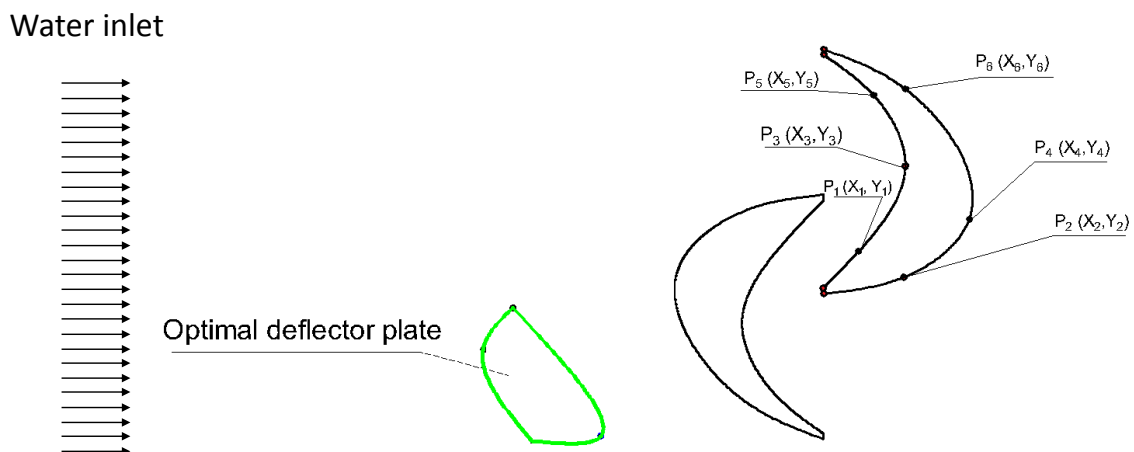
Figure 6.32: Geometrical description of the fixed optimal deflector plate and blade shape with movable points.

Figure 6.33: Parallel coordinates for all optimization input parameters. While the 12 columns from the left side indicate the blade's shape parameters, the right column presents the objective value (C_p).

Table 6.7: Optimal parameter values

	X/r	Y/r
P_1	0.411	0.496
P_2	0.976	0.233
P_3	0.5097	1.213
P_4	1.102	0.984
P_5	0.454	1.417
P_6	0.506	1.468

6.8.1 Presentation of the optimal configuration

the obtained geometrical configuration will be compared with the standard Savonius turbine. Figure 6.34 shows the comparison between the optimal blades with a fixed deflector and the standard Savonius turbine with the same deflector. When looking at the optimized blades, it is clear that the convex side is almost not changed compared to the standard Savonius turbine. On the other hand, the concave side was changed significantly and the thickness at the inner position of the blade was greatly enlarged. While the performance was improved compared to the standard Savonius turbine without the deflector, the performance improved by only 3% in comparison

with the standard Savonius turbine with the same deflector. This percentage is larger than the validation error in the numerical model but less than the uncertainty in the experimental setup. Therefore, it is acceptable from a numerical point of view but can not be checked experimentally. Still, this is not a substantial increase. Therefore, both the deflector plate and the thick blade will be optimized simultaneously later on.
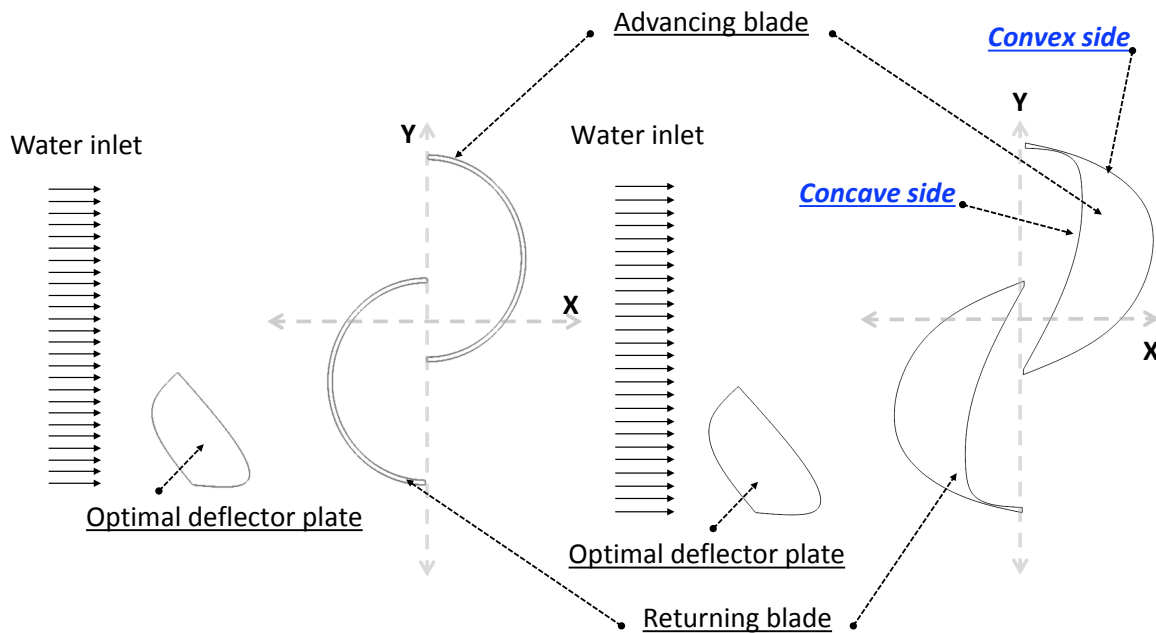
Figure 6.34: Optimal blade shape on the right compared to standard Savonius on the left with deflector in both cases (normally, the standard Savonius is used without a deflector). Here, the deflector is kept fixed during the optimization process.

6.8.2 Whole operating range

After determining the new geometry, it was tested over the whole operating range ($0.6 \leq \lambda \leq 1.2$). The performance was compared for three different configurations: the optimal thick blade with the deflector, a standard Savonius turbine with the same deflector, and a standard Savonius turbine without any modifications, as shown in Figure 6.35. The performance improves over the whole range, and increases relatively with decreasing tip speed ratio, reaching a maximum of almost 17% at $\lambda = 0.6$. Looking at the curves, it is clear that while the optimized thick blade is highly useful at low tip speed ratio, using the thick deflector plate improves the performance at high tip speed ratios.

Since the improvement was not very significant, there is no more need to go into more detail about pressure distributions. In the next section, the optimization of

the deflector while using the optimal thick blades will be discussed briefly, then the guidelines will be established in order to speed up the whole optimization process.
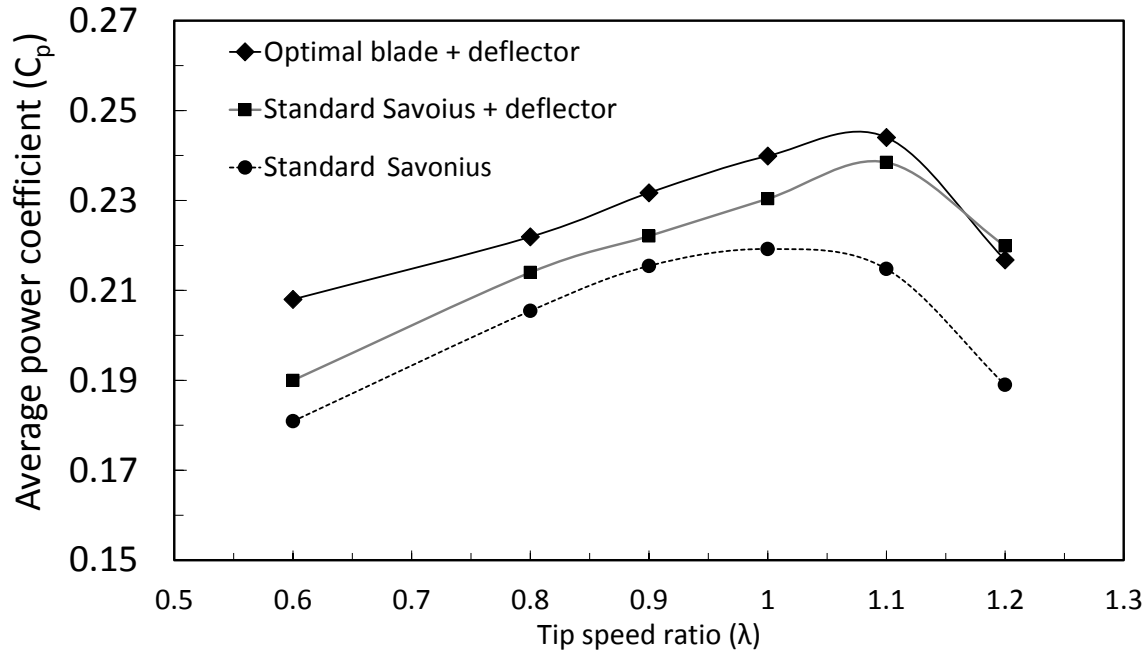
(a) Average power coefficient
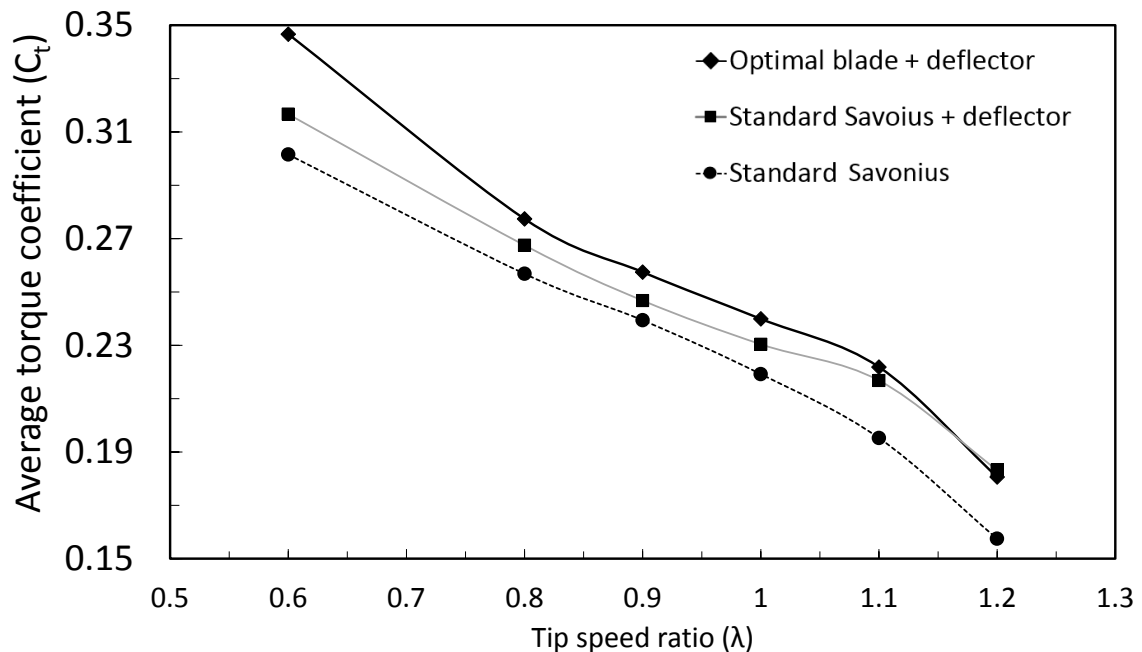
(b) Average torque coefficient

Figure 6.35: Comparison of the performance of a standard Savonius turbine with and without a deflector, and with optimal blade shape with the same deflector for (a) the average power coefficient and (b) the average torque coefficient as a function of the tip speed ratio.

6.9 Optimization of the thick plate while using the optimal thick blades

After using the optimal deflector to try to optimize the blades, it was important to reverse the process; thus keeping the optimal thick blades of Section 6.4 fixed while optimizing the deflector plate. The result will indicate the effect of the thick blades and thick deflector plate on the turbine's performance as well as the interaction between both quantities.

Figures 6.36 shows the movable points for the thick deflector plate and the fixed shape of the thick blades for the Savonius turbine. Seven variables were used to define the position and the shape of the deflector plate. The range for movable points and the constraints between the points was identical to the procedure used in Section 6.5.1.

As the idea of this section is only to check the influence of the shape of the blade on the deflector plate geometry and vice versa there is no need for an optimization process involving a large number of individuals or generations. If the performance does not improve much compared to the beginning of the optimization process, then the shape of the blades and the shape of the deflector must be optimized together, not separately. Consequently, only 250 validated configurations (5 generations) were selected. The results are shown in Figure 6.37.
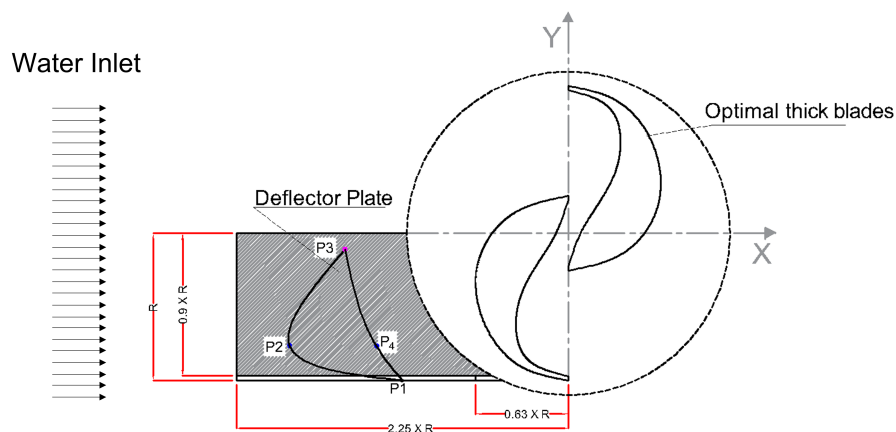
Figure 6.36: Geometry decription for fixed optimal thick blades and moving points for the thick deflector.

6.9.1 Optimization results

Figure 6.37 shows the parallel coordinates for the optimization process. While the seven left columns present the input parameters, the last column indicates the objective

107

function (C_p). The thick black line indicates the best configuration. Since there is no improvement in performance compared to the optimal thick blades alone (see section 6.4), the optimization process was stopped.
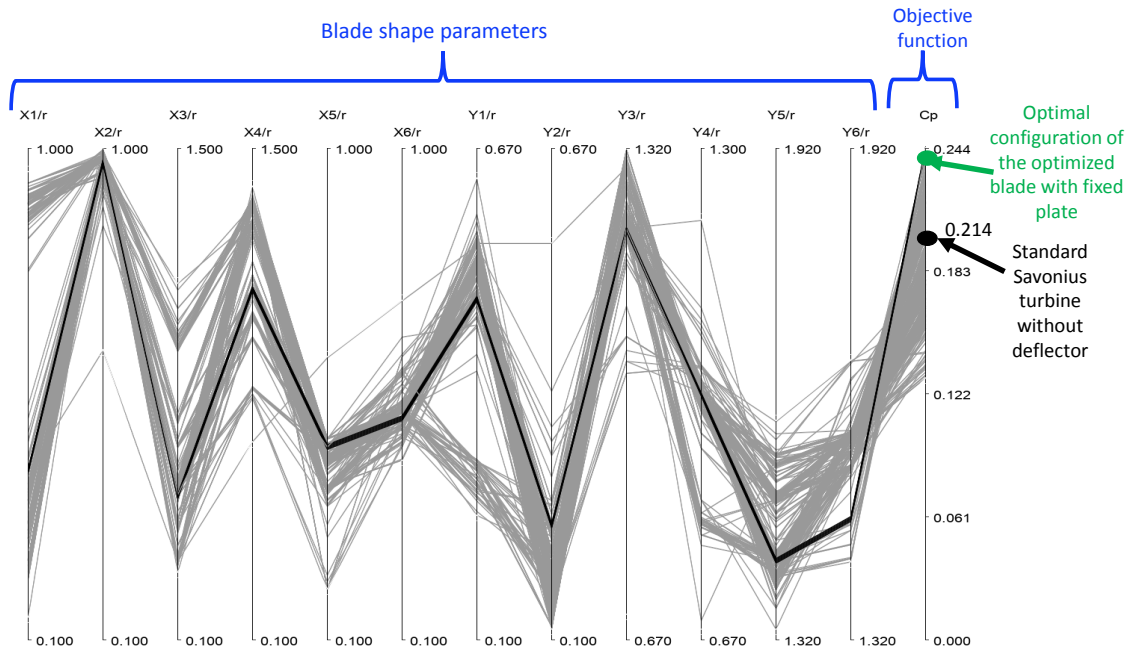

Figure 6.37: Parallel coordinates for the optimization input parameters. While the 7 columns from the left side indicate the thick plate's shape and position parameters, the right column presents the objective value C_p.

6.9.2 Geometry presented

It is important to check the deflector shape while using the thick blades, in order to have an impression of the outcome of the next section. Figure 6.38 presents the deflector plate and its position when also using the thick blades. This shape is not the final optimal shape that will be presented with the complete set of optimization parameters. While the deflector covers almost half of the blade from the outer side, it is situated almost $1.4R$ from the radius of the turbine in the x direction, as shown in Figure 6.38. This is similar to its position when a standard Savonius turbine was used, as illustrated in Section 6.5.2.2. However, the shape of the deflector changes substantially compared to a standard Savonius turbine. The shape consists of two sides. Side 1, which is slightly concave, is in front of the flow direction. Side 2 is convex and faces the turbine. Overall, it is clear that the shape of the deflector depends strongly on the shape of the blades, while the position changes slightly when either the shape of the deflector plate or the geometry of the thick blades is modified.
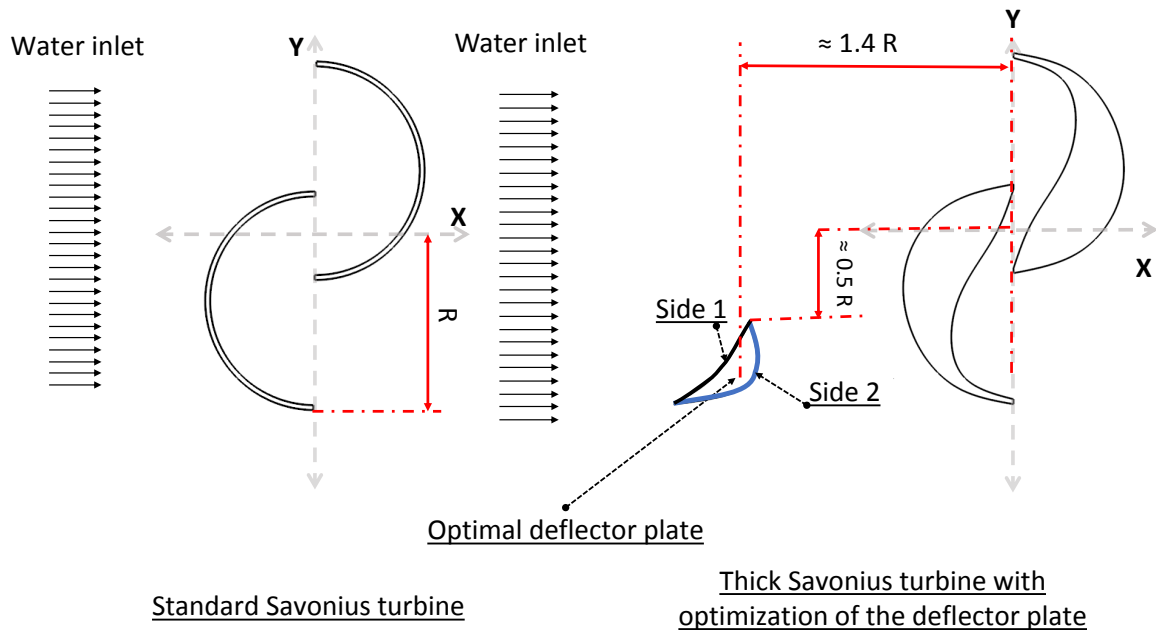
Figure 6.38: Geometrical comparison between a standard Savonius turbine and the thick blade with the optimal deflector.

6.10 Complete optimization process for the thick blades with a thick deflector plate, optimized simultaneously

In this section, a final step towards the optimal Savonius turbine in water will be presented. While all the parameters of the blade skeleton as well as the deflector shape and position will be simultaneously optimized, the three main parameters (overlap, gap ratio, and arc angle) will be kept constant. Of course, when the thickness and profile of the blade are modified, the shape of the gap between the blades is changed, but the values of gap and overlap ratios are kept fixed. With this procedure, the number of input parameters is minimized, and the efficiency of the optimization process is improved.

6.10.1 Parametrization and optimization procedure

In this aggressive optimization procedure, nineteen input parameters were simultaneously optimized. These parameters were twelve parameters for the shape of the blade, and seven parameters for the deflector plate controlling its position and shape (Figure 6.39). During the optimization process, the deflector plate should not increase the area swept by the turbine. Therefore, Y_{1p} will be fixed equal to the radius of the turbine.
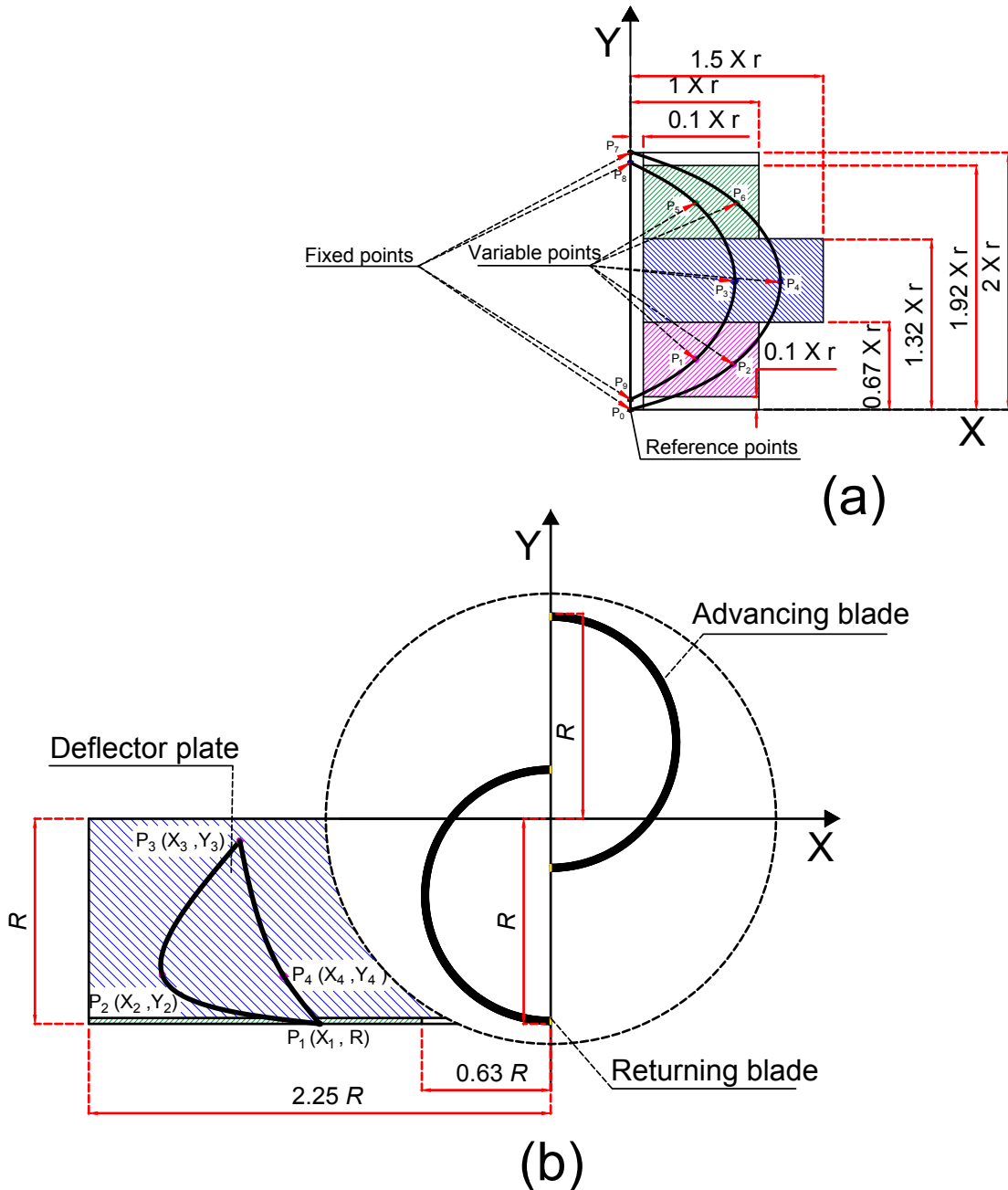
Figure 6.39: Geometrical description of the deflector plate and the thick blades in the optimization process.

In the optimization process, twenty generations were considered, containing 1950 evaluations with a valid geometry, mesh and CFD computation. All valid evaluations are presented in Figure 6.40. While the X-axis represents the evaluation number, the Y-axis shows the objective function (C_p). The figure focuses only on the best values, which are larger than for the standard Savonius turbine. In the small inset, the whole

data set is shown. The blue points indicate the complete evaluation configurations. The red line, connected the best values found during the process. With increasing numbers of generations, the improvement becomes slower, then saturates.
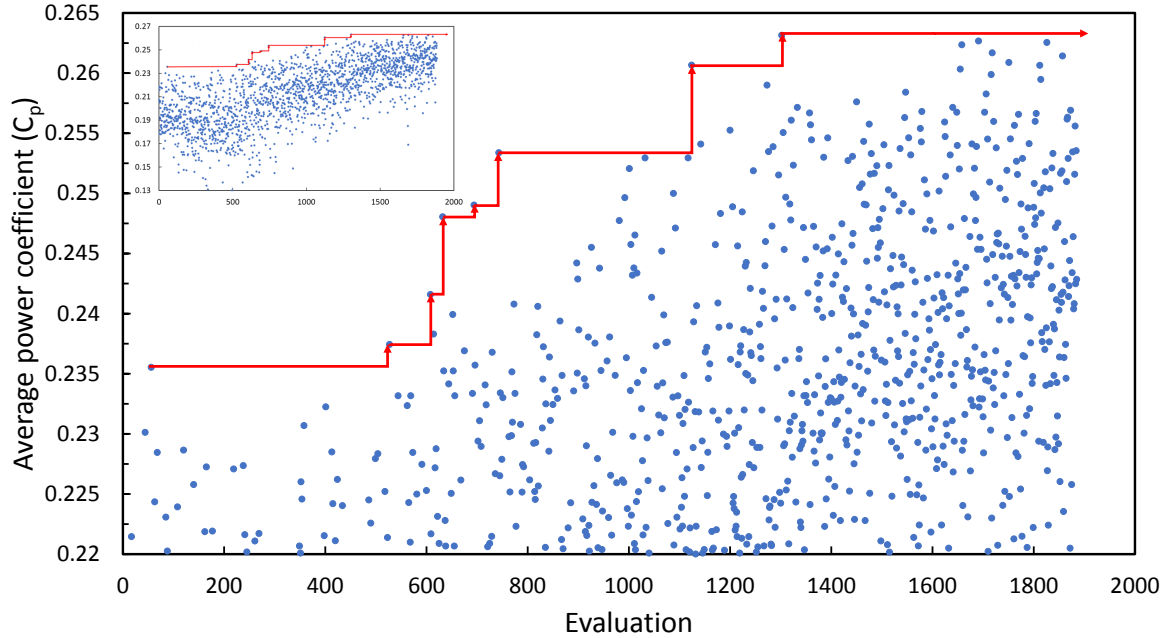
Figure 6.40: Optimization procedure and convergence process (main figure: $0.22 \leq C_p \leq 0.265$; inset: $0.13 \leq C_p \leq 0.27$).

Results from the complete optimization process are presented as parallel coordinates in Figure 6.41. The input parameters are presented in the 19 columns from the left and the last column represents the corresponding power coefficient (C_p). Almost 2000 different configurations were tested, which are represented by the thin lines in Figure 6.41. Four different configurations , which produced the highest values of the power coefficient were finally selected as represented by the four thick colored lines; i.e black (S_1), orange (S_2), red (S_3), and blue (S_4). Those four configurations will be analyzed in detail and compared with each other as well as with the classical (standard) shape. It is clear that the performance of the Savonius turbine was greatly improved by optimization. At $\lambda = 1.1$, the power coefficient is increased by 0.051 (absolute), which means a relative increase of almost 25%. Table 6.8 presents the coordinates for all movable points for all four configurations.

6.10.2 Comparison of the four optimal configurations

In this section, the four configurations will be discussed and compared with the standard Savonius turbine (without deflector), as shown in Figure 6.42. The comparison will be divided into two parts: 1) comparison of the thick blades, and 2) a comparison
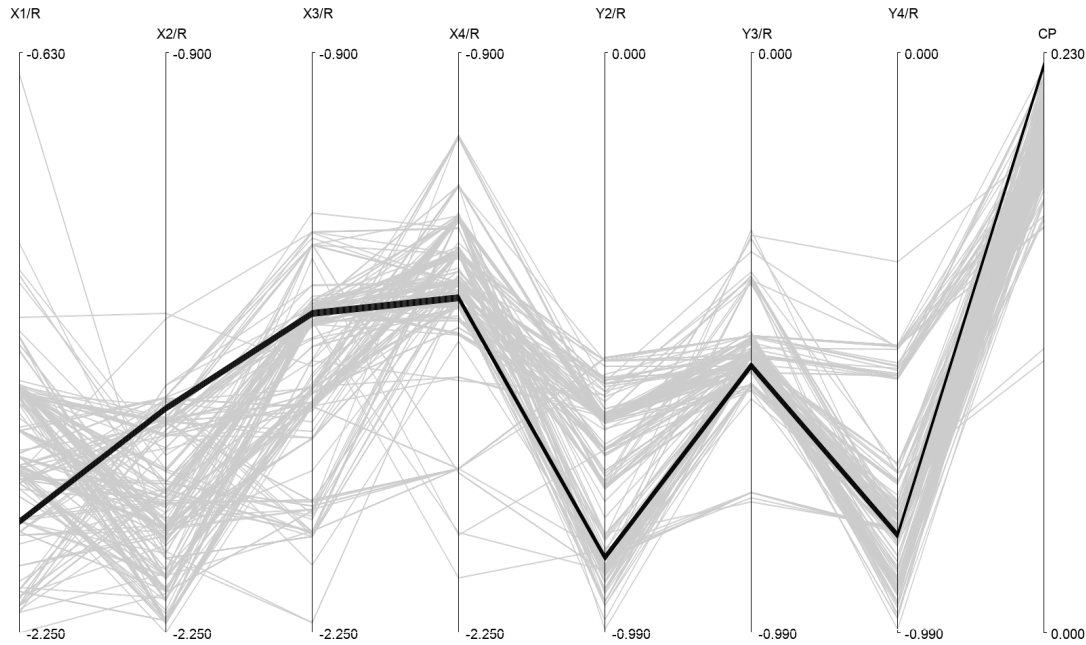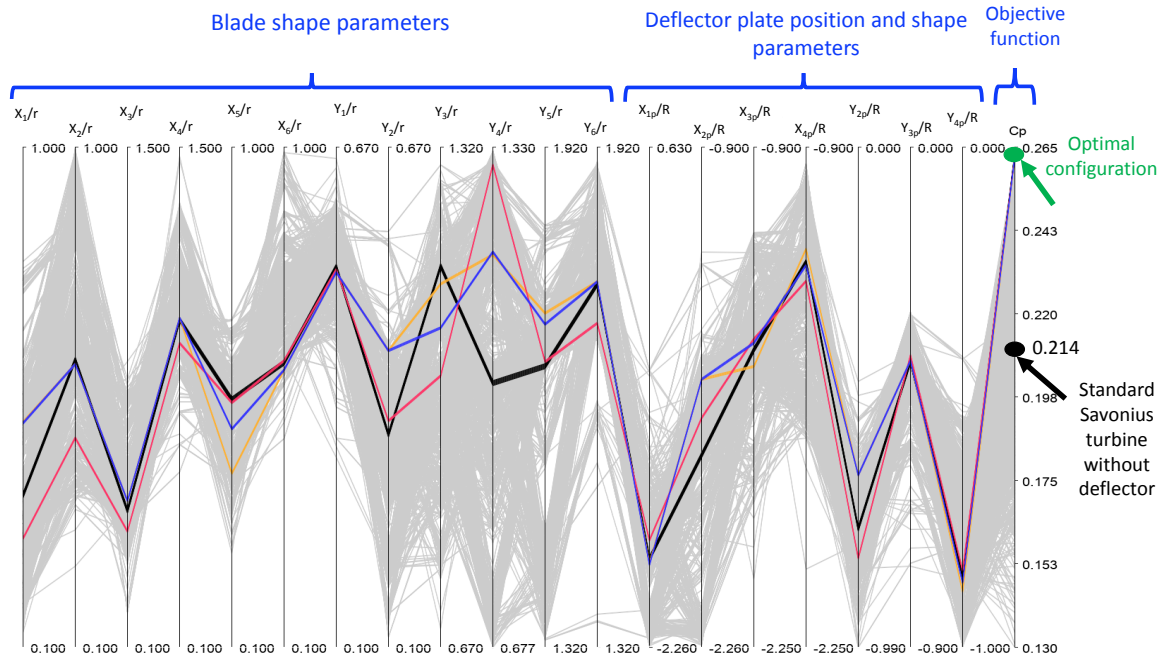
Figure 6.41: Parallel coordinates for the complete optimization input parameters; the 12 columns from the left side indicate the blade's shape parameters, these are followed by 7 columns of input parameters for the position and shape of the deflector. The right column represents the objective value (C_p).

of the different deflector plates. At the end one of those configurations will be selected as the best design on an engineering basis.

First, the thick blades are compared. While the convex side of each configuration is not significantly modified compared to the standard profile, the concave sides are very notably changed, as shown in Figure 6.42. Generally, the optimal concave side could have two different configurations; either a broad portion in the middle with raised outer segments (shapes S_1 and S_2) leading to a "dishware" shape; or one big flat segment starting from the center with a sharp bend at the outer part, producing a "hooked" shape (S_3 and S_4 configurations). Moreover, the middle portion of the blade can be slightly wavy (S_1 or S_3) or flat (S_2 or S_4), according to the shape of the deflector plate.

The optimal position and shape of the deflector plate will now be described. It is clear that, for all the configurations, the overall position is almost fixed. While the deflector covers approximately only the outer half of the returning blade in the Y direction, it is placed far away from the center of the turbine, at about $1.4R$. The shape of the deflector is described by two sides. Side 1 (blue thick line) is facing the turbine, and Side 2 (green thick line) is facing the incoming flow. Side 1 has a similar shape for all of the configurations, which is a rounded triangular structure with slightly different inclinations. Side 2 can be either in cambered convex form (S_1 or S_3) when the blade has a wavy shape on the concave side, or a depressed concave structure (S_2,

Table 6.8: Optimal values for the four configurations

	Blade skeleton							
	S_1		S_2		S_3		S_4	
	X_i/r	Y_i/r	X_i/r	Y_i/r	X_i/r	Y_i/r	X_i/r	Y_i/r
P_1	0.3747	0.5342	0.5056	0.5277	0.2968	0.5307	0.5035	0.5277
P_2	0.6179	0.3433	0.6104	0.4382	0.4769	0.3582	0.6099	0.4382
P_3	0.4839	1.1660	0.5102	1.1421	0.4254	1.0228	0.5100	1.0857
P_4	1.0176	1.0226	1.0230	1.1900	0.9518	1.3075	1.0230	1.1938
P_5	0.5467	1.6582	0.4131	1.7212	0.5403	1.6625	0.4929	1.7075
P_6	0.6129	1.7562	0.5996	1.7590	0.6167	1.7094	0.5996	1.7590
	Plate position and configuration							
	X_i/R	Y_i/R	X_i/R	Y_i/R	X_i/R	Y_i/R	X_i/R	Y_i/R
P_{1p}	-1.7435	-1 (set)	-1.7713	-1 (set)	-1.6411	-1 (set)	-1.7802	-1 (set)
P_{2p}	-1.7366	-0.7539	-1.5299	-0.6492	-1.6349	-0.8137	-1.5312	-0.6492
P_{3p}	-1.4451	-0.3850	-1.4913	-0.3833	-1.4176	-0.3743	-1.4286	-0.3833
P_{4p}	-1.2079	-0.8571	-1.1744	-0.8879	-1.2605	-0.8463	-1.2174	-0.8709

S_4) when the blade has a flatter shape on the concave side.

Overall, while the thick blades should have almost a half-circular profile on the convex side, the concave side should be either in a hook form or have a dishware structure. In the end, the hooked shape should be easier to manufacture. This is also the case for a flatter shape, not a wavy structure. Finally, S_4 is the best configuration from a manufacturing point of view, with a flat Side 2 for the deflector and a flat central part for the blade.

6.10.3 Power coefficient comparison

For a better comparison of the performance, the performance of only a single blade will be presented for the five configurations, i.e., the four optimal configurations and the standard shape. Figure 6.43 shows the variation of the instantaneous C_p as a function of the rotational angle. It is clear that the performance, for all of the optimal configurations compared to the standard shape improved almost over the whole cycle except in the range between 200° and 260°. In that range the standard shape produces
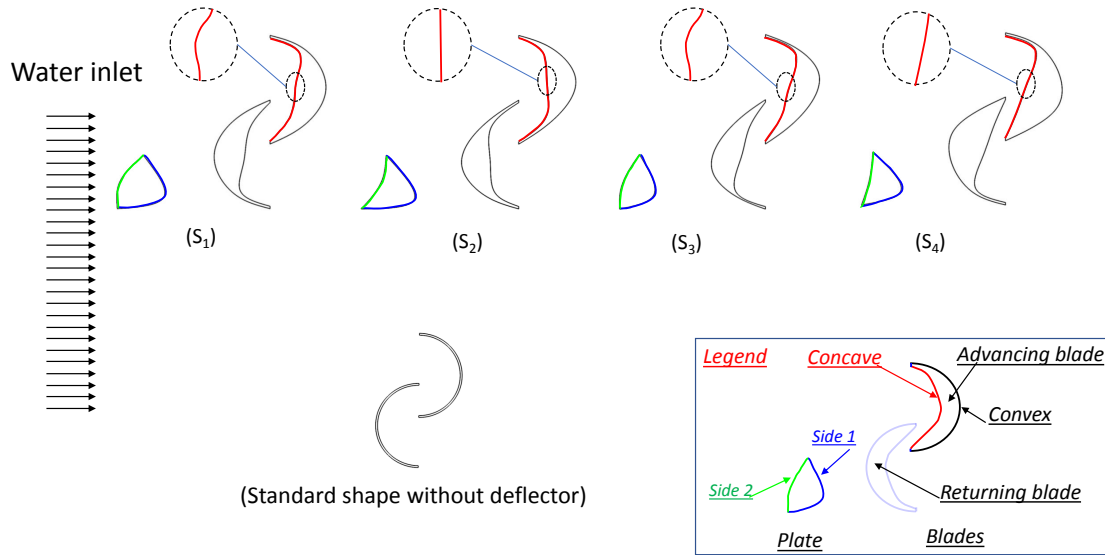
Figure 6.42: The four optimal configurations (top) compared with the standard shape (bottom).

a slightly higher power coefficient.

To explain the variation of the instantaneous C_p, the pressure distributions around the blades were compared for the optimal configurations and the standard shape. Since $\theta = 150°$ lies in the improved range while $\theta = 240°$ is in the reduced range, the pressure distributions at both angles will be analyzed to clarify the reason for the improvement of the turbine.

6.10.4 Pressure comparison

For the improved condition ($\theta = 150°$), Figure 6.44 presents the pressure distribution for all five configurations (S_0, S_1, S_2, S_3, and S_4) at the selected angle, where S_0 indicates the standard shape and S_1 to S_4 indicate the four optimal configurations. While the pressure is strongly reduced on the convex side for all of the optimal configurations compared to the standard shape, the pressure on the concave side is not changed significantly.

For a more quantitative analysis, the pressure distributions are presented as polar curve in Figure 6.45. While S_4 is represented by thick blue color, the rest of the optimal configurations are represented by transparent colors, since S_4 appear as the best configuration from a manufacturing point of view. On one side, all optimal configuration show similar trends except for S_2 (transparent orange lines). For the S_2 configuration, the pressure is highly decreased on both sides. For the S_4 configuration,
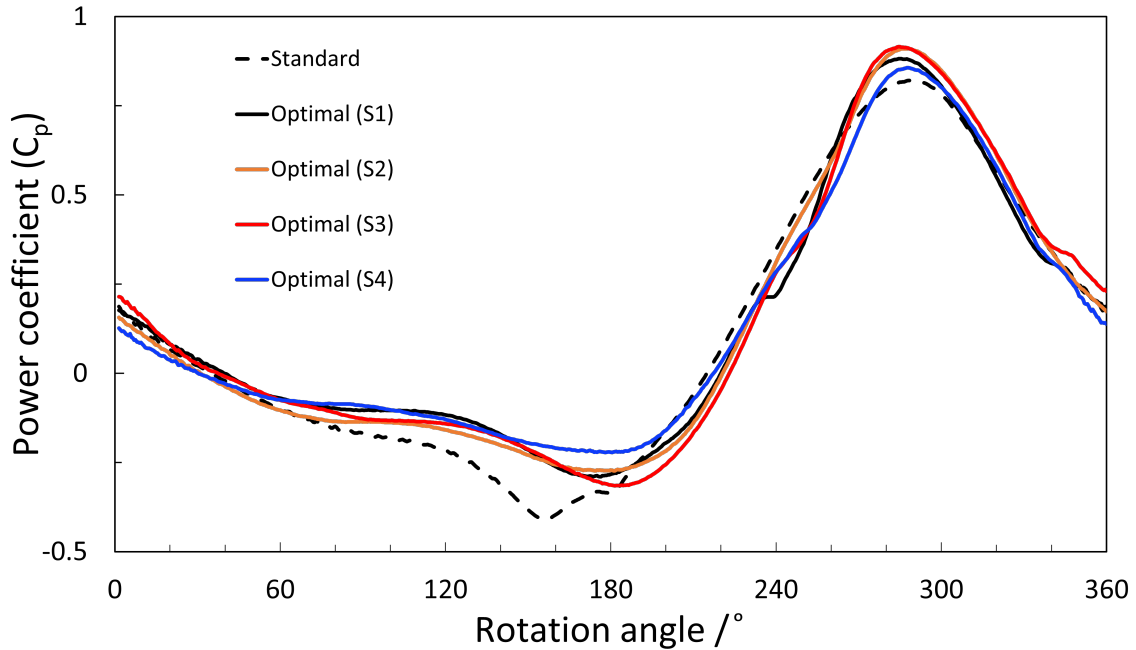
Figure 6.43: Comparison of the instantaneous C_p for the four configurations and a standard Savonius turbine for Blade 1.

while the pressure is decreased on the concave side over about 50 % of the blade, the pressure is greatly reduced on the convex side over almost 70 % of the blade length. Thus, the net produced power is improved. For the rest of the blade, the pressure on the pressure side increased. However, the pressure on the suction side also increased compared to the standard configuration, which clearly explains that the power was greatly improved over the whole blade length. so that the performance of the turbine was improved in that range.

For the reduction situation ($\theta = 240°$), Figure 6.46 shows the pressure field distributions around the blades, while the quantitative values are presented as polar coordinates in Figure 6.47. From both figures, it is clear that the pressure increases on the convex side, which hinders the movement of the blades. Moreover, the pressure on the concave side also decreased, explaining further the reduction.

6.10.5 Complete operating range

It is useful to check the effect of the optimal shapes for different tip speed ratios. The average power coefficient is presented in Figure 6.48a while Figure 6.48b shows the torque coefficient as a function of the tip speed ratio. For both figures, while the X-axis presents the tip speed ratios, the Y-axis shows the performance on the left-hand side and the improvement as a percentage on the right-hand side. It is clear that the torque coefficient decreases with increasing tip speed ratio, and the power coefficient

(a) Turbine (S_0) at 150°

(b) Turbine (S_1) at 150°

(c) Turbine (S_2) at 150°

(d) Turbine (S_3) at 150°

(e) Turbine (S_4) at 150°
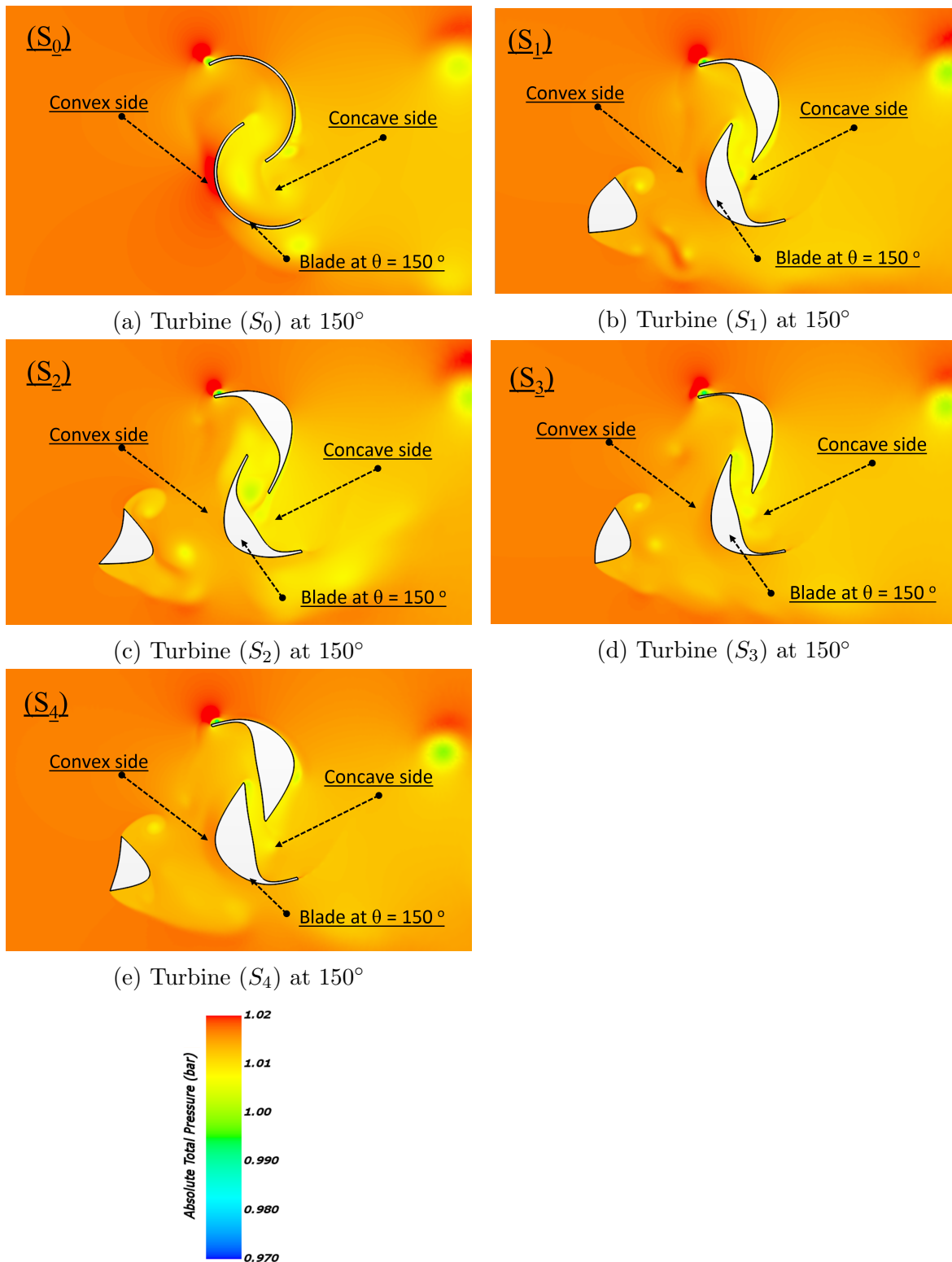
Figure 6.44: Pressure distribution around the blades for all five configurations (S_0, S_1, S_2, S_3, and S_4) at rotational angle of 150°.

116

is well described by a third-order polynomial, as stated in the literature and previous sections. Interestingly, the four configurations perform better in comparison to the standard Savonius turbine over the whole operating range ($0.6 \leq \lambda \leq 1.2$), as shown in Figure 6.48. The performance increases by almost 25% in comparison with the standard shape at both tip speed ratios $\lambda = 1.1$ and $\lambda = 1.2$.
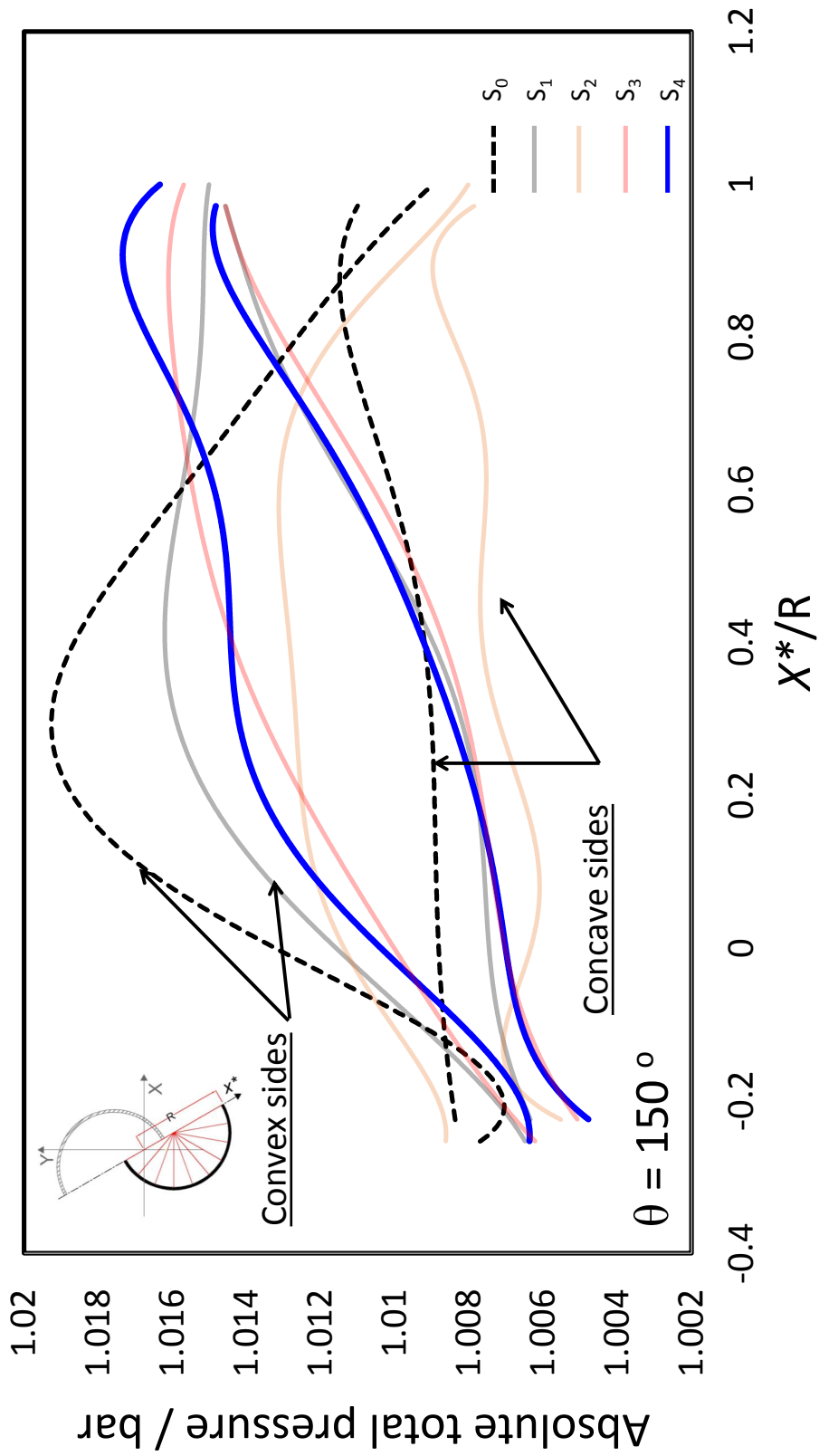
Figure 6.45: Comparison of the pressure distribution around the blades at an angular position of 150°.

6.10. Complete optimization process for the thick blades with a thick deflector plate, optimized simultaneously

(a) Turbine (S_0) at 240°

(b) Turbine (S_1) at 240°

(c) Turbine (S_2) at 240°

(d) Turbine (S_3) at 240°

(e) Turbine (S_4) at 240°
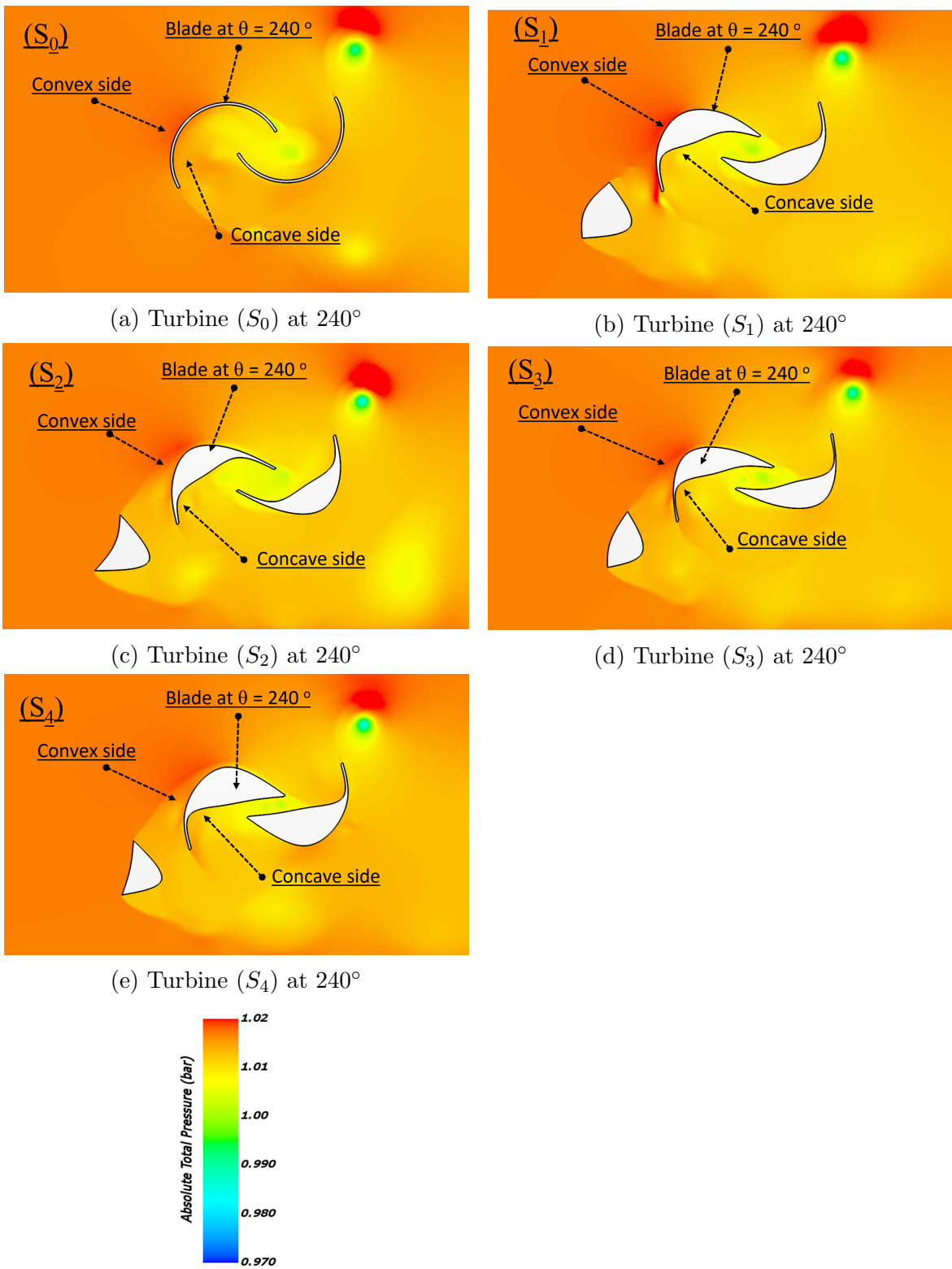
Figure 6.46: Pressure distribution around the blades for all five configurations (S_0, S_1, S_2, S_3, and S_4) at a rotational angle of 240°.
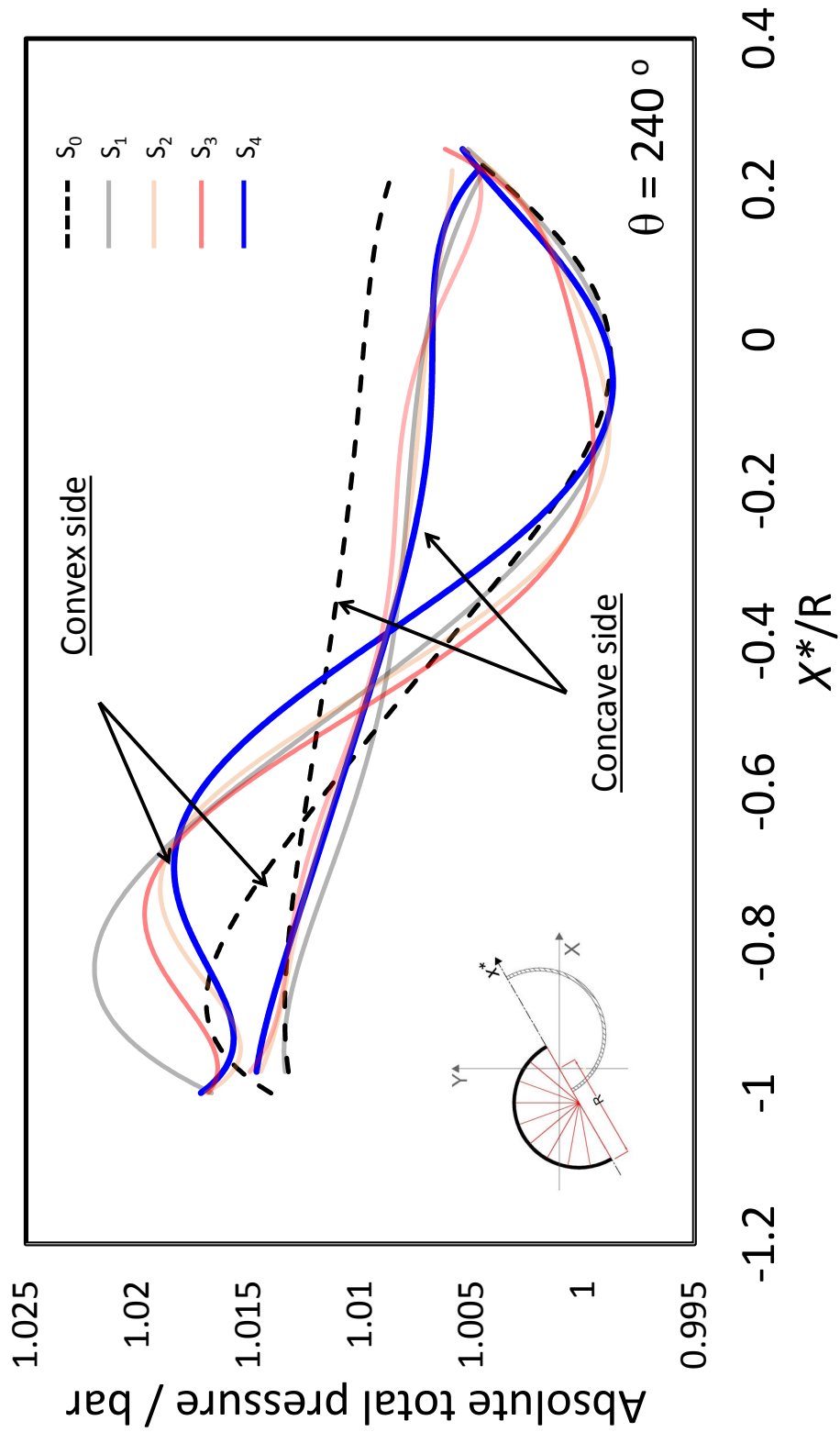
Figure 6.47: Comparison of the pressure distribution around the blades at an angular position of 240°.
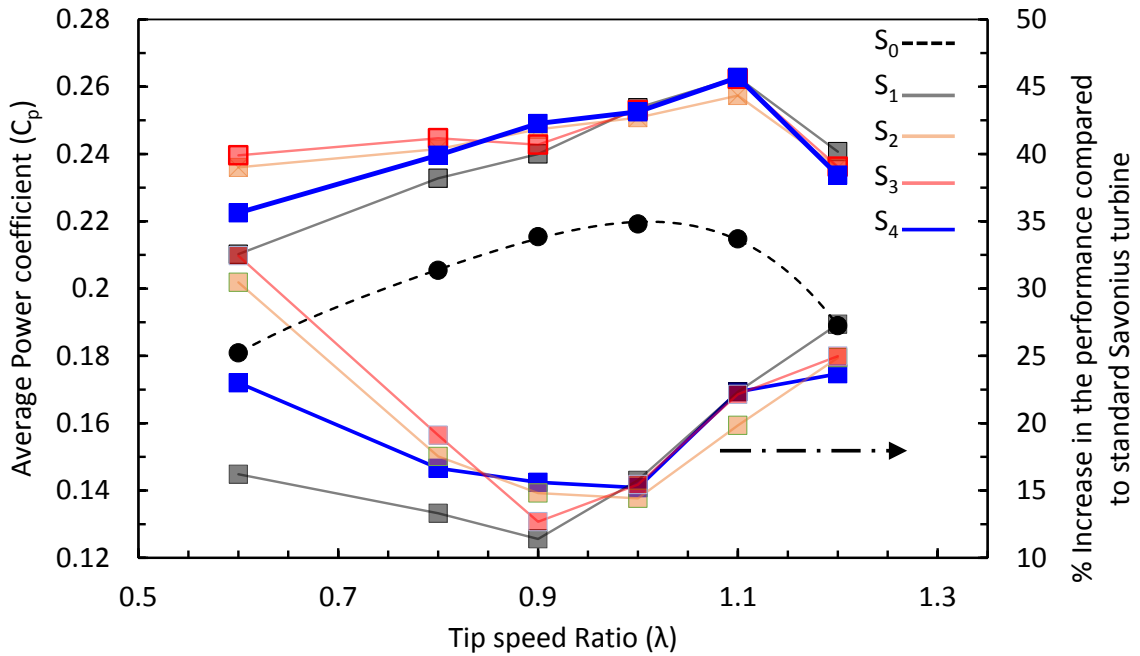
(a) Average power coefficient
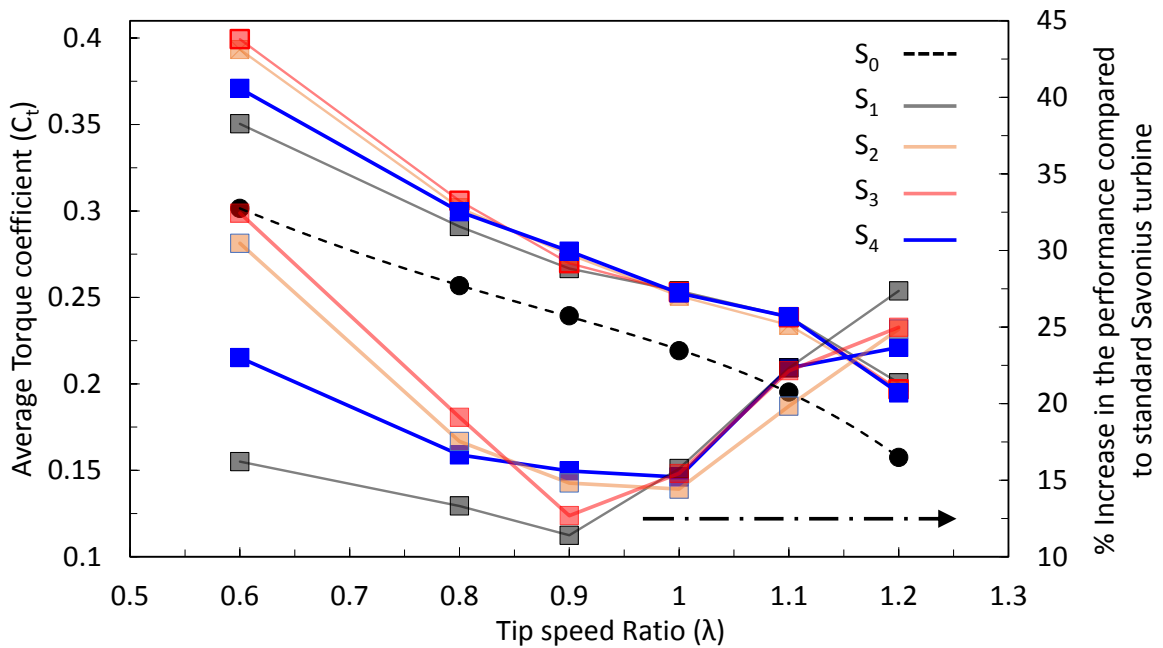
(b) Average torque coefficient

Figure 6.48: Comparison of (a) the average power coefficient and (b) the average torque coefficient as a function of the tip speed ratio for the four optimal configurations and for the standard Savonius turbine. On the right scale the percentage increase for each tip speed ratio is shown.

6.11   Conclusions

In the study presented here, a new hybrid system for a hydraulic Savonius turbine pairing thick blades with a thick plate was optimized in order not only to improve the performance of the whole system when used in water, but also to prevent the returning blades from being damaged by suspended solids in the water. After some preliminary steps, the optimization of a thick blade for the turbine was carried out. Then, the second step was to optimize position and shape of a deflector plate in front of the turbine. The third step was to determine the effect of the deflector and of the thick blades in combination. It proves that the deflector was more useful at low tip speed ratios, while the thick blades are promising at higher tip speed ratios. Finally, all of the parameters of the blades and the deflector plate were optimized simultaneously, providing four optimal configurations. Overall, the optimal configurations improved the performance of the turbine by up to 25% compared with the standard Savonius turbine without a deflector. Table 6.9 summarizes all of the optimization processes and the corresponding relative improvements in performance. From an engineering point of view, S_4 is recommended.

Table 6.9: Summarization of the optimization processes and the corresponding improvements

Optimization case	Relative increase in performance	Tip speed ratio corresponding to improvement
Thick blades	12%, 15%	1.1, 1.2
Thick deflector	11.6%, 15%	1.1, 1.2
Overlap and gap ratio	6 %	1.1
Arc angle	6 %	1.1
Optimized thick blades with fixed thick plate	3 % compared to standard with deflector, 15% compared to standard without deflector	1.1
Optimized thick plate with fixed thick blades	0% compared to standard with deflector, 12% compared to standard without deflector	1.1 (the optimization process was not completed)
Overall optimization	25 % compared to standard without deflector, 12% compared to optimal thick blades, 13% compared to standard with optimal deflector	1.1

Chapter 7

Summary and Outlook

It is clear now that hydrokinetic vertical axis turbines may make an important contribution to a global sustainable energy strategy. Since 70% of the earth is water, using this type of turbine in aquatic environments will be a topic of interest in the future. Savonius turbines fullfill all of the requirements to be applied in this field. In addition to being robust and having a simple design, they can be manufactured at a very low cost. However, the simple design of this turbine usually suffers from a very low efficiency. Therefore, this thesis focused on optimizing the hydraulic Savonius turbine to improve its performance. As the first step before starting the optimization process, computational fluid dynamics (CFD) should produce a very accurate model of the flow structure and performance of the turbine in order to be sure that the optimization procedure produces the right optimal results. After validation based on experimental results, optimization could start. Genetic algorithms were used to optimize the system while the performance was evaluated by using computational fluid dynamics. After many new preliminary steps, the optimization process could be carried out in a fully automatic manner, allowing the efficient exploration of a variety of configurations. However, each optimization process take several weeks to converge. Therefore, the optimization was divided into several steps until the final geometry was determined. These steps can be illustrated as follows:

- A Savonius turbine with different blade shapes on the concave and convex sides has been optimized. The optimal Savonius blade is flatter on the concave side but shows a strong change in direction close to the tip, with a hook-like form; the convex side is almost unchanged and very close to a semi-circular shape. The performance of the turbine was improved by almost 14% compared to the standard shape. The optimization process consumed almost 14 days using 25 nodes (each one is a 16-core) in a cluster. It is interesting to note that Betz already recommended the use of a hooked-shape Savonius in his book [127], as
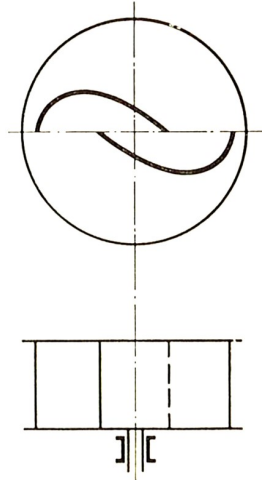
Figure 7.1: Savonius turbine shape recommended by Betz [127].

shown in Figure 7.1.

- The position and the shape of a deflector in front of the standard Savonius turbine were optimized. The obtained optimal deflector plate covers only the outer half of the returning blade in the Y-direction and stays relatively far from the turbine (about $1.4R$). The upstream side of the deflector plate is curved and redirects the flow towards the advancing blade, while the downstream side is almost straight. When using this deflector, the performance was improved by almost 15% compared to the standard shape without the deflector. When using a deflector plate, each simulation consumes more time in comparison to the turbine without the deflector due to the many vortices produced by the deflector inside the flow. Here, the optimization result was obtained after 24 days by using the same number of nodes as in the previous optimization process.

- In the next step, the three main parameters (overlap ratio, gap ratio, and arc angle) characterizing the geometry of a hydraulic Savonius turbine were simultaneously optimized. Here, the optimization process consumed less time as the number of parameters was small; moreover, each simulation took less time. Therefore the whole process takes only one week. The performance increased by almost 10% in comparison with the standard Savonius turbine.

- The combination of the deflector plate with the thick blades was studied in detail. First, the optimal thick blades were kept fixed and the deflector was optimized. Then, the optimal deflector was kept constant during optimization of the thick blades. It was found that the optimal deflector is very useful at lower tip speed ratios, while thick blades are more useful at higher tip speed ratios.

- Finally, an aggressive optimization process with nineteen parameters was performed to get the final configuration of the turbine and the deflector. Four different optimal configurations were produced from the optimization process leading to almost the same performance. When using any of these configurations, the performance improved by up to 28 % compared to the standard shape without the deflector. The pure computational time for this optimization process was almost two months using a high-speed computer.

- In addition to the different optimization processes that were conducted in this thesis, experimental work was done using PIV and torque sensors in order to validate our numerical model based on the experimental work. This experimental comparison was repeated by adding a deflector plate in order to validate the optimization process.

7.1 Suggestions for further research

Besides all of the numerical and experimental works done for this thesis, the final configuration should be checked experimentally. For this purpose, configuration S_4 should be built and investigated in our water channel.

Moreover, this research area could be extended to investigate the interactions between two optimal configurations used in a flotilla system instead of one single turbine. In this manner, it could be checked if optimal Savonius turbines could be efficiently used in a farm.

Bibliography

[1] UN Water. The United Nations' world water development report 2014: water and energy. *United Nations, Paris*, 2014.

[2] REN21: Renewable Energy Policy Network for the 21st Century. Renewables 2019: Global status report, 2019.

[3] REN21: Renewable Energy Policy Network for the 21st Century. Renewables 2022: Global status report, 2022.

[4] AN Menegaki. Growth and renewable energy in Europe: a random effect model with evidence for neutrality hypothesis. *Energy Economics*, 33(2):257–263, 2011.

[5] D Goodstein. *Out of Gas: The end of the age of oil*. WW Norton & Company, 2005.

[6] P Roberts. *The End of Oil: On the edge of a perilous new world*. Houghton Mifflin Harcourt, 2005.

[7] F Barbir. Transition to renewable energy systems with hydrogen as an energy carrier. *Energy*, 34(3):308–312, 2009.

[8] S Wang, LJ Qing, H Wang, and HY Li. Integrated assessment of environmental performance-based contracting for sulfur dioxide emission control in chinese coal power plants. *Journal of Cleaner Production*, 177:878–887, 2018.

[9] K Elsaid, ET Sayed, MA Abdelkareem, MS Mahmoud, M Ramadan, and AG Olabi. Environmental impact of emerging desalination technologies: A preliminary evaluation. *Journal of Environmental Chemical Engineering*, 8(5):104099, 2020.

[10] ET Sayed, T Wilberforce, K Elsaid, MKH Rabaia, MA Abdelkareem, KJ Chae, and AG Olabi. A critical review on environmental impacts of renewable energy systems and mitigation strategies: Wind, hydro, biomass and geothermal. *Science of the Total Environment*, 766:144505, 2021.

[11] JF Kenny, NL Barber, SS Hutson, KS Linsey, JK Lovelace, and MA Maupin. Estimated use of water in the United States in 2005. Technical report, US Geological Survey, 2009.

[12] F Matthes, C Heinemann, S Ludig, and V Cook. Renewables versus fossil fuels – comparing the costs of electricity systems. Technical report, Öko-Institut, 2017.

[13] WP Schill, M Pahle, and C Gambardella. Start-up costs of thermal power plants in markets with increasing shares of variable renewable generation. *Nature Energy*, 2(6):1–6, 2017.

[14] JP Barton and DG Infield. Energy storage and its use with intermittent renewable energy. *IEEE Transactions on Energy Conversion*, 19(2):441–448, 2004.

[15] O Yuksek, MI Komurcu, I Yuksel, and K Kaygusuz. The role of hydropower in meeting Turkey's electric energy demand. *Energy Policy*, 34(17):3093–3103, 2006.

[16] G Müller and K Kauppert. Performance characteristics of water wheels. *Journal of Hydraulic Research*, 42(5):451–460, 2004.

[17] E Quaranta. Stream water wheels as renewable energy supply in flowing water: theoretical considerations, performance assessment and design recommendations. *Energy for Sustainable Development*, 45:96–109, 2018.

[18] DM Rosenberg, RA Bodaly, and PJ Usher. Environmental and social impacts of large scale hydroelectric development: who is listening? *Global Environmental Change*, 5(2):127–148, 1995.

[19] O Cleynen, E Kerikous, S Hoerner, and D Thévenin. Characterization of the performance of a free-stream water wheel using computational fluid dynamics. *Energy*, 165:1392–1400, 2018.

[20] S Eriksson, H Bernhoff, and M Leijon. Evaluation of different turbine concepts for wind power. *Renewable and Sustainable Energy Reviews*, 12(5):1419–1434, 2008.

[21] P Kozak. *Effects of unsteady aerodynamics on vertical-axis wind turbine performance.* PhD thesis, Illinois Institute of Technology, 2014.

[22] SL Dixon and C Hall. *Fluid Mechanics and Thermodynamics of Turbomachinery.* Butterworth-Heinemann, 2013.

[23] E Hau and H von Renouard. Commercial applications of wind turbines. *Wind Turbines: Fundamentals, Technologies, Application, Economics*, pages 563–614, 2006.

[24] AC Hansen and CP Butterfield. Aerodynamics of horizontal-axis wind turbines. *Annual Review of Fluid Mechanics*, 25(1):115–149, 1993.

[25] LA Viterna and DC Janetzke. Theoretical and experimental power from large horizontal-axis wind turbines. Technical report, National Aeronautics and Space Administration, Cleveland, OH (USA). Lewis Research Center, 1982.

[26] MJ Khan, G Bhuyan, MT Iqbal, and JE Quaicoe. Hydrokinetic energy conversion systems and assessment of horizontal and vertical axis turbines for river and tidal applications: A technology status review. *Applied Energy*, 86(10):1823–1835, 2009.

[27] P Bachant, A Goude, and M Wosnik. Actuator line modeling of vertical-axis turbines. *arXiv preprint arXiv:1605.01449*, 2016.

[28] AM El Baz, AR Refaey, Y Mohannad, and AWY Mohammed. Computational modelling of H-type Darrieus vertical axis wind turbine with multi element airfoil blades. In *Proceedings of ICFD11, Eleventh International Conference of Fluid Dynamics, Alexandria, Egypt*, 2013.

[29] S Hoerner, S Abbaszadeh, T Maître, O Cleynen, and D Thévenin. Characteristics of the fluid–structure interaction within Darrieus water turbines with highly flexible blades. *Journal of Fluids and Structures*, 88:13–30, 2019.

[30] S Hoerner, C Bonamy, O Cleynen, T Maître, and D Thévenin. Darrieus vertical-axis water turbines: deformation and force measurements on bioinspired highly flexible blade profiles. *Experiments in Fluids*, 61:1–17, 2020.

[31] G Mercier, C Pellone, and T aître. Experimental characterization of the near-wake of a cross flow water turbine with ldv measurements. In *Proceedings of the 17th International Symposium on Applications of Laser Techniques to Fluid Mechanic, Lisbon, Portugal*, pages 7–10, 2014.

[32] S Hoerner, S Abbaszadeh, O Cleynen, C Bonamy, T Maître, and D Thévenin. Passive flow control mechanisms with bioinspired flexible blades in cross-flow tidal turbines. *Experiments in Fluids*, 62(5):1–14, 2021.

[33] M Balat. A review of modern wind turbine technology. *Energy Sources, Part A*, 31(17):1561–1572, 2009.

[34] SB Qamar and I Janajreh. A comprehensive analysis of solidity for cambered Darrieus VAWTs. *International Journal of Hydrogen Energy*, 42(30):19420–19431, 2017.

[35] O Cleynen, S Engel, S Hoerner, and D Thévenin. Optimal design for the free-stream water wheel: A two-dimensional study. *Energy*, 214:118880, 2021.

[36] SJ Savonius. *The wing-rotor in theory and practice*. Omnia-Mikrofilm-Technik, 1981.

[37] M Nakajima, S Iio, and T Ikeda. Performance of double-step Savonius rotor for environmentally friendly hydraulic turbine. *Journal of Fluid Science and Technology*, 3(3):410–419, 2008.

[38] MH Mohamed, G Janiga, E Pap, and D Thévenin. Optimal performance of a modified three-blade Savonius turbine using frontal guiding plates. In *ASME Turbo Expo 2010: Power for Land, Sea, and Air*, pages 803–812. Glasgow, UK, 2010.

[39] MH Mohamed and D Thévenin. Performance optimization of a Savonius turbine considering different shapes for frontal guiding plates. In *10th International Conference of Fluid Dynamics ASME-ICFD, Cairo, Egypt, ICFD10-EG-3026*, 2010.

[40] KH Wong, WT Chong, NL Sukiman, SC Poh, YC Shiah, and CT Wang. Performance enhancements on vertical axis wind turbines using flow augmentation systems: A review. *Renewable and Sustainable Energy Reviews*, 73:904–921, 2017.

[41] JV Akwa, HA Vielmo, and AP Petry. A review on the performance of Savonius wind turbines. *Renewable and Sustainable Energy Reviews*, 16(5):3054–3064, 2012.

[42] A Kumar and RP Saini. Performance parameters of Savonius type hydrokinetic turbine: A Review. *Renewable and Sustainable Energy Reviews*, 64:289–310, 2016.

[43] M Zemamou, M Aggour, and A Toumi. Review of Savonius wind turbine design and performance. *Energy Procedia*, 141:383–388, 2017.

[44] UK Saha, S Thotla, and D Maity. Optimum design configuration of Savonius rotor through wind tunnel experiments. *Journal of Wind Engineering and Industrial Aerodynamics*, 96(8-9):1359–1375, 2008.

[45] BF Blackwell, LV Feltz, and RE Sheldahl. *Wind tunnel performance data for two-and three-bucket Savonius rotors*. Sandia Laboratories Albuquerque, New Mexico, 1977.

[46] M Lates and R Velicu. CFD analysis and theoretical modelling of multiblade small Savonius wind turbines. In *Sustainable Energy in the Built Environment-Steps Towards nZEB*, pages 403–415. Springer, 2014.

[47] I Ushiyama and H Nagai. Optimum design configurations and performance of Savonius rotors. *Wind Engineering*, pages 59–75, 1988.

[48] W Vance. Vertical axis wind rotors–status and potential. In *Proceedings of the conference on wind energy conversion systems*, pages 96–102, 1973.

[49] AJ Alexander and BP Holownia. Wind tunnel tests on a Savonius rotor. *Journal of Wind Engineering and Industrial Aerodynamics*, 3(4):343–351, 1978.

[50] VJ Modi and MS Fernando. On the performance of the Savonius wind turbine. *Journal of Solar Energy Engineering*, 111(1):71–81, 02 1989.

[51] JL Menet and N Bourabaa. Increase in the Savonius rotors efficiency via a parametric investigation. In *European Wind Energy conference & exhibition*, pages 22–25. London, UK, 2004.

[52] MR Ahmed, M Faizal, and YH Lee. Optimization of blade curvature and inter-rotor spacing of Savonius rotors for maximum wave energy extraction. *Ocean Engineering*, 65:32–38, 2013.

[53] A Al-Faruk and A Sharifian. Geometrical optimization of a swirling Savonius wind turbine using an open jet wind tunnel. *Alexandria Engineering Journal*, 55(3):2055–2064, 2016.

[54] AS Grinspan and UK Saha. Experimental investigation of twisted bladed Savonius wind turbine rotor. *International Energy Journal*, 5, 2005.

[55] K Kacprzak, G Liskiewicz, and K Sobczak. Numerical investigation of conventional and modified Savonius wind turbines. *Renewable Energy*, 60:578–585, 2013.

[56] L Song, ZX Yang, RT Deng, and XG Yang. Performance and structural optimization for a new type of vertical axis wind turbine. In *Proceedings of the 2013 International Conference on Advanced Mechatronic Systems*, pages 687–692. IEEE, 2013.

[57] S Sharma and RK Sharma. Performance improvement of Savonius rotor using multiple quarter blades–a CFD investigation. *Energy Conversion and Management*, 127:43–54, 2016.

[58] M Tartuferi, V D'Alessandro, S Montelpare, and R Ricci. Enhancement of Savonius wind rotor aerodynamic performance: a computational study of new blade shapes and curtain systems. *Energy*, 79:371–384, 2015.

[59] GG Muscolo and R Molfino. From Savonius to bronzinus: a comparison among vertical wind turbines. *Energy Procedia*, 50:10–18, 2014.

[60] W Tian, Z Mao, B Zhang, and Y Li. Shape optimization of a Savonius wind rotor with different convex and concave sides. *Renewable Energy*, 117:287–299, 2018.

[61] A Banerjee, S Roy, P Mukherjee, and UK Saha. Unsteady flow analysis around an elliptic-bladed Savonius-style wind turbine. In *Gas Turbine India Conference*, volume 49644, page V001T05A001. American Society of Mechanical Engineers, 2014.

[62] N Alom, SC Kolaparthi, SC Gadde, and UK Saha. Aerodynamic design optimization of elliptical-bladed Savonius-style wind turbine by numerical simulations. In *International Conference on Offshore Mechanics and Arctic Engineering*, volume 49972, page V006T09A009. American Society of Mechanical Engineers, 2016.

[63] MH Mohamed, G Janiga, E Pap, and D Thévenin. Optimal blade shape of a modified Savonius turbine using an obstacle shielding the returning blade. *Energy Conversion and Management*, 52(1):236–242, 2011.

[64] M Tartuferi, V D'Alessandro, S Montelpare, and R Ricci. Enhancement of Savonius wind rotor aerodynamic performance: A computational study of new blade shapes and curtain systems. *Energy*, 79:371–384, 2015.

[65] S Roy and UK Saha. Wind tunnel experiments of a newly developed two-bladed Savonius-style wind turbine. *Applied Energy*, 137:117–125, 2015.

[66] N Alom, B Borah, and UK Saha. An insight into the drag and lift characteristics of modified bach and benesh profiles of savonius rotor. *Energy Procedia*, 144:50–56, 2018.

[67] SM Al-Absi and HB Salleh. Numerical investigation of Savonius rotor elliptical and the design modification on a blade shape. In *Advances in Material Sciences and Engineering*, pages 177–185. Springer, 2020.

[68] CM Shashikumar and V Madav. Numerical and experimental investigation of modified v-shaped turbine blades for hydrokinetic energy generation. *Renewable Energy*, 177:1170–1197, 2021.

[69] O Cleynen, S Hoerner, and D Thévenin. Characterization of hydraulic power in free-stream installations. *International Journal of Rotating Machinery*, 2017, 2017.

[70] T Hayashi, Y Li, and Y Hara. Wind tunnel tests on a different phase three-stage Savonius rotor. *JSME International Journal Series B Fluids and Thermal Engineering*, 48(1):9–16, 2005.

[71] WA El-Askary, MH Nasef, AA Abdel-Hamid, and HE Gad. Harvesting wind energy for improving performance of Savonius rotor. *Journal of Wind Engineering and Industrial Aerodynamics*, 139:8–15, 2015.

[72] K Irabu and JN Roy. Characteristics of wind power on Savonius rotor using a guide-box tunnel. *Experimental Thermal and Fluid Science*, 32(2):580–586, 2007.

[73] M Tartuferi, V D'Alessandro, S Montelpare, and R Ricci. Enhancement of Savonius wind rotor aerodynamic performance: a computational study of new blade shapes and curtain systems. *Energy*, 79:371–384, 2015.

[74] MH Mohamed, G Janiga, E Pap, and D Thévenin. Optimization of Savonius turbines using an obstacle shielding the returning blade. *Renewable Energy*, 35(11):2618–2626, 2010.

[75] K Golecha, TI Eldho, and SV Prabhu. Influence of the deflector plate on the performance of modified Savonius water turbine. *Applied Energy*, 88(9):3207–3217, 2011.

[76] AH Elbatran, YM Ahmed, and AS Shehata. Performance study of ducted nozzle Savonius water turbine, comparison with conventional Savonius turbine. *Energy*, 134:566–584, 2017.

[77] A Grönman, J Backman, M Hansen-Haug, M Laaksonen, M Alkki, and P Aura. Experimental and numerical analysis of vaned wind turbine performance and flow phenomena. *Energy*, 159:827–841, 2018.

[78] HA Heikal, OSM Abu-Elyazeed, MAA Nawar, YA Attai, and MMS Mohamed. On the actual power coefficient by theoretical developing of the diffuser flange of wind-lens turbine. *Renewable Energy*, 125:295–305, 2018.

[79] AN Shikha, TS Bhatti, and DP Kothari. Wind energy conversion systems as a distributed source of generation. *Journal of Energy Engineering*, 129(3):69–80, 2003.

[80] BD Altan and M Atılgan. The use of a curtain design to increase the performance level of a Savonius wind rotor. *Renewable Energy*, 35(4):821–829, 2010.

[81] K Pope, V Rodrigues, R Doyle, A Tsopelas, R Gravelsins, GF Naterer, and E Tsang. Effects of stator vanes on power coefficients of a zephyr vertical axis wind turbine. *Renewable Energy*, 35(5):1043–1051, 2010.

[82] YX Yao, ZP Tang, and XW Wang. Design based on a parametric analysis of a drag driven VAWT with a tower cowling. *Journal of Wind Engineering and Industrial Aerodynamics*, 116:32–39, 2013.

[83] MH Mohamed, G Janiga, and D Thévenin. Optimal design of a Savonius turbine. In *Conference on Modelling Fluid Flow (CMFF'12) The 15th International Conference on Fluid Flow Technologies Budapest*, pages 4–7, 2012.

[84] BM Shaughnessy and SD Probert. Partially-blocked Savonius rotor. *Applied Energy*, 43(4):239–249, 1992.

[85] G Kailash, TI Eldho, and SV Prabhu. Performance study of modified Savonius water turbine with two deflector plates. *International Journal of Rotating Machinery*, 2012:12 pages, 2012. Article ID 679247.

[86] M Kunasekaran, SH Rhee, N Venkatesan, and A Samad. Design optimization of a marine current turbine having winglet on blade. *Ocean Engineering*, 239:109877, 2021.

[87] AK Jaiswal, Md Siddique, AR Paul, and A Samad. Surrogate-based design optimization of a centrifugal pump impeller. *Engineering Optimization*, 54(8):1395–1412, 2022.

[88] MH Siddique, A Samad, and S Hossain. Centrifugal pump performance enhancement: Effect of splitter blade and optimization. *Proceedings of the Institution of Mechanical Engineers, Part A: Journal of Power and Energy*, 236(2):391–402, 2022.

[89] HW Kuhn. Nonlinear programming: a historical view. In *Traces and Emergence of Nonlinear Programming*, pages 393–414. Springer, 2014.

[90] LT Biegler. *Nonlinear programming: concepts, algorithms, and applications to chemical processes.* SIAM, 2010.

[91] A Messac. *Optimization in practice with MATLAB®: for engineering students and professionals.* Cambridge University Press, 2015.

[92] D Thévenin and G Janiga. *Optimization and Computational Fluid Dynamics.* Springer Science & Business Media, 2008.

[93] JK Karlof. *Integer programming: Theory and Practice.* CRC Press, 2005.

[94] DS Chen, RG Batson, and Y Dang. *Applied Integer Programming: Modeling and Solution.* John Wiley & Sons, 2011.

[95] J Hromkovič. *Algorithmics for Hard Problems: Introduction to combinatorial optimization, randomization, approximation, and heuristics.* Springer Science & Business Media, 2013.

[96] D Simon. *Evolutionary Optimization Algorithms, John Willey & Sons.* Inc, 2013.

[97] CO Paschereit, B Schuermans, and D Büche. Combustion process optimization using evolutionary algorithm. In *Turbo Expo: Power for Land, Sea, and Air*, volume 36851, pages 281–291, 2003.

[98] JH Holland. *Adaptation in Natural and Artificial Systems: An introductory analysis with applications to biology, control, and artificial intelligence.* MIT press, 1992.

[99] JH Holland. Genetic algorithms. *Scientific American*, 267(1):66–73, 1992.

[100] DE Goldberg. *Genetic Algorithms in Search, Optimization and Machine Learning.* Addison-Wesley Longman Publishing Co., Inc., USA, 1st edition, 1989.

[101] K Deb, RB Agrawal, et al. Simulated binary crossover for continuous search space. *Complex Systems*, 9(2):115–148, 1995.

[102] K Deb, M Goyal, et al. A combined genetic adaptive search (Geneas) for engineering design. *Computer Science and Informatics*, 26:30–45, 1996.

[103] K Deb, A Pratap, S Agarwal, and T Meyarivan. A fast and elitist multiobjective genetic algorithm: NSGA-II. *IEEE Transactions on Evolutionary Computation*, 6(2):182–197, 2002.

[104] L Daróczy, G Janiga, and D Thévenin. Systematic analysis of the heat exchanger arrangement problem using multi-objective genetic optimization. *Energy*, 65:364–373, 2014.

[105] E Kerikous and D Thévenin. Optimal shape of thick blades for a hydraulic Savonius turbine. *Renewable Energy*, 134:629–638, 2019.

[106] E Kerikous and D Thévenin. Performance Enhancement of a Hydraulic Savonius Turbine by Optimizing Overlap and Gap Ratios. volume 2 of *Gas Turbine India Conference*, 2019. V002T06A016.

[107] E Kerikous and D Thévenin. Optimal shape and position of a thick deflector plate in front of a hydraulic Savonius turbine. *Energy*, 189:116157, 2019.

[108] K Kacprzak, G Liskiewicz, and K Sobczak. Numerical investigation of conventional and modified Savonius wind turbines. *Renewable Energy*, 60:578–585, 2013.

[109] MMA Bhutta, N Hayat, AU Farooq, Z Ali, ShR Jamil, and Z Hussain. Vertical axis wind turbine–a review of various configurations and design techniques. *Renewable and Sustainable Energy Reviews*, 16(4):1926–1939, 2012.

[110] O Yaakob, YM Ahmed, and MA Ismail. Validation study for Savonius vertical axis marine current turbine using CFD simulation. In *Asia-Pasific Workshop on Marine Hydrodynamics*, volume 6, pages 327–332, 2012.

[111] MS Abdullah, MHH Ishak, and F Ismail. Numerical study of the 3D Savonius turbine under stationary conditions. *Engineering Failure Analysis*, 136:106199, 2022.

[112] SJ Chemengich, SZ Kassab, and ER Lotfy. Effect of the variations of the gap flow guides geometry on the Savonius wind turbine performance: 2d and 3d studies. *Journal of Wind Engineering and Industrial Aerodynamics*, 222:104920, 2022.

[113] CD Adapco. Star CCM+ User Guide Version 12.04. *CD-Adapco: New York, NY, USA*, 2017.

[114] L Daróczy, G Janiga, K Petrasch, M Webner, and D Thévenin. Comparative analysis of turbulence models for the aerodynamic simulation of H-Darrieus rotors. *Energy*, 90:680–690, 2015.

[115] M Nakajima, S Iio, and T Ikeda. Performance of Savonius rotor for environmentally friendly hydraulic turbine. *Journal of Fluid Science and Technology*, 3(3):420–429, 2008.

[116] RI Loehrke and HM Nagib. Control of free-stream turbulence by means of honeycombs: a balance between suppression and generation. *Journal of Fluids Engineering*, 98(3):342–351, 1976.

[117] A Hijazi and V Madhavan. A novel ultra-high speed camera for digital image processing applications. *Measurement Science and Technology*, 19(8):085503, 2008.

[118] MD Atkins. Velocity field measurement using particle image velocimetry (PIV). In *Application of Thermo-Fluidic Measurement Techniques*, pages 125–166. Elsevier, 2016.

[119] RJ Moffat. Describing the uncertainties in experimental results. *Experimental Thermal and Fluid Science*, 1(1):3–17, 1988.

[120] SJ Kline. Describing uncertainty in single sample experiments. *Mech. Engineering*, 75:3–8, 1953.

[121] RJ Moffat. Using uncertainty analysis in the planning of an experiment. *Journal of Fluids Engineering*, 107(2):173–178, 06 1985.

[122] L Daróczy, MH Mohamed, G Janiga, and D Thévenin. Analysis of the effect of a slotted flap mechanism on the performance of an H-Darrieus turbine using CFD. In *ASME Turbo Expo 2014*. American Society of Mechanical Engineers, Paper GT2014-25250, 2014.

[123] L Daróczy, G Janiga, and D Thévenin. Analysis of the performance of a H-Darrieus rotor under uncertainty using polynomial chaos expansion. *Energy*, 113:399–412, 2016.

[124] L Daróczy, G Janiga, and D Thévenin. Computational fluid dynamics based shape optimization of airfoil geometry for an H-rotor using a genetic algorithm. *Engineering Optimization*, pages 1–17, 2017.

[125] T Eger, T Bol, AR Thanu, L Daróczy, G Janiga, R Schroth, and D Thévenin. Application of entropy generation to improve heat transfer of heat sinks in electric machines. *Entropy*, 19(6):255, 2017.

[126] J Meyer, L Daróczy, and D Thévenin. Shape optimization of the pick-up tube in a pitot-tube jet pump. *Journal of Fluids Engineering*, 139(2):021103, 2017.

[127] A Betz. *Einführung in die Theorie der Strömungsmaschinen*. G. Braun, 1959.

Journal publications

T. Das, **E. Kerikous**, G. Janiga, N. Venkatesan, and D. Thévenin. Performance Improvement of Wells Turbine through an Automated Optimization Technique. Energy Conversion and Management: X, 16:100285, 2022.

T. Das, **E. Kerikous**, G. Janiga, N. Venkatesan, D. Thévenin, A. Samad. Mapping Performace of a Marine Energy Harvesting Turbine for Flow Coefficient and Reynolds Number through an Automated Optimization Technique. Sustainable Energy Technologies and Assessments (Under review).

E. Kerikous and D. Thévenin. Optimal Shape and Position of a Thick Deflector Plate in Front of a Hydraulic Savonius Turbine, Energy, 189:116157, 2019.

E. Kerikous and D. Thévenin. Optimal Shape of Thick Blades for a Hydraulic Savonius Turbine, Renewable Energy , 134:629-638, 2019.

O. Cleynen, **E. Kerikous**, and D. Thévenin. Characterization of the Performance of a Free-Stream Water Wheel using Computational Fluid Dynamics, Energy , 165:1392-1400, 2018.

Proceedings and Conferences

I. Hashem, **E. Kerikous**, S. Hoerner, and D. Thévenin. Performance Investigation of a Savonius Wind Turbine with Unconventional Blade Designs Inspired by Sand Eels. In: Conference on Modelling Fluid Flow CMFF'22, (Vad, J., Ed.), Budapest, Hungary, 54/1-8, 2022.

E. Kerikous and D. Thévenin. Performance Enhancement of a Hydraulic Savonius Turbine by Optimizing Overlap and Gap Ratios. In: ASME 2019 Gas Turbine India Conference, Channei, India, December 5-6, 2019.

O. Cleynen, **E. Kerikous**, S. Hoerner, and D. Thévenin. Influence of Flotation Bodies on the Power Characteristics of a Free-Stream Water Wheel. In: 9th International Conference on Computational & Experimental Methods in Multiphase & Complex Flow, Tallinn, Estonia, June 20-22, 2017.

H.A. Heikal, **E. Kerikous**, and R. Abd El-Maksoud. Hybrid Valve with Variable Performance Curves. In: Aerospace sciences & aviation technology, Cairo, Egypt, ASAT-15-132-HF, 2013.

....

Date

....

Signature